

Open Research Online

The Open University's repository of research publications and other research outputs

Cosmic spherules from Widerøefjellet, Sør Rondane Mountains (East Antarctica)

Journal Item

How to cite:

Goderis, Steven; Soens, Bastien; Huber, Matthew; McKibben, Seann; van Ginneken, Matthias; Van Maldeghem, Flore; Debaille, Vinciane; Greenwood, Richard; Franchi, Ian; Cnudde, Veerle; Van Malderen, Stijn; Vanhaeke, Frank; Koeberl, Christian; Topa, Dan and Claeys, Philippe (2020). Cosmic spherules from Widerøefjellet, Sør Rondane Mountains (East Antarctica). *Geochimica et Cosmochimica Acta*, 270 pp. 112–143.

For guidance on citations see [FAQs](#).

© 2019 Elsevier Ltd.



<https://creativecommons.org/licenses/by-nc-nd/4.0/>

Version: Accepted Manuscript

Link(s) to article on publisher's website:

<http://dx.doi.org/doi:10.1016/j.gca.2019.11.016>

Copyright and Moral Rights for the articles on this site are retained by the individual authors and/or other copyright owners. For more information on Open Research Online's [data policy](#) on reuse of materials please consult the policies page.

32 *Corresponding author. Email address: Steven.Goderis@vub.be (S. Goderis)

33 **Abstract**

34 A newly discovered sedimentary accumulation of micrometeorites in the Sør Rondane Mountains
35 of East Antarctica, close to the Widerøefjellet summit at ~2750 meter above sea level, is
36 characterized in this work. The focus here lies on 2099 melted cosmic spherules larger than
37 200 μm , extracted from 3.2 kg of sampled sediment. Although the Widerøefjellet deposit shares
38 similarities to the micrometeorite traps encountered in the Transantarctic Mountains, both subtle
39 and more distinct differences in the physicochemical properties of the retrieved extraterrestrial
40 particles and sedimentary host deposits are discernable (e.g., types of bedrock, degree of wind
41 exposure, abundance of metal-rich particles). Unlike the Frontier Mountain and Miller Butte
42 sedimentary traps, the size fraction below 240 μm indicates some degree of sorting at
43 Widerøefjellet, potentially through the redistribution by wind, preferential alteration of smaller
44 particles, or processing biases. However, the cosmic spherules larger than 300 μm appear largely
45 unbiased following their size distribution, frequency by textural type, and bulk chemical
46 compositions. Based on the available bedrock exposure ages for the Sør Rondane Mountains,
47 extraterrestrial dust is estimated to have accumulated over a time span of ~1 to 3 Ma at
48 Widerøefjellet. Consequently, the Widerøefjellet collection reflects a substantial reservoir to
49 sample the micrometeorite influx over this time interval. Petrographic observations and 3D
50 microscopic CT imaging are combined with chemical and triple-oxygen isotopic analyses of
51 silicate-rich cosmic spherules larger than 325 μm . The major element composition of 49 cosmic
52 spherules confirms their principally chondritic parentage. For 18 glassy, 15 barred olivine, and 11
53 cryptocrystalline cosmic spherules, trace element concentrations are also reported on. Based on
54 comparison with evaporation experiments reported in literature and accounting for siderophile and
55 chalcophile element losses during high-density phase segregation and ejection, the observed
56 compositional sequence largely reflects progressive heating and evaporation during atmospheric
57 passage accompanied by significant redox shifts, although the influence of (refractory) chondrite
58 mineral constituents and terrestrial alteration cannot be excluded in all cases. Twenty-eight cosmic
59 spherules larger than 325 μm analyzed for triple-oxygen isotope ratios confirm inheritance from
60 mostly carbonaceous chondritic precursor materials (~55% of the particles). Yet, ~30% of the
61 measured cosmic spherules and ~50% of all glassy cosmic spherules are characterized by oxygen
62 isotope ratios above the terrestrial fractionation line, implying genetic links to ordinary chondrites
63 and parent bodies currently unsampled by meteorites. The structural, textural, chemical, and

64 isotopic characteristics of the cosmic spherules from the Sør Rondane Mountains, and particularly
65 the high proportion of Mg-rich glass particles contained therein, imply a well-preserved and
66 representative new sedimentary micrometeorite collection from a previously unstudied region in
67 East Antarctica characterized by distinct geological and exposure histories.

68

69 *Keywords:* cosmic spherules; extraterrestrial dust; parent bodies; atmospheric heating; oxygen
70 isotope ratios.

71 **1. INTRODUCTION**

72 Micrometeorites (MMs), dust particles within the size range of 10 μm to 2 mm (Rubin and
73 Grossman, 2010), dominate the $40,000 \pm 20,000$ metric tons of extraterrestrial matter accreting to
74 Earth every year (Love and Brownlee, 1993). Due to different production mechanisms in and
75 transportation pathways from their source regions, these microscopic particles sample parent
76 bodies different from those of meteorites (e.g., Fredriksson and Martin, 1963; Ganapathy et al.,
77 1978; Engrand and Maurette, 1998; Flynn et al., 2009; Gounelle et al., 2009; Dartois et al., 2013;
78 Cordier and Folco, 2014; Rubin, 2018). Generally recovered from deep-sea sediments, seasonal
79 lakes in Greenland, ice and snow in Greenland and Antarctica, Antarctic moraines, continental
80 sands and soils, and more recently also urban environments (e.g., Brownlee et al., 1979; Blanchard
81 et al., 1980; Koeberl and Hagen, 1989; Hagen et al., 1989; Engrand and Maurette, 1998; Taylor
82 and Lever, 2001; Genge et al., 2016, 2017; Rudraswami et al., 2016; van Ginneken et al., 2017),
83 MMs have also been found concentrated in high-altitude sedimentary traps, i.e. pits, fissures and
84 cracks of glacially eroded surfaces, in the Transantarctic Mountains (TAM) (e.g., Rochette et al.,
85 2008; Suavet et al., 2009). To concentrate MMs in numbers sufficient to be able to efficiently
86 distinguish them from terrestrial particles in sedimentary deposits, the accumulation time of such
87 traps is ideally of the order of millions of years, while at the same time alteration must have
88 remained limited, with minimal background or anthropogenic contributions (Suavet et al., 2009).
89 In the case of the Antarctic collections from the Cap Prud'homme blue ice field, the Yamato
90 Mountain blue ice field, and the South Pole Water Well at the Scott-Amundsen Station (USA), the
91 sampled time intervals cover the last few kyr (Maurette et al., 1994), 27-33 kyr (Yada et al., 2004),
92 and 1100-1500 AD (Taylor et al., 1998, 2000), respectively. For the most recent flux of
93 extraterrestrial material to Earth, the MMs in central East Antarctica near the French-Italian
94 Concordia Station – Dome C recovered from the melting and filtering of snow are considered
95 among the most representative (Duprat et al., 2001, 2007; Gounelle et al., 2005; Dobrica et al.,
96 2010). However, significantly older Antarctic surface sediments have also been found enriched in
97 MMs, particularly the melted types (Hagen et al., 1989; Koeberl and Hagen, 1989; Harvey and
98 Maurette, 1991). In the case of the TAM, sedimentary traps yield exposure ages on the order of
99 several Ma (up to 4 Ma), linked to the high resistance of the bedrock to weathering and erosion.
100 This is based on cosmic spherule fluences in combination with unbiased flux rate estimates,
101 cosmogenic nuclide measurements of the exposed surface surrounding the trap, the occurrence of

102 ~0.8 Myr old microtektites, the presence of ~480 kyr old ablation debris related to a large
103 meteoritic airburst, and the paleomagnetic record of melted MMs (e.g., Folco et al., 2008, 2009;
104 Rochette et al., 2008; Welten et al., 2008; van Ginneken et al., 2010; Suavet et al., 2011b). The
105 TAM sedimentary traps have proven an exceptionally productive source, yielding several 1000s
106 MMs larger than 400 μm and 100s larger than 800 μm (e.g., Rochette et al., 2008; Suavet et al.,
107 2009).

108 Based on the degree of melting experienced during atmospheric passage, the distinction is
109 generally made between melted MMs (hereafter cosmic spherules, CSs), partially melted MMs (or
110 scoriaceous MMs), and unmelted or angular MMs (e.g., Maurette et al., 1994; Taylor et al., 1998;
111 Genge et al., 2008). Cosmic spherules form after significant melting of micrometeoroids during
112 atmospheric passage and subsequent cooling (Folco and Cordier, 2015). Cosmic spherules are
113 distinct from meteorite ablation spheres, which are quenched melt droplets separated from the
114 fusion crust of macroscopic meteorites. The latter can often be differentiated from CSs based on
115 their lower cosmic-ray induced ^{26}Al and ^{10}Be contents and higher volatile element (mainly alkali
116 metal) content (Raisbeck et al., 1986; Genge and Grady, 1998; van Ginneken et al., 2010).

117 In this work, a new sedimentary MM collection from mount Widerøefjellet in the Sør Rondane
118 Mountains (SRM) of Dronning Maud Land in eastern Antarctica is documented, and the
119 physicochemical characteristics of the deposits and most obvious CSs larger than 200 μm are
120 compared to those of the TAM and other MM collections. As CSs dominate the MM influx in the
121 size fraction larger than 50 μm , constituting a representative subpopulation for the entire MM flux
122 (e.g., Brownlee et al., 1997; Taylor et al., 2012; Cordier and Folco, 2014), a fraction of the largest
123 CSs recovered from Widerøefjellet has been characterized for major ($n = 49$) and trace ($n = 44$)
124 element concentrations, as well as for high-precision oxygen isotopic compositions ($n = 28$), after
125 structural characterization by μCT . While the textures and chemical compositions of
126 extraterrestrial particles are reprocessed by alteration during their terrestrial residence, this work
127 focuses on confirming the primary nature of the MM precursor materials and refining the processes
128 that affected these particles during atmospheric passage. While there is convincing evidence, based
129 on elemental compositions and oxygen isotope ratio studies (e.g., Genge et al., 1997; Noguchi et
130 al., 2002), that a large fraction of the MMs is related to carbonaceous chondrites of various clans
131 and groups, the ratio of MMs related to ordinary as compared to carbonaceous chondrites and their
132 distribution per size fraction, is currently based on only a limited number of analyses, especially

133 for the larger size fractions (e.g., Steele, 1992; Kurat et al., 1994; Brownlee et al., 1997; Engrand
134 and Maurette, 1998; Engrand et al., 2005; Gounelle et al., 2005; Genge et al., 2008; Suavet et al.,
135 2010; Cordier et al., 2011a, 2011b; Taylor et al., 2012; Rudraswami et al., 2012, 2015a, 2015b,
136 2016; van Ginneken et al., 2012, 2017; Imae et al., 2013; Cordier and Folco, 2014). The ratio of
137 carbonaceous chondrite relative to ordinary chondrite material decreases as CS diameters increase,
138 from a factor of 10 for small particles ($< 500 \mu\text{m}$ in diameter) to a factor of 0.3 for larger particles,
139 indicating that the contribution of ordinary chondrite material to the composition of the
140 micrometeoroid complex increases with MM size, with a possible continuum between meteorites
141 and MMs (Cordier and Folco, 2014). The present study provides an independent assessment of the
142 flux of large ($> 200 \mu\text{m}$) micrometeoroids over the last ~ 3 Ma and a means to evaluate the relative
143 contributions of primitive asteroids (and comets) compared to more evolved asteroids within the
144 interplanetary dust cloud.

145 2. MATERIALS AND METHODS

146 2.1. Sedimentary micrometeorite traps in the Sør Rondane Mountains

147 The Sør Rondane Mountains (SRM) within Dronning Maud Land of East Antarctica cover a
148 surface area of approximately 2000 km², mainly composed of low- to high-grade metamorphic
149 lithologies that were intruded by various plutonic rocks (e.g., Shiraishi et al., 1997). Sensitive high-
150 resolution ion microprobe U-Pb zircon ages indicate that the last tectonothermal event in the SRM
151 range took place 650-500 Myr ago, after which the SRM have remained geologically stable
152 (Shiraishi et al., 2008). Ice sheet surfaces reach an elevation of about 1000 meter above sea level
153 (masl) north of the SRM and rise to 2500 masl to the South (Suganuma et al., 2014). The region
154 surrounding the Belgian Princess Elisabeth Antarctica (PEA) station was studied using satellite
155 images and geological maps before the start of the 2012-2013 field campaign (Imae et al., 2015).
156 Based on descriptions of the TAM traps (e.g., Rochette et al., 2008; Suavet et al., 2009), erosional
157 and eolian sediment, expected to contain significant extraterrestrial contributions, was
158 subsequently sampled from exposed cracked and fissured surfaces at wind-exposed, high altitude
159 (>2000 masl) granitoid summits in the western part of the SRM (Fig. 1 and 2). The current work
160 focuses on CSs separated from a single batch of ~6.6 kg detritus collected at Widerøefjellet (~2755
161 masl; S72°8'41", E23°16'41"). The main lithotype found at Widerøefjellet is a gneissose biotite-
162 hornblende metatonalite, geochemically categorized as a low-K tholeiitic intrusion in volcanic arc
163 granitoids (Kamei et al., 2013; Kojima and Shiraishi, 1986).

164 Limited information exists on the deglaciation history of the Widerøefjellet peak, as fully
165 exposed or glacially abraded bedrock surfaces suitable for cosmogenic dating methods are lacking
166 near the sampled sediment trap. However, an abraded coherent surface showing glacial striations
167 on the granitoid Walnumfjellet in the western central part of the SRM (Fig. 1), 30 km East of
168 Widerøefjellet at 2489 masl (S72°04'57", E24°17'16"), indicates a ¹⁰Be exposure age of 1.9±0.2
169 Ma after correction for glacial isostatic adjustment (Suganuma et al., 2014). This exposure age is
170 in agreement with the general glacial history for the western part of the Sør Rondane Mountains,
171 as interpreted based on the height and degree of weathering of tills (Moriwaki et al., 1991) that
172 were correlated to absolute ¹⁰Be and ²⁶Al exposure ages (Nishiizumi et al., 1991). Prior to 4 Ma, a
173 large part of the SRM was covered with an ice sheet that retreated progressively with some pauses
174 prior to 1 Ma, was stagnant or re-advanced after 1 Ma, and subsequently retreated to nearly the
175 same level as at present until ten thousand years ago (Moriwaki et al., 1991). The summit height

176 and degree of weathering in the western part of the Sør Rondane Mountains correspond to an
177 exposure age of ~1 to 3 Ma. The Walnumfjellet exposure age is taken here as a workable
178 approximation for the deglaciation history of Widerøefjellet, until more precisely constrained.
179 Given the annual mean air temperature of approximately -19°C at the PEA research station (1390
180 masl; Pattyn et al., 2010; Gorodetskaya et al., 2013), the Widerøefjellet sediment, which lies at
181 altitudes more than 1350 m higher than PEA, is assumed to mostly have remained below freezing
182 point since the time of exposure. In the TAM deposits, which lie at 2600 masl (Folco et al., 2008),
183 extraterrestrial particles have clearly been exposed to liquid water (e.g., van Ginneken et al., 2016),
184 suggesting that melting may occur at high altitudes and ambient temperatures well below 0°C.
185 However, contact with liquid water appears to have been less pervasive at Widerøefjellet based on
186 the observed degree of weathering and the type of weathering minerals found on the CSs (cf.
187 below).

188

189 **2.2. Collection, sampling, and first classification**

190 After removal of the largest rock fragments and boulders, 6.6 kg of Widerøefjellet sediment
191 was sampled using dedicated polypropylene and wooden sampling tools, to avoid contamination
192 by metal (Fig. 1 and 2). The sediment was gradually defrosted at temperatures only slightly
193 exceeding the freezing point at the PEA station. After sample splitting, about half of the sediment
194 (3.2 kg) was processed by washing in milli-Q H₂O and sieving at the Vrije Universiteit Brussel
195 (VUB, Belgium) to separate size fractions of less than 125 µm, 125-200 µm, 200-400 µm, 400-
196 800 µm, 800-3000 µm, and more than 3000 µm, while the remaining half is kept for reference.
197 Using optical microscopy, 2099 CSs were handpicked from the >200 µm size fractions of the
198 Widerøefjellet deposit, with 1707 CSs extracted from the 200-400 µm, 375 CSs from the 400-800
199 µm, and 17 CSs from the 800-3000 µm size fractions. No extraterrestrial particles were found in
200 the >3000 µm size fraction, while the smaller fractions and unmelted particles remain the subject
201 of further study. For 985 randomly picked CSs, the surface textural and compositional
202 characteristics were determined using a JEOL JSM-IT300 or field emission JEOL JSM-7000F
203 scanning electron microscope (SEM), both equipped with energy-dispersive X-ray spectrometers
204 (EDS), at the VUB. Cosmic spherules are traditionally divided into three compositional types
205 following their main mineralogy: the silicate-rich (S-type) spherules, the iron-rich (I-type)
206 spherules, and the G-type spherules, which represent an intermediate class (e.g., Blanchard et al.,

207 1980; Taylor et al., 2000; Genge et al., 2008). Stony or silicate CSs are commonly further
208 subdivided into four types based on quench textures, i.e. porphyritic (Po-type), cryptocrystalline
209 (CC-type), barred olivine (BO-type) and glass or vitreous (V-type) spherules (Taylor and
210 Brownlee, 1991; Taylor et al., 2000, 2007a; Genge et al., 2008, 2018). Recently, this classification
211 has been expanded to include a microporphyritic type (μ PO-type), as the μ PO CSs appear to derive
212 from a parent body distinct to the Po-type spherules (van Ginneken et al., 2017). Back-scattered
213 electron images for examples of the various textural groups of silicate CSs are shown in Fig. 3.
214 Using optical microscopy, SEM and/or μ CT (cf. below), the diameters for a fraction of the
215 extracted CSs were determined. Figure 4 illustrates the size distribution of the Widerøefjellet CS
216 collection and compares the size distributions of the subgroups of CSs characterized using different
217 analytical techniques.

218

219 **2.3. Micro computer-assisted X-ray tomography (μ CT)**

220 From these 985 CSs, 45 particles in the 200-400 μ m size fraction and 101 particles in the 400-
221 800 μ m size fraction were analyzed using the HECTOR (High-Energy μ CT system Optimized for
222 Research) X-ray scanner at the Centre for X-ray Tomography of Ghent University (Supplementary
223 Fig. S1). This instrument is equipped with a 240 kV X-ray tube from X-RAY WorX and a
224 PerkinElmer 1620 flat-panel detector of 2048x2048 pixels (Masschaele et al., 2013). The beam
225 was operated at 15 kV with 90 minutes of exposure time per scan. Because of the size and number
226 of MMs, packets of up to 50 particles were scanned simultaneously. Because of the variable total
227 scanned volume, this set-up generated transmission images with a pixel size of 2 x 2 μ m² and 4 x
228 4 μ m² for the 400-800 μ m and 200-400 μ m particles, respectively. The Octopus Reconstruction
229 software (Masschaele et al., 2007; Vlassenbroeck et al., 2007) was used to transform the acquired
230 μ CT data into a stack of 2D image slices that were consequently processed into 3D models using
231 the open source program 3dmod Version 4.5.8. For the latter, the voxel size of the reconstructions
232 was preferred to approximate the pixel size and ranged from 2 μ m x 2 μ m x 2 μ m to 4 μ m x 4 μ m
233 x 4 μ m. A selection of 3D μ CT models is presented in Fig. 5, while examples of 2D μ CT slices
234 are shown in Supplementary Fig. S2.

235

236 **2.4. Major and trace element analysis**

237 Following the acquisition of the μ CT images, 49 CSs, ranging between 439 and 916 μm , were
238 arbitrarily selected from the larger size fractions and mounted in epoxy resin (PolyfastTM) under
239 vacuum conditions and polished using silicon carbide paper with 1200 to 4000 grit (mesh) size.
240 The exposed interiors of the spherules were subsequently polished with diamond paste in an
241 alcohol-based suspension (particle sizes 6, 3 and 1 μm) on a synthetic cloth, and carbon-coated
242 prior to further textural and chemical characterization using the SEM-EDS systems at VUB and
243 electron microprobe (EMP) at the Natural History Museum (NHM) in Vienna, Austria.
244 Quantitative wavelength-dispersive X-ray spectrometric (WDS) analyses were performed with a
245 field emission gun electron microprobe analyser (EMPA) JEOL Hyperprobe JXA 8530F in the
246 Central Laboratory at the NHM. Between 2 and 19 EMPA data points were gathered for relatively
247 homogeneous particles (V- and CC-type), while more analyses were carried out for CSs with
248 significant heterogeneity, with up to 50 points for BO- and Po-type CSs. In each CS, olivine, glass,
249 metal and magnetite phases were examined and averaged proportional to their abundances
250 estimated from SEM images using image processing software to obtain bulk compositions. Note
251 that this methodology depends on the CS section obtained and the phase contrasts within individual
252 particles but can in part be validated through the subsequent laser ablation – inductively coupled
253 plasma – mass spectrometry (LA-ICP-MS) analysis (cf. below). Operating conditions included an
254 accelerating voltage of 15 kV, a beam current of 20 nA with WDS and EDS (Bruker), and a
255 counting time of 10 s for the peak and 5 s for the background for all element K_{α} lines. The spot
256 size was varied from 0.07 μm (fully focused, in the case of spatially limited phases) to 2 μm .
257 Synthetic compounds Al_2O_3 , Cr_2O_3 , TiO_2 , NiO , NaCl , KCl and natural minerals vanadinite
258 $\text{Pb}_5(\text{VO}_4)_3\text{Cl}$, tephroite Mn_2SiO_4 , wollastonite CaSiO_3 , Durango apatite $\text{Ca}_5(\text{PO}_4)_5\text{F}$ and Marjalahti
259 olivine $(\text{Mg,Fe})_2\text{SiO}_4$ were used for calibration of Al, Cr, Ti, Ni, Na, K, V, Mn, Ca, P, Mg, Si, and
260 Fe, respectively. The data reduction was carried out using the on-line ZAF-corrections provided
261 by JEOL. The mean detection limits (LOD, in wt% and ppm) for the measured oxides (with
262 standard deviation for the LOD in ppm), calculated from 50 analysis points on glass and olivine,
263 are presented in Supplementary Table S1. The analytical precision for major elements (Si, Mg and
264 Fe) is typically better than 1% relative standard deviation (RSD) based on repeated measurements
265 of calibration standards and V-type CSs, but the total uncertainty associated with the EMPA
266 analysis, due to sample heterogeneity, is estimated to be 2-5% RSD for BO-, CC-, and Po-type
267 CSs. For the analyzed minor and trace elements (Ti, Cr, Mn, Na, K, P, V and Ni), the total

268 uncertainty associated with the EMP analysis is calculated to be on the order of 5-15% RSD, taking
269 the presence of olivine and magnetite phenocrysts and changes in the composition of the
270 interstitial glass into account. The major element data obtained using EMPA are summarized in
271 Table 1 and Supplementary Table S1.

272 Selected major and trace element concentrations were determined by means of LA-ICP-MS
273 analysis using a Teledyne Photon Machines (Bozeman, MT, USA) Analyte G2 ArF* excimer-
274 based LA system coupled to a Thermo Scientific Element XR double-focusing sector field ICP-
275 mass spectrometer at the Department of Chemistry of Ghent University, following the procedures
276 outlined in Martin et al. (2013) and Van Roosbroek et al. (2015). Using a repetition rate of 30 Hz
277 and energy density of $\sim 8.27 \text{ J/cm}^2$, each CS was ablated multiple times for 15 s using a laser spot
278 size of 50 μm . The 18 V-type CSs were each ablated on 2 to 4 locations, while 15 BO-type and 11
279 CC-type CSs were all ablated on 2 to 3 locations, making sure no visibly recognizable vesicles or
280 high-density phases were targeted. The Po-type CSs were not analyzed for trace elements because
281 of potential biases linked to individual mineral crystals.

282 Replicates were compared to ensure similar phases were sampled by monitoring signal
283 intensities for the major elements Mg, Si, Ca, and Fe. Quantification was achieved through external
284 calibration against multiple certified reference materials produced by the United States Geological
285 Survey (USGS) and the National Institute of Standards and Technology (NIST), i.e. natural
286 basaltic glasses USGS BCR-2G, USGS BHVO-2G, USGS BIR-1G, natural nephelinite glass
287 NKT-1G, and synthetic glasses USGS GSC-1G, USGS GSD-1G, USGS GSE-1G, NIST SRM
288 610, and NIST SRM 612, using ^{29}Si as an internal standard. Based on the reference materials, the
289 reproducibility for the reported elements is typically of the order of 5-10% RSD. The trace element
290 data obtained for the different textural and chemical CS groups are summarized in Table 1, while
291 the data for individual CSs are also presented in Supplementary Table S1.

292

293 **2.5. High-precision oxygen isotope ratio measurements**

294 Measurements of $\delta^{18}\text{O}$ and $\delta^{17}\text{O}$ were carried out on 28 CSs, randomly selected from the same
295 fraction from which the CSs were prepared for major and trace element concentrations
296 (Supplementary Fig. S1), using infrared laser-assisted (IR) fluorination isotope ratio mass
297 spectrometry (IRMS) at the Open University in Milton Keynes, UK (Miller et al., 1999;
298 Greenwood et al., 2017). The particles had diameters between 357 and 735 μm and were studied

299 using SEM-EDS and μ CT beforehand (Supplementary Fig. S1). Figure 3 includes back-scattered
300 electron images for a selection of the silicate CSs characterized for oxygen isotope ratios.
301 Supplementary Fig. S3 indicates that the atomic Mg-Si-Fe data based on SEM-EDS for these
302 particles fall within or close to the compositional range determined for CSs from other Antarctic,
303 Greenland, and deep-sea collections (Taylor et al., 2000). As most of the selected CSs showed
304 limited degrees of chemical alteration, no fracturing, and no encrustation by secondary phases
305 based on binocular microscopy and BSE imaging (cf. below; Fig. 3; Table 2), the particles of
306 interest were washed in acetone to remove adhesive material, but not acid-leached. Following
307 weighing and loading, oxygen was released from the samples by reaction with BrF_3 . After
308 fluorination, the released oxygen was purified by passing the gas through two cryogenic nitrogen
309 traps and over a bed of heated KBr. The oxygen three-isotopic composition was determined using
310 a MAT 253 dual-inlet IRMS unit. Oxygen isotope ratios are reported in standard δ notation, where
311 $\delta^{18}\text{O}$ is calculated as $\delta^{18}\text{O} = [({}^{18}\text{O}/{}^{16}\text{O})_{\text{sample}}/({}^{18}\text{O}/{}^{16}\text{O})_{\text{ref}} - 1] \times 1000$ (‰) and $\delta^{17}\text{O}$ using the ${}^{17}\text{O}/{}^{16}\text{O}$
312 ratio, relative to Vienna Standard Mean Ocean Water (V-SMOW; Table 2). To allow comparison
313 to previously published data, $\Delta^{17}\text{O}$, which represents the deviation from the terrestrial fractionation
314 line (TFL), is calculated as $\delta^{17}\text{O} - 0.52 \times \delta^{18}\text{O}$ (Clayton, 1993). Accuracy and analytical precision
315 of the method were validated by replicate analysis of international reference materials (NBS-28
316 quartz and UWG-2 garnet; Miller et al., 1999). Based on repeated measurement of an in-house
317 obsidian standard, the results for subsamples with masses between 0.062 and 0.193 mg ($n = 21$;
318 3.69 ± 0.21 ‰ for $\delta^{17}\text{O}$; 7.09 ± 0.42 ‰ for $\delta^{18}\text{O}$; 0.006 ± 0.035 ‰ for $\Delta^{17}\text{O}$; 2σ) show a slight systematic
319 offset and decreased precision compared to the values obtained for larger subsamples of ~ 2 mg (n
320 $= 39$, 3.81 ± 0.05 ‰ for $\delta^{17}\text{O}$; 7.27 ± 0.09 ‰ for $\delta^{18}\text{O}$; 0.029 ± 0.017 ‰ for $\Delta^{17}\text{O}$; 2σ). This offset has
321 been observed during previous analytical campaigns as well and may result from isotopic
322 fractionation associated with the transfer of gas in the inlet system (e.g., Greenwood et al., 2007;
323 Suavet et al., 2010; Cordier et al., 2011b). As the precision obtained for the small obsidian
324 subsamples reflects the typical analytical uncertainties associated with MM analysis and the
325 determined values for the small obsidian subsamples overlap within uncertainty with those of
326 larger subsamples, no additional (bias) corrections were carried out. The results of the oxygen
327 isotope measurements are summarized in Table 2, together with information on the textural group,
328 apparent diameter and mass, and degree of alteration of as well as the presence of vesicles and
329 high-density phases in the selected particles.

330 3. RESULTS

331 3.1. Textural classification and cumulative size distribution

332 Following SEM-EDS and μ CT analysis, a selection of particles, including whole CSs and
333 sectioned particles, were classified according to their mean bulk compositions and textural
334 characteristics (Tables 1-3; Supplementary Fig. S1; Supplementary Table S1). The majority of
335 CSs larger than 200 μ m in the Widerøefjellet collection belong to the stony, S-type CSs (95% by
336 number). The iron (I-type, 3%) and mixed stony-iron (G-type, 2%) types represent only small
337 contributions to the fractions analyzed. These contributions are similar to what is observed for the
338 TAM collections (3% I-type and 1% G-type particles; Suavet et al., 2009; Table 3). Unmelted and
339 scoriaceous MMs have been observed but are relatively uncommon (< 5%) and difficult to
340 distinguish from mafic background mineral contributions. Of 109 randomly sampled CSs larger
341 than 400 μ m, 95% are classified as S-type (33% as V-subtype), while the G- and I-type spherules
342 contribute 1% and 4%, respectively. A comparable distribution is observed for 228 different
343 particles larger than 200 μ m, of which 95% are classified as S-type (27% as V-subtype), with 2%
344 and 3% contributions to the G- and I-type CSs, respectively (Table 3). The CSs studied for
345 elemental and oxygen isotopic composition exhibit similar distributions between the textural CS
346 groups. Of the 49 particles studied for major and trace elements, 18 (37%) are classified as V-type,
347 15 (31%) as BO-type, 11 (22%) as CC-type, while 5 (10%) are Po-type (Fig. 3; Table 1;
348 Supplementary Table S1). In the case of the latter, an additional CS subtype is distinguished, the
349 μ PO-type CSs, which are mainly composed of euhedral submicron olivine crystals and are highly
350 vesicular relative to normal Po-type CSs (Fig. 3; van Ginneken et al., 2017). Of the CSs
351 characterized for oxygen isotope ratios, 10 (36%) represent V-type spherules, 7 (25%) are BO-
352 type, 6 (21%) are CC-type, 1 (4%) belongs to the Po-type, 1 (4%) belongs to the μ Po-type, while
353 a single subangular, vesicular particle with dendritic and skeletal spinel crystals is classified as
354 irregular (4%) and 2 are designated as BO/CC-type mixtures (7%; Table 2).

355 The diameters of the individual CSs studied here have been determined combining optical
356 microscopy, SEM and μ CT (Table 2; Supplementary Table S1). Similar to the work of Suavet et
357 al. (2009), the particles are assumed to represent ellipsoids with equal minor and intermediate axes
358 ($a > b = c$). As such, the diameters used in the size distribution are defined as $d_{\text{ellipsoid}} = (a \times b^2)^{1/3}$,
359 where $d_{\text{ellipsoid}}$ represents the reported diameter of the CSs (Table 2; Supplementary Table S1). Due
360 to the sieving process, particles may fall outside of their size fraction. As a result, a larger size

361 fraction may contain CSs with diameters slightly below the mesh size, while conversely particles
362 larger than the mesh size may pass into smaller mesh size sieves due to elongated shapes or mesh
363 imperfections (e.g., Rochette et al., 2008). In Fig. 4A, the cumulative size distribution for
364 Widerøefjellet CSs larger than 200 μm is plotted, displaying the number N of CSs larger than a
365 certain diameter. A similar curve for a subpopulation of TAM particles larger than 400 μm , for
366 which the unprocessed diameters were provided, is shown for comparison (Suavet et al., 2009).
367 The size distributions for the CSs separated for chemical and oxygen isotopic analyses are plotted
368 in Fig. 4B. Both subgroups of analyzed CSs display similar size distributions.

369

370 **3.2. Metal and vesicle content**

371 Based on the μCT scans (2D slices and 3D volumes) and sectioned SEM images (2D slices),
372 vesicles, Fe–Ni metal beads, sulfides, and/or other inclusions with contrasting densities (including
373 spinel group minerals) can be detected (Table 2; Fig. 5; Supplementary Table S1; Supplementary
374 Fig. S2). Using the applied μCT system, the distinction between silicate glass and olivine cannot
375 be made in most cases, due to the similar X-ray attenuation of these phases and the often small
376 sizes (mostly $< 10 \mu\text{m}$) of olivine crystals in BO-, CC, and Po-type CSs. Rarely, Po-type CSs are
377 characterized by large enough olivine crystals (larger than 10 μm and up to 150 μm in size;
378 Supplementary Fig. S2B) to be distinguished on μCT scans (e.g., WF1202B-0006, 0036, 0137,
379 0202). In various CSs (WF1202B-0013, 0028, 0042, 0050, 0120, 0114), μCT scans reveal internal
380 structures on BO-type CSs that may be related to crystal orientation, although indicative lines can
381 also be generated through interference patterns. The lower size range of vesicles and high-density
382 phases is limited by the spatial resolution obtained for the μCT system applied. Vesicles range in
383 diameter from $<10 \mu\text{m}$ to $\sim 200 \mu\text{m}$, while high-density phases vary between $<15\text{-}20 \mu\text{m}$ and ~ 100
384 μm (Fig. 5; Supplementary Fig. S2).

385 Based on the data for 146 CSs, only in part validated through 2D sections for a subset of these
386 particles studied using SEM-EDS (Supplementary Table S1), the distinction can be made between
387 groundmass silicate phases, high-density phases, which may include rounded Fe–Ni metal (often
388 as metal beads), irregular sulfides, rounded to angular spinel group mineral phases, or
389 micrometeorite-sized platinum group element nuggets (e.g., Brownlee et al., 1984; Taylor et al.,
390 2000; Rudraswami et al., 2011; Cordier et al., 2011b), and vesicles. While most CSs with high-

391 density phases contain only a single inclusion, multiple high-density phases, presumably FeNi
392 metal beads, can be encountered, with up to five metal-rich inclusions within a single particle (e.g.,
393 WF1201B-0129; Supplementary Fig. S2).

394 Approximately 46% of the CSs between 200 and 800 μm contains no vesicles or high-density
395 inclusions (Fig. 5; Supplementary Fig. S4A). Second most abundant ($\sim 23\%$) are CSs with high-
396 density phases but no vesicles, while CSs with vesicles, but no high-density inclusions, contribute
397 $\sim 22\%$ to the studied Widerøefjellet CSs. Least abundant ($\sim 9\%$) are the CSs with both vesicles and
398 high-density phases. No significant differences are observed between the studied CSs in the 200-
399 400 μm and 400-800 μm size fractions, with the exception of a higher relative abundance of CSs
400 with no vesicles and high-density phases in the 400-800 μm fraction relative to the 200-400 μm
401 fraction (Supplementary Fig. S4A). When combining μCT data with textural information
402 (Supplementary Fig. S4B), V-, BO- and Po-type CSs are dominated by particles with no vesicles
403 or high-density phases ($>57\%$), while only 14% of Po-type CSs fall in this category. In the case of
404 Po-type CSs, particles with vesicles prevail, either with (43%) or without (43%) high-density
405 phases. Based on these abundances, relict grain survival, vesicle formation and high-density phase
406 segregation are linked to different degrees of atmospheric heating.

407

408 **3.3. Major element composition**

409 V-type CSs ($n = 18$) show the largest compositional variations in terms of Al, Mg, and Ca (i.e.
410 0.86-31.3 wt% Al_2O_3 , 3.73-48.5 wt% MgO, and 0.78-18.7 wt% CaO; Table 1; Supplementary
411 Table S1). These ranges are comparable to or larger than those reported for 187 V-type CSs from
412 the TAM collection, with 0.06-14.1 wt% Al_2O_3 , 0.85-43.0 wt% MgO, and 0.04-11.9 wt% CaO
413 (Cordier et al., 2011b). For the CSs studied here, the largest range in SiO_2 , Cr_2O_3 , and FeO^* (all
414 Fe reported as FeO) concentrations is observed for BO-type spherules (Supplementary Table S1).
415 The SiO_2 concentrations of V-type CSs display a range of 39.7 to 50.5 wt%, while SiO_2 contents
416 vary between 27.4 and 42.4 wt%, 36.9 and 47.0 wt%, and 40.5–46.2 wt% for BO-type ($n = 15$),
417 CC-type ($n = 15$), and Po-type ($n = 5$) CSs, respectively, partly overlapping (average values with
418 1 SD can be found in Table 1). On average, BO-type CSs contain higher bulk Fe contents than
419 their CC-type and Po-type textured counterparts, with 28.2 wt% FeO^* for BO-type versus 17.0
420 and 18.0 wt% FeO^* for CC-type and Po-type CSs, respectively (Table 1; Supplementary Table
421 S1). CC-type and Po-type CSs generally display comparable major element compositions,

422 although Po-type CSs often show higher Ni contents (1.3 wt.% NiO on average) relative to other
423 textural types (less than 0.3 wt.% NiO on average for V-type, BO-type, and CC-type CSs based
424 on EMPA data; Table 1; Supplementary Table S1). To highlight possible extraction biases, the
425 molar Fe/(Si + Mg) ratios of the Widerøefjellet particles are compared to those of particles from
426 various other collections (Fig. 6). On Mg-Si-Fe and K+Na-Ca-Al ternary diagrams, the SRM
427 particles plot within the compositional ranges of CSs defined in the literature (e.g., Brownlee et
428 al., 1997; Taylor et al., 2000; Rochette et al., 2008; Fig. 7). The extraterrestrial field is clearly
429 distinct from literature data for Antarctic volcanic rocks and tephra. All particles studied for major
430 and minor elements contain less than 0.35 wt% Na₂O, 0.06 wt% K₂O, and 51 wt% SiO₂, making
431 these CSs distinct from volcanic glass shards, microtektites or meteorite ablation debris (e.g.,
432 Cordier et al., 2011b; Folco and Cordier, 2015).

433 All CSs characterized here exhibit relatively chondritic Mn/Mg ratios with positively correlated
434 Fe/Mg and Fe/Mn ratios (Fig. 8A). This suggests that no particles from differentiated or basaltic
435 precursors were sampled, as particles from differentiated parent bodies are often marked by higher
436 Fe/Mg but similar Fe/Mn ratios relative to chondrites plotting along the horizontal lines marked
437 “Moon” and “4Vesta/Mars” in Fig. 8A (e.g., Goodrich and Delaney, 2000; Taylor et al., 2007a;
438 Gounelle et al., 2009; Cordier et al., 2011a, b, 2012; Cordier and Folco, 2014). Based on the
439 atomic Fe/Si ratio and CaO and Al₂O₃ contents, chondritic CSs have previously been assigned to
440 three distinct chemical groups (Cordier et al., 2011b): (i) the normal group containing most
441 chondritic CSs, (ii) the Ca-Al-Ti-rich (CAT-like) group with Fe/Si < 0.06, Mg/Si > 0.9 (at.%) and
442 CaO + Al₂O₃ > 5 wt.%, and (iii) the high Ca-Al group with Fe/Si > 0.06 (at.%) and CaO + Al₂O₃
443 > 9 wt.% (Fig. 8B). This classification extends and refines the chemical characteristics (low Fe/Si
444 and high Mg/Si ratios) of the previously identified “CAT” group, defined by Taylor et al. (2000)
445 and Alexander et al. (2002). Applying the criteria defined above, 6 (12%) of the CSs studied here
446 belong to the CAT-like group (V-type WF1202B-0010, 0029 and 0048, BO-type WF1202B-0002
447 and 0016, CC-type WF1202B-0037; Supplementary Table S1), while 4 of these 49 CSs (8%) can
448 be classified as high Ca-Al spherules (V-type WF1202B-0001 and 0020, CC-type WF1202B-
449 0011, BO-type WF1202B-0038). It should be noted that high Ca-Al particle WF1202B-0038 is
450 also characterized by a high TiO₂ content of 0.36 wt%, perhaps rendering this classification scheme
451 incomplete. Both CAT-like and high Ca-Al particles are thus represented among all textural CS
452 groups, excepting Po-type CSs. While the abundance of high Ca-Al particles is comparable to that

453 observed in the V-type CS population of the TAM collection (10%), CAT-like particles are
454 significantly less abundant in the V-type subpopulation of the TAM collection (~2%; Cordier et
455 al., 2011b). As the V-type CSs in the latter work are comparable in size (220 to 850 μm) to the
456 Widerøefjellet particles studied here, the higher abundance of CAT-like particles here indicates a
457 higher proportion of such CSs among the non-glassy textural groups.

458

459 **3.4. Trace element composition**

460 The CSs studied exhibit a large diversity in REE contents and patterns (Fig. 8C, 9, 10, 11),
461 which are difficult to relate to any particular chemical or textural group. On average, the V-type,
462 BO-type, and CC-type textural groups show fully chondritic REE ratios and superchondritic
463 concentrations ($\text{La}/\text{Yb}_\text{N}$ of 1.0, 1.2, and 0.95, Eu^* of 1.6, 1.1, and 1.0, average REE_N of 3.0, 3.0,
464 and 2.3 for V-, BO-, and CC-type, respectively; Table 1). CC-type CSs exhibit the least variable
465 REE patterns, while BO-type CSs display the most pronounced Ce depletions, with a mean Ce^*
466 of 0.84 (with $\text{Ce}^* = \text{Ce}_\text{N} / \sqrt{[\text{La}_\text{N} * \text{Nd}_\text{N}]}$), compared to mean Ce^* of 1.0 and 0.92 for V- and CC-
467 type CSs, respectively. These Ce anomalies in BO-type spherules are mostly inherited from CAT-
468 like and high Ca-Al group CSs (mean Ce^* of ~0.36 for CAT-like WF1202B-0002 and 0016, and
469 high Ca-Al WF1202B-0038; Fig. 11). Based on the fractionation observed between light, medium,
470 and heavy REEs, in combination with the presence or absence of Ce and Eu anomalies (defined
471 based on $\text{Eu}^* = \text{Eu}_\text{N} / \sqrt{[\text{Sm}_\text{N} * \text{Gd}_\text{N}]}$), seven different REE patterns can be recognized among the
472 CSs characterized in this work ($n = 44$; Fig. 9A-F; Supplementary Table S1): (A) CSs with flat
473 patterns ($\text{La}/\text{Yb}_\text{N} = 0.7\text{-}1.4$; $\text{Eu}^* = 0.8\text{-}1.3$; $n = 29$). These CSs make up 82% of the CC-type, 75%
474 of the BO-type, and 50% of the V-type spherules. Most of these CSs exhibit fully chondritic REE
475 patterns ($\text{Ce}^* \sim 0.7\text{-}1.2$), while two CAT-like BO-type spherules show strong Ce depletions with
476 Ce^* of less than 0.3 (WF1202B-0002 and 0016). (B) One BO-type CS (WF1202B-0040) shows a
477 flat REE pattern with a negative Eu anomaly ($\text{La}/\text{Yb}_\text{N} = 0.9$; $\text{Eu}^* = 0.6$). (C) Eight CSs, mostly V-
478 type (75%), are characterized by a flat REE pattern with positive Eu anomaly ($\text{La}/\text{Yb}_\text{N} = 0.6\text{-}1.2$;
479 $\text{Eu}^* = 1.4\text{-}4.6$). One of the V-type CSs of this group (WF1202B-0017) exhibits a positive Ce
480 anomaly (Ce^* of 2.0 compared to 0.8-1.1 for the other CSs with this type of pattern). (D) One CC-
481 type CS (WF1202B-0011) exhibits a LREE-depleted pattern ($\text{La}/\text{Yb}_\text{N} = 0.5$; $\text{Eu}^* = 0.8$). (E) Two
482 V-type spherules (WF1202B-0019 and 0039) show LREE-depleted patterns with positive Eu
483 anomalies ($\text{La}/\text{Yb}_\text{N} = 0.5$; $\text{Eu}^* = 1.6\text{-}2.7$). (F) One V-type (WF1202B-0001) and one BO-type

484 (WF1202B-0013) CS are characterized by LREE-enriched patterns with negative Eu anomalies
485 ($\text{La}/\text{Yb}_N = 2.6\text{-}3.8$; $\text{Eu}^* = 0.6\text{-}0.7$). The BO-type CS also shows a slight negative Ce anomaly (Ce^*
486 of 0.6). (G) BO-type CS WF1202B-0042 exhibits a LREE-enriched pattern with a positive Eu
487 anomaly ($\text{La}/\text{Yb}_N = 2.1$; $\text{Eu}^* = 2.5$).

488 The chemical groups of CSs also vary in their trace element compositions (Table 1; Fig. 8-11).
489 The mean values for the chemical CS groups determined in this work indicate excellent
490 correspondence to the group averages compiled in literature based on particles from different MM
491 collections (Table 1; Fig. 10; Folco and Cordier, 2015). Relative to CI chondrites, the normal group
492 exhibits an enrichment in refractory elements (50% condensation temperatures above 1360 K),
493 excluding siderophile W and chalcophile V as well as redox-sensitive Th and U, to values of ~ 1.5
494 to 2.3, with a mean REE_N equal to 1.9 ± 1.2 times CI (1 SD; $n = 34$; Fig. 10). On average, the
495 siderophile elements W, Ni, and Co and chalcophile elements V and Cr are depleted by
496 approximately one order of magnitude relative to refractory elements, although particular CSs
497 show element depletions by four orders of magnitude. The flat refractory element patterns of these
498 CSs are occasionally also interrupted by both positive and negative anomalies in Sc, Y, Th, U, Ta,
499 Nb, and Ce, but on average most of these elements, except for Th, U, and Ce, are not depleted
500 relative to chondrites and exhibit chondritic ratios (Fig. 10). Mean positive Th and U anomalies
501 were previously not observed for V-type spherules (Cordier et al., 2011b), but can be present in
502 CSs as exemplified by BO-type CS WF1202B-0013, for this reason this particle is not included in
503 the BO-type average in Fig. 10A. The depletion in volatile Rb, Na, Cu, Zn, and Pb may not be
504 linked directly to element condensation temperatures, as Pb is present at higher concentrations
505 than all other volatile elements. Alternatively, the relative Pb enrichment may be due to
506 contamination during LA-ICP-MS analysis.

507 The CAT-like CSs are distinct from the normal group by a higher enrichment in refractory
508 elements (~ 2.1 to $4.9 \times \text{CI}$), with a mean REE_N equal to 4.1 ± 1.5 times CI (1 SD; $n = 6$; Fig. 10),
509 and a stronger mean depletion in siderophile elements W, Co and Ni (by ~ 1 to 4 orders of
510 magnitude). Chalcophile Cr, V, and Mn are depleted to 0.2-0.02 times CI on average (Fig. 10). On
511 average, CAT-like CSs exhibit a negative U anomaly comparable to that of the normal chondritic
512 CS group, although individual spherules can be U-enriched, as seen for BO-type CS WF1202B-
513 0016 (Supplementary Table S1). The depletion in volatile Rb, Na, Cu, Zn, and Pb is not as

514 pronounced as for the normal chondritic CSs, mostly as the result of V-type CS WF1202B-0029
515 that shows a less volatile element-depleted signature.

516 The high Ca-Al spherules show the highest enrichment in refractory elements of all groups
517 (~ 2.4 to $5.2 \times \text{CI}$), with a mean REE_N equal to 4.5 ± 1.6 times CI (1 SD; $n = 3$; Fig. 10). This mean
518 value excludes V-type CS WF1202B-0001 characterized by an even higher REE enrichment factor
519 of ~ 24 relative to CI chondrites (Supplementary Table S1). All high Ca-Al spherules exhibit a
520 negative U anomaly, although limited in WF1202B-0001. The relative depletions in siderophile
521 W, Co, and Ni and chalcophile Cr, V, and Mn for the average high Ca-Al group are intermediate
522 between those of the normal and CAT-like groups (Table 1; Fig. 10). The depletion in volatile Rb,
523 Na, Cu, Zn, and Pb is similar to or larger than that observed for the normal CSs.

524

525 **3.5. Oxygen isotope ratios**

526 The $\delta^{18}\text{O}$, $\delta^{17}\text{O}$ and $\Delta^{17}\text{O}$ values for 28 CSs are reported in Table 2. These CSs, with diameters
527 ranging from 325 to 715 μm and masses between 45 and 450 μg (see Section 2.5; Supplementary
528 Fig. S5), were randomly selected from the Widerøefjellet collection and analyzed for their three-
529 oxygen isotopic compositions. Based on BSE images of whole particles, these CSs have been
530 assigned to the BO-type ($n = 7$, $\sim 25\%$), Po-type ($n = 2$, $\sim 7\%$), V-type ($n = 10$, $\sim 36\%$), and CC-
531 type ($n = 6$, $\sim 21\%$) textural groups (Genge et al., 2008; Table 2). One CS has an irregular
532 appearance, while 2 other particles represent BO/CC-type mixtures (Fig. 3; Table 2). This
533 distribution by types is similar to that of unbiased collections (e.g., Taylor et al., 2000; Cordier and
534 Folco, 2014), and consistent with the 49 Widerøefjellet CSs characterized for major and trace
535 element concentrations (Supplementary Table S1). In Figure 12, the $\Delta^{17}\text{O}$ data versus $\delta^{18}\text{O}$ of the
536 CSs are shown relative to the TFL and the oxygen isotopic compositions of various chondrite
537 groups (Clayton et al., 1991; Clayton and Mayeda, 1999; Newton et al., 2000). Figure 12A
538 compares the data from this work to high-precision oxygen isotopic data determined for Antarctic
539 CSs by IRMS available from literature (Cordier et al., 2011a, 2012; Suavet et al., 2010, 2011a),
540 while Fig. 12B links the acquired data to the values determined for eighteen $> 500 \mu\text{m}$ diameter
541 CSs from the Atacama Desert in Chile (van Ginneken et al., 2017) and includes textural
542 information.

543 The oxygen isotopic compositions of the CSs characterized here can be compared to the four
544 groups previously defined qualitatively by Suavet et al. (2010) (Fig. 12A). A fifth group is often

545 added to these four to accommodate for HED-like materials (e.g., Cordier and Folco, 2014 and
546 references therein). Below the TFL, 3 of 10 V-type, 5 of 7 BO-type, 1 of 2 Po-type, 4 of 6 CC-
547 type CSs, and 1 mixed BO/CC-type CS exhibit isotopic compositions that fall within or close to
548 the *Group 1* field, defined to exhibit $\Delta^{17}\text{O}$ values below -2.2‰ and $\delta^{18}\text{O}$ values of 8 to 32‰ (Suavet
549 et al., 2010). A single V-type CS WF 1202B-0057 has an isotopic composition that can be
550 considered to be part of *Group 2*, previously constrained to range from -0.2 to -1.5‰ for $\Delta^{17}\text{O}$
551 with $\delta^{18}\text{O}$ of $\sim 25\text{‰}$ (Suavet et al., 2010). One V-type (WF1202B-0105) and 2 CC-type CSs
552 (WF1202B-0061 and 0069) fall in between *Group 1* and *Group 2* and cluster closer to meteoritic
553 values, with $\Delta^{17}\text{O}$ between -2.0 and -1.6‰ and $\delta^{18}\text{O}$ around 12‰ . Mixed BO/CC-type CS
554 WF1202B-0071 with a $\Delta^{17}\text{O}$ of -0.25 and $\delta^{18}\text{O}$ of 37.2‰ remains ambiguous and cannot be
555 assigned to either *Group 1* or *Group 2*, or any particular chondrite group. Above the TFL, five V-
556 type, 1 BO-type, 1 CC-type CS, as well as 1 CS with an irregular texture have isotopic
557 compositions that fall within or close to the *Group 3* field, defined to display $\Delta^{17}\text{O}$ values between
558 0.1 and 1.0‰ and $\delta^{18}\text{O}$ values of $\sim 15\text{‰}$; Suavet et al., 2010). One CS of each main textural group
559 (V-, BO-, CC-, and Po-type) is characterized by an isotopic composition close to that of the ^{16}O -
560 poor *Group 4*, with $\Delta^{17}\text{O}$ of $\sim 2\text{‰}$ and $\delta^{18}\text{O}$ equal or larger than 40‰ (Suavet et al., 2010).
561

562 **4. DISCUSSION**

563 **4.1. Accumulation mechanism for Widerøefjellet**

564 Natural concentration and alteration processes (e.g., wind sorting, interaction with fluids) and
565 sampling methods (e.g., sieving, magnetic separation, hand-picking) may introduce biases in the
566 physicochemical properties of a MM collection. The Concordia collection, recovered by melting
567 large volumes of Antarctic snow, is considered one of the least biased collections based on the
568 high abundance of fragile fine-grained fluffy and ultracarbonaceous particles as well as the
569 occurrence of sulfides prone to weathering (e.g., Nakamura et al., 1999; Duprat et al., 2007, 2010;
570 Dobrica et al., 2012; Genge et al., 2018). However, CSs are not described for this collection
571 (Dobrica et al., 2010), preventing a direct comparison with collections recovered from deposits
572 with longer accumulation ranges, such as blue ice-derived collections and sedimentary
573 accumulations. As an example, fine- and coarse-grained unmelted particles are significantly less
574 abundant in the SPWW (Taylor et al., 1998, 2000, 2007b), Cap Prud'homme (Kurat et al., 1994;
575 Genge et al., 1997), Larkman Nunatak (Genge et al., 2018), or TAM (Rochette et al., 2008)
576 collections relative to the Concordia collection (Dobrica et al., 2010), indicating terrestrial
577 reprocessing or collection and operator biases.

578 Despite different particle size distributions for various collections, the abundance of CS types
579 may also provide some insight regarding potential collection biases. For example, magnetite and
580 wüstite-dominated I-type CSs, relatively resistant to weathering, represent 1% of all CSs larger
581 than 100 μm in the SPWW collection, generally considered a relatively unbiased MM collection
582 (Table 3; Taylor et al., 2000, 2007a; Rochette et al., 2008; Genge et al., 2018). Slightly higher
583 abundances of I-type particles (3-4% of all CSs >200 μm) have been observed in the TAM
584 collection, while even higher values in the Larkman (6% of all CSs >60 μm), Walcott N  v   (6%
585 of all CSs >100 μm), and Indian Ocean (6% of all CSs >60 μm) collections likely indicate higher
586 weathering degrees, taking into account the respective collection size ranges (Table 3). Mid-
587 Pacific abyssal clays up to 500 kyr old form an extreme example, with I-type particles constituting
588 25 to 50% of the extracted CSs, based on 700 particles of 0.1 to 1 mm where the variation depends
589 on the core samples and magnetic extraction procedures employed (Blanchard et al., 1980). If no
590 metal-bearing I-type spherules were lost, the comparable degree of I-type enrichment in the
591 Wider  fjellet and TAM collections relative to the SPWW collection may indicate a significant

592 loss of S-type particles due to weathering or wind transport, although potential biases linked to
593 particle size distributions remain difficult to evaluate.

594 Particle losses may be detected by studying the cumulative size distribution of the
595 Widerøefjellet collection relative to those of other collections (Fig. 4A). To account for the
596 diversity of procedures that exist to construct cumulative size distributions (e.g., Taylor et al.,
597 2000, 2007b; Suavet et al., 2009; Genge et al., 2018), the cumulative size distribution for CSs from
598 Widerøefjellet (>200 μm size fraction) was compared to the data provided for a set of CSs from
599 the TAM (>400 μm size fraction; Suavet et al., 2009). The diameters were first collected in 20 μm
600 bins, after which power law functions were fitted to the diameters larger than 240 μm and 440 μm ,
601 respectively, to account for potential sieving biases, using the OriginPro software. As the studied
602 size fractions were picked in their entirety, no mathematical corrections were applied. The
603 calculated slope exponent of the TAM cumulative size distribution equals to -4.8 ± 0.2 for the
604 particles larger than 440 μm , in good agreement with values of -4.8 and -5 determined for the non-
605 magnetic and magnetic fractions of the TAM collection (Suavet et al., 2009). The slope exponent of
606 the Widerøefjellet cumulative size distribution equals to -4.4 ± 0.2 (for particles >240 μm), which
607 overlaps within uncertainty with the exponent obtained for the TAM collection (Fig. 4A). These
608 values are close to the -5.0 and -5.4 slopes determined for the SPWW collection (Taylor et al.,
609 2000, 2007b), but may still indicate minor weathering or transport losses for the Widerøefjellet
610 collection. The Walcott Névé collection represents a more extreme case, where a strong deficit in
611 smaller particles not accounted for by a sieving bias (~6% of all CSs >100 μm is I-type; Table 3)
612 with a large fraction of the MMs exhibiting moderate to severe alteration led to a slope exponent
613 of -2.9 determined for the 200-400 μm size fraction (Suavet et al., 2009). Similarly, the Larkman
614 nunatak collection (~6% of all CSs >60 μm is I-type) exhibits a power law distribution with an
615 exponent of -5.3 only for diameters from 210 to 330 μm , with abundances decreasing below the
616 power law at both higher and lower diameters (Genge et al., 2018).

617 Taking into account subtle differences in the classification scheme used for S-type CSs, the
618 relative abundances of Po-, BO-, CC-, and V-type CSs are fairly comparable for the older Larkman
619 nunatak, Cap Prud'homme, and TAM collections on one hand and for the younger Indian Ocean
620 and SPWW collection on the other (Genge et al., 2018). The diversity in quench textures among
621 melted silicate particles has previously been attributed to (i) different peak temperatures and

622 cooling rates experienced during atmospheric entry, with peak temperatures increasing from Po-,
623 over BO- and CC-, to V-type CSs (e.g., Taylor et al., 2000), as supported by the μ CT data in this
624 work (Section 3.2), and (ii) the grain size of the precursor material, as coarser-grained
625 micrometeoroids have higher probabilities to evolve into relict-bearing spherules (e.g., Taylor et
626 al., 2012; van Ginneken et al., 2017). Here, it should be noted that the distinction between BO-
627 and CC-type CSs may be biased by the operator, with the existence of a continuum in particle
628 textures and the occurrence of CSs exhibiting dual textures, including mixed BO/CC-type CSs.
629 Based on the comparable abundance of V-type CSs for all collections (except Widerøefjellet),
630 which requires limited subjectivity in classification, such differences have been interpreted to
631 reflect systematic changes in the velocities of the dust particles arriving to Earth (Genge et al.,
632 2018). When comparing the frequency of the different CS types (Table 3), the Widerøefjellet
633 collection is characterized by a significantly higher contribution of V-type CSs for different size
634 fractions above 200 μ m. Glass spherules are generally more prone to fracturing and chemical
635 alteration, mostly due to secondary wind transport and/or strong interaction with ice or fluids over
636 time. This is demonstrated by the heavily altered Walcott Névé and Larkman nunatak collections,
637 where CSs frequently contain surface and penetrative fractures as the result of impact after wind
638 transportation and swelling or cryoclasty (freeze-thaw weathering), respectively (Suavet et al.,
639 2009; van Ginneken et al., 2016; Genge et al., 2018). Although these sites have been accumulating
640 material for at least one Myr, the main factor controlling weathering may be the temperature
641 variation of the local environment, such as seasonal melting of the thin layer of snow covering the
642 MM accumulation sites. The effects of chemical weathering include the removal of primary
643 mineral phases, such as olivine and glass, and incrustations by weathering products (van Ginneken
644 et al., 2016). Ferrihydrite and jarosite have been shown to precipitate within cavities of TAM MMs,
645 resulting in pseudomorphic textures within heavily altered particles. Glass is known to alter into
646 palagonite gels with sequential replacement indicative of varying water-to-rock ratios. Metal may
647 be replaced by Fe-oxide/hydroxide (e.g., goethite, lepidocrocite, and maghemite), although
648 magnetite formed during atmospheric entry is generally resistant to alteration by interaction with
649 the terrestrial environment (van Ginneken et al., 2016).

650 Physical weathering is mainly due to frequent freeze-thaw cycles occurring due to daily change
651 in surface temperature within the MM traps. Such weathering results in the fracturing of a fraction
652 of the MMs (Rochette et al., 2008; Suavet et al., 2009). In the Widerøefjellet collection, the effects

653 of both chemical and physical weathering of CSs appear limited and similar to what is observed
654 for MMs from the TAM (Tables 1 and 2; Supplementary Table S1), although jarosite weathering
655 products are not abundant (van Ginneken et al., 2016). This is consistent with the assumption of
656 limited variation in the environment over the period of accumulation of the CSs and insubstantial
657 interaction with ice melts. Following the weathering scale for MMs of van Ginneken et al. (2016),
658 based on both the degree of terrestrial alteration and the level of encrustation by secondary phases,
659 the Widerøefjellet particles studied can be assigned to the 0a to 2c scales, indicating no visible to
660 moderate loss and/or alteration of primary material with no visible to complete encrustation (Fig.
661 3). The limited degree of chemical alteration observed for Widerøefjellet particles may be linked
662 to the high altitude, the presence of a permanent snow layer, or the observation that the CS-rich
663 sediment was sampled in a shadow-rich zone during the peak of the austral Summer.

664 The bulk geochemical composition of different CS collections can to a certain degree also be
665 used to evaluate possible biases through comparison of the molar $\text{Fe}/(\text{Mg} + \text{Si})$ ratios of the CSs
666 studied (Fig. 6). Magnetic separation will favor the extraction of magnetite-bearing CSs (e.g., G-
667 and I-type spherules), while non-magnetic V-types will be underrepresented. Hence, CSs with
668 molar $\text{Fe}/(\text{Mg} + \text{Si})$ above 0.1 ratios will be overrepresented when applying magnetic separation,
669 as observed for the Frontier Mountain and Walcott Névé collections (Suavet et al., 2009). The
670 molar $\text{Fe}/(\text{Mg} + \text{Si})$ distribution for a Miller Butte subsample that did not undergo magnetic
671 separation is more similar to that of the SPWW collection (Fig. 6). During the sample preparation
672 of the Widerøefjellet collection, no magnetic or density separation was performed, and the molar
673 $\text{Fe}/(\text{Mg} + \text{Si})$ ratio distribution is comparable to that of the SPWW (Taylor et al., 2000). Compared
674 to the other collections shown, the Widerøefjellet and SPWW collections both have a significant
675 contribution of particles with molar $\text{Fe}/(\text{Mg} + \text{Si})$ below 0.1.

676 Combining the various physicochemical properties of the SRM collection (degree of alteration,
677 abundance by type, size-frequency distribution, $\text{Fe}/(\text{Mg} + \text{Si})$ ratio, etc.), the Widerøefjellet
678 collection may thus be largely unbiased for the size fractions studied (Table 1; Supplementary
679 Table S1). While the Widerøefjellet collection shares properties with both old and young
680 (Antarctic) MM collections in terms of CSs, the most obvious feature is the high abundance of V-
681 subtype CSs, consistent across different size fractions (Table 3). While secondary trapping and
682 transportation effects, for example due to lack of wind or the presence of a stabilizing fine-grained
683 dust below the snow layer (Genge et al., 2018), cannot be excluded, the high V-subtype abundance,

684 and overall distinct relative abundances of V-, BO-, CC-, and Po-type CSs, in the Widerøefjellet
685 collection could perhaps also be explained by systematic changes in the entry velocities of dust
686 caused by quasi-periodic gravitational perturbation during transport to Earth over the different time
687 periods of CS accumulation. This was first suggested by Genge et al. (2017) to explain the textural
688 differences between recent and older CS collections. Such changes may not be expressed in the
689 Larkman, Cap Prud'homme, TAM and Walcott Névé collections due to higher degrees of
690 weathering or the implementation of magnetic separation techniques.

691

692 **4.2. Parent body precursors of Widerøefjellet cosmic spherules**

693 *4.2.1. Constraints from elemental chemistry*

694 Based on the major element compositions, most, if not all, of the Widerøefjellet particles derive
695 from chondritic precursors. This interpretation is based on both major (Fig. 7, 8, 10) and trace (Fig.
696 9, 10) element compositions and trends, which all indicate compositional ranges close to or within
697 the chondritic fields. This chondritic parentage indicates that the majority of the dust delivered to
698 the Earth samples specific source regions (Section 4.4) and arrives through particular
699 transportation mechanisms (Poynting-Robertson drag for μm to cm particles; Rubin, 2018). The
700 achondritic particles described in literature are thus relatively rare (e.g., Folco and Cordier, 2015).
701 While largely chondritic (e.g., Brownlee et al., 1997), the chemical groups of CSs reflect the degree
702 of heating experienced and the degree of evaporation undergone during atmospheric entry.
703 Decreasing Si/Al and Mg/Al ratios are generally thought to reflect higher degrees of evaporation
704 (e.g., Alexander et al., 2002; Wang et al., 2001) and CSs evolve from the normal group (Si/Al =
705 14.6 and Mg/Al = 14.2), through the CAT-like group (Si/Al = 9.8 and Mg/Al = 9.9), to the high
706 Ca–Al group (Si/Al = 6.6 and Mg/Al = 8.0), with variable Fe/Si, Mg/Si, and CaO and Al_2O_3
707 contents as a result (Taylor et al., 2005; Cordier et al., 2011b; Fig. 8).

708 The bulk spherule composition is also controlled by the mineralogy of the precursor material
709 (e.g., Imae et al., 2013). This is clear from major element trends, but also from the trace element
710 plots, where the occurrence of specific REE patterns highlights the influence of mineral precursors,
711 such as enstatite and forsterite (Fig. 8D, 9), but possibly also Cr-rich spinel crystals (e.g.,
712 WF1202B-0013 and 0041 with $> 1 \text{ wt}\%$ Cr_2O_3). As atmospheric melting and concomitant
713 evaporation experienced by CSs strongly affected primary textures, mineralogy and chemical
714 compositions, precisely constraining the nature of the chondritic sources remains highly

715 challenging (e.g., Alexander et al., 2002; Taylor et al., 2005). Most elemental concentrations and
716 ratios are either not sufficiently discriminative or underwent too large a modification to deduce the
717 type of precursor body (e.g., Rudraswami et al., 2016).

718

719 4.2.2. Constraints from oxygen isotope ratios

720 Triple-oxygen isotope ratios have been shown to be a powerful tracer of the origin of CSs and
721 MMs in general (e.g., Engrand et al., 1999; Yada et al., 2005; Taylor et al., 2005; Suavet et al.,
722 2010; Cordier and Folco, 2014). Based on their distribution in three-O isotopic space, bulk CSs
723 have previously been assigned to five large isotopic groups depending on the identification scheme
724 used (Fig. 12; Section 3.5). These assignments take into account mixing with atmospheric oxygen
725 (constant at $\delta^{18}\text{O} \approx 23.5\text{‰}$ and $\delta^{17}\text{O} \approx 11.8\text{‰}$ up to 60.9 km altitude; Thiemens et al., 1995) and
726 mass-dependent fractionation during atmospheric entry. Loss of material by evaporation (Engrand
727 et al., 2005) and separation of iron-nickel droplets (Brownlee et al., 1984; Genge and Grady, 1998)
728 may lead to mass-dependent oxygen isotope fractionation with higher $\delta^{17}\text{O}$ and $\delta^{18}\text{O}$ values (Suavet
729 et al., 2010; Fig. 12). Here, the data collected indicate the existence of a third process affecting the
730 bulk oxygen isotopic compositions of Antarctic CSs, involving the interaction with Antarctic
731 precipitation (Fig. 12). While surface snow samples in Antarctica have revealed highly variable O
732 isotopic compositions, the nearby Nansen blue icefield indicates $\delta^{18}\text{O}$ values of $-43 \pm 3\text{‰}$ (1 SD;
733 $n = 185$; Zekollari et al., 2019). Although alteration products of Antarctic CSs vary widely
734 depending on the sample location, exposure age, and textural type of the particles, these will be
735 dominated by Fe-oxyhydroxides, clay minerals, or palagonite (van Ginneken et al., 2016).
736 Alteration products in equilibrium with meteoric waters at 0°C will be offset from the surrounding
737 ice by $\delta^{18}\text{O}$ values varying between 0 and 20‰ depending on the minerals concerned (Beaudoin
738 and Therrien, 2009; Alexander et al., 2018), with a secondary mineral assemblage to the right of
739 the surrounding meteoric water along the TFL, with an average $\delta^{18}\text{O}$ of roughly -30‰ . As a result,
740 the bulk composition of the affected CSs will have moved in this general direction (see dashed
741 arrows for *Group 1* extremes on Fig. 12A). This effect is likely important in other collections and
742 previously reported O isotope data as well but remains difficult to evaluate due to varying
743 preparation and measurement protocols (e.g., washing with acetone versus acid leaching).

744 Chondritic spherules that plot well below the TFL are commonly assigned to bulk carbonaceous
745 chondrites CV, CO, CM, CR, or their constituent chondrules and refractory inclusions (e.g., Ca-

746 Al-rich inclusions, CAIs). As the isotopic compositions for Wild 2 anhydrous mineral grains
747 partially overlap with the fields defined for both carbonaceous and ordinary chondrites (with $\Delta^{17}\text{O}$
748 between -21.4 and $+3.4\text{‰}$ and $\delta^{18}\text{O}$ between -47.2 and $+3.5\text{‰}$, with 2σ analytical uncertainties
749 ranging from 1 to 4‰ for $\delta^{18}\text{O}$; Nakamura et al., 2008), cometary particles cannot be discriminated
750 from asteroidal material. Suavet et al. (2010) discriminated *Group 1* from *Group 2* carbonaceous
751 CSs based on their isotopic signatures (Fig. 12). In this classification scheme, *Group 1* CSs have
752 $\Delta^{17}\text{O} \approx -3$ to -5‰ , and $\delta^{18}\text{O}$ in the range of 10 - 30‰ , while *Group 2* CSs have $\Delta^{17}\text{O} \approx -1\text{‰}$, and
753 $\delta^{18}\text{O}$ between 15 - 35‰ . For the Widerøefjellet dataset, only a single CS falls close to the *Group 2*
754 (V-type WF1202B-0057; Table 2; Fig. 12). Fourteen of 16 Widerøefjellet spherules below the
755 TFL plot significantly lower than *Group 2*, extending the ranges of the previously identified *Group*
756 *1*, and likely indicate the existence of a continuum between particles deriving from CV, CO, CM
757 and possibly CR carbonaceous chondrites (Fig. 12). Based on mixing lines starting from the
758 chondrite fields, CC-type CS WF1202B-0078 is likely connected to CV carbonaceous chondrites
759 or derives from chondritic refractory inclusions, while V-type WF1202B-0053, BO-type
760 WF1202B-0058, 0064, 0077, and mixed BO/CC-type WF1202B-0080 can conclusively not have
761 a CR chondritic parentage, and share a CV, CO, or CM-related origin (Fig. 12; Table 2).

762 *Group 2* particles, in part linked to CR carbonaceous chondrites, thus constitute only 4% of the
763 Widerøefjellet collection relative to 21% and 17% of similar particles in the TAM and Atacama
764 Desert collections (Suavet et al., 2010; van Ginneken et al., 2017). The cosmic-ray exposure ages
765 for Atacama Desert and TAM surfaces indicate collection windows between the present and 4 to
766 5 Myr ago (Suavet et al., 2010; van Ginneken et al., 2017). The measured terrestrial ages of
767 individual TAM particles, based on their thermal remanent magnetization, indicate that most
768 particles ($\sim 66\%$) fell to Earth between 1-2 Myr ago, while the remainder ($\sim 33\%$) fell more recently
769 (Suavet et al., 2011b). Thus, in practice, the TAM collection has an accumulation window of up
770 to 2 Ma and is possibly biased toward the latter half of this window. This seems comparable to the
771 collection age for Widerøefjellet, where the deglaciation history of the SRM indicates possible
772 accumulation during the last ~ 1 -3 Ma. This implies that the relative contributions of the O isotopic
773 groups to these collections are not linked to accumulation windows alone, and the observed
774 underrepresentation of *Group 2* particles at Widerøefjellet (Table 2; Fig. 12) may rather reflect the
775 preservation state of the Widerøefjellet collection or the preparation procedures applied before
776 analysis. However, if *Group 2* particles formed from CR chondritic precursors and *Group 1*

777 spherules are dominated by CM-CO-CV carbonaceous chondrites, with the latter much more
778 common than the CRs in the relatively recent meteorite record (< 3 Ma) (Meteoritical Bulletin
779 Database: <http://www.lpi.usra.edu/meteor/metbull.php>, accessed 17 October 2019), detailed
780 comparison between collections with distinct accumulation windows (e.g., CSs from rooftops;
781 Genge et al., 2017) and analysis of more representative numbers of CSs may reveal changes in the
782 MM source regions.

783 Particle WF1202B-0071 with a mixed BO-/CC-type texture (Fig. 3) plots slightly below the
784 TFL and to the right of the *Group 2* field ($\Delta^{17}\text{O} \approx -0.25\text{‰}$, $\delta^{18}\text{O}$ of 37.18‰). Based on its triple-
785 oxygen isotopic composition, WF1202B-0071 may have derived from HED asteroids, or the CI-
786 type or enstatite chondrite parent bodies (Fig. 12). When considering the major element ratios
787 (including Mg/Al, Si/Al, and Fe/Mg) determined using semi-quantitative SEM-EDS before IRMS
788 (Supplementary Fig. S3), this particle likely does not originate from a differentiated parent body
789 and its origin remains ambiguous, as the field for enstatite chondrites overlaps with that of CI
790 chondrites. However, a large degree of mass-dependent isotope fractionation (>30‰) would be
791 required to explain the observed $\delta^{18}\text{O}$ from an enstatite chondritic starting composition. Particle
792 WF1202B-0071 could thus potentially originate from a CI chondrite precursor. Based on textural
793 and geochemical observations on unmelted particles, MMs deriving from CI chondrites are known
794 to exist (Kurat et al., 1992; van Ginneken et al., 2012), yet no particles have previously been
795 assigned to CI precursors based on O-isotope data. Such particles are likely more abundant in the
796 smallest size fractions.

797 Above the TFL, two fairly well-defined groups have been identified that are confirmed by the
798 particles characterized in this work. *Group 3* CSs are mostly related to ordinary chondrites,
799 although contributions from enstatite, R and CI chondrites cannot be excluded (Fig. 12). *Group 4*
800 spherules are characterized by significantly elevated $\delta^{17}\text{O}$ and $\delta^{18}\text{O}$ (above stratospheric oxygen)
801 and $\Delta^{17}\text{O}$ above 1.0‰ (Fig. 12), which have been described as ^{16}O -poor spherules in literature
802 (Yada et al., 2005; Suavet et al., 2010, 2011). To date, the nature of these spherules remains unclear
803 but a derivation from a known ordinary chondritic progenitor appears improbable, as the amount
804 of evaporation required to shift ordinary chondritic compositions towards such high $\delta^{17}\text{O}$ and $\delta^{18}\text{O}$
805 does not agree with their measured bulk major element compositions (e.g., Yada et al., 2005;
806 Cordier and Folco, 2014; Supplementary Fig. S3). Instead, fragments of unequilibrated ordinary
807 chondrites, dominated by secondary magnetite grains ($\Delta^{17}\text{O} = +5$ to $+7\text{‰}$; Choi et al., 1998) or

808 chondrules with glass or feldspathic mesostasis ($\Delta^{17}\text{O} = +3\text{‰}$; Franchi et al., 2001) have been
809 suggested. As all textural subtypes of S-type CSs are represented among the *Group 4* particles
810 studied in this work (V-, CC-, BO-, and Po-type), the latter ideas are no longer considered
811 reasonable, as this would require a magnetite or feldspathic component to be the main contributor
812 to the oxygen isotopic compositions of *Group 4* CSs, which is not tenable considering the modal
813 mineralogy of the particles studied here. Alternatively, these MMs may represent ^{16}O -poor nebular
814 material from a reservoir that currently remains unsampled by normal-sized meteorites (Yada et
815 al., 2005; Suavet et al., 2010). Based on the observed mass-dependent isotope fractionation effects
816 and exchange with atmospheric oxygen for *Group 1* and *Group 3* particles, the probable starting
817 composition of *Group 4* spherules was around $\delta^{18}\text{O} \approx +20\text{‰}$ and $\Delta^{17}\text{O} \approx +3\text{‰}$, which, albeit large
818 analytical uncertainties, is within range of the bulk O-isotopic measurements reported for
819 particular interplanetary dust particles (IDPs; Starkey et al., 2014).

820 While metal bead segregation is assumed to induce mass-dependent oxygen isotope
821 fractionation (Genge and Grady, 1998; Suavet et al., 2010), no direct relationship between the
822 presence of high-density phases or high $\delta^{18}\text{O}$ is observed for the Widerøefjellet particles, although
823 the nature of the high-density phases (metal bead, sulfide, spinel group mineral, etc.) mostly
824 remains ambiguous (Table 2). This indicates that mass-dependent isotope fractionation may be
825 caused by a variety of processes, including evaporation, high-density phase segregation or kinetic
826 isotope effects during interaction with atmospheric oxygen (Taylor et al., 2005). Similarly, the
827 presence of vesicles does not seem to influence the degree of mass-dependent fractionation
828 experienced (Table 2). While also no correlation is observed between the meteorite type from
829 which the CSs are derived based on oxygen isotope ratios and their chemical group (Cordier et al.,
830 2011b), general trends between the oxygen isotopic composition and textural groups of CSs have
831 previously been observed (van Ginneken et al., 2017) and are discussed in Section 4.4.

832

833 **4.3. Chemical modification during atmospheric heating**

834 In the following paragraphs, we argue that the observed deviations from chondritic values in
835 bulk chemistry (Fig. 8-11) largely stem from effects linked to evaporation, high-density phase
836 segregation, and redox shifts taking place during atmospheric passage on mostly originally
837 chondritic particles or (refractory) mineral components, rather than from chemical alteration taking
838 place during the terrestrial residence of the studied particles, supporting the pristine nature and

839 representativeness of the Widerøefjellet CS collection. Here, the fragmentation dynamics in
840 specific Solar System source regions, resulting in unrepresentative subsampling of the parent
841 bodies involved, most likely play an important role in determining the bulk composition of CSs.

842 To study the individual effects of the processes mentioned above, the data for all CS analyzed
843 here are compiled for all textural (V-, BO-, and CC-type) and chemical (normal, CAT-like, high
844 Ca-Al) groups, to minimize the effects related to heterogeneity in precursor mineralogy and
845 individual CS chemistry (Table 1; Fig. 10). To obtain an average chemical composition for the
846 normal BO-type CSs, the composition of WF1202B-0013 was excluded, as this normal CS (Fe/Si
847 of 1.09 and Mg/Si of 0.93) is characterized by a high enrichment in REE (average REE_N of 7.03)
848 with a fractionated LREE-enriched pattern ((La/Yb)_N of 3.83), exhibiting negative Ce and Eu
849 anomalies (Supplementary Table S1). Similarly, the composition of WF1202B-0001 was excluded
850 from the high Ca-Al CSs because of its extreme enrichment in REE (more than 10 times CI) and
851 fractionated REE pattern ((La/Yb)_N of 2.60; Fig. 8, 9; Table 1). Overall, the average REE patterns
852 for the 3 texturally (V-, BO-, and CC-type) and chemically (normal, CAT-like, and high Ca-Al)
853 characterized CS types are consistent with bulk chondrite compositions and exhibit relatively flat
854 REE patterns (La/Yb_N = 0.91-1.01; Table 1; Fig. 8, 9, 10; Supplementary Table S1): 33 out of 34
855 normal, 6 out of 6 CAT-like, and 3 out of 4 high Ca-Al CSs have relatively chondritic REE patterns
856 (Fig. 9), consistent with literature data (e.g., Folco and Cordier, 2015). With the exception of the
857 LREE-enriched REE patterns recognized in the current work (Fig. 9F), all REE patterns have
858 previously been observed among the 76 V-type spherules of Cordier et al. (2011b). Conversely,
859 U-shaped REE patterns (La/Yb_N = 0.8-2.2; Eu* = 3.8-10.6), the least abundant signature among
860 the V-type spherules of Cordier et al. (2011b), are not observed among the CSs studied here,
861 although perhaps the case could be made that the LREE-enriched patterns observed for WF1202B-
862 0001, 0013, and 0042 (Fig. 9F) partly resemble the U-shaped REE patterns described. A positive
863 Ce anomaly, a feature typical of U-shaped REE patterns (Cordier et al., 2011b), has only been
864 observed in a single V-type spherule (WF1202B-0017) that could also be interpreted to represent
865 a member of the U-shaped group. Likely, a continuum exists between these subtypes, reflecting
866 competing processes linked to the thermal and redox processes taking place during atmospheric
867 passage.

868

869 *4.3.1. Evaporation*

870 The observed diversity in quench textures and chemical compositions in CSs has previously
871 been interpreted to result from variable peak temperatures and evaporative loss during atmospheric
872 entry and heating (e.g., Taylor et al., 2000; Genge et al., 2008). From Po-type to BO- and CC-type,
873 V-type spherules and then the more strongly evaporated CAT and high Ca-Al spherules, peak
874 temperatures are thought to increase, leading to increases in CaO, Al₂O₃, TiO₂, and MgO contents,
875 as well as decreases in FeO contents relative to chondritic values (Taylor et al., 2000; Cordier et
876 al., 2011b; Section 3.3). These chemical trends are consistent with both geochemical models
877 (Alexander et al. 2002) and experimental simulations (Floss et al., 1996; Wang et al., 2001) of
878 heating and evaporation starting from chondritic and solar starting compositions (Fig. 11).

879 By comparing the refractory major element and REE compositions of the CSs with those of the
880 residues obtained after heating of experimental charges with solar composition (Wang et al., 2001),
881 Cordier et al. (2011b) estimated that CSs of the normal group experienced between 40% and 50%
882 mass loss, CAT-like CSs between 50% and 60% mass loss, and high Ca–Al spherules between
883 80% and 90% mass loss. These calculated values based on the elemental compositions are similar
884 to those estimated for CAT-like spherules based on isotopic values (~50% mass loss; Alexander
885 et al., 2002) and fit with the mass losses of 70-90% proposed by Love and Brownlee (1991), at
886 least for the high Ca-Al CSs. However, these values need to be considered upper estimates for the
887 mean values, as individual particles can show even larger variations in the degree of evaporation
888 (Fig. 11). According to Taylor et al. (2005), evaporative losses can also be approximated through
889 trends on a plot of the atomic Si/Al versus atomic Mg/Al ratio (Fig. 8D), provided that the bulk
890 composition of the MM precursor can be estimated adequately. Aluminum, with a 50%
891 condensation temperature T_C of 1653K, is progressively enriched relative to Mg and Si (50% T_C
892 of 1336K and 1310K, respectively; Lodders, 2003). Extraterrestrial particles that are progressively
893 evaporated will therefore follow an evaporation trajectory starting from the carbonaceous and
894 ordinary chondrite source fields. In Fig. 8D, the majority of normal CSs lie within or near the
895 chondrite fields, attesting to minor to moderate degrees of evaporation. The CAT-like and high
896 Ca-Al spherules are positioned further down the evaporation trajectory, which reflects more
897 extreme atmospheric heating conditions. Particle WF1202B-0001 lies at the extreme end of the
898 evaporation curve, with evaporative loss estimates exceeding 90%.

899 The degree of evaporative loss in CSs during atmospheric entry can also be estimated from
900 refractory trace elements other than the REE (e.g., Sc, Y, Zr, and Hf; Fig. 8C). Refractory trace

901 element contents display a positive correlation with the degree of evaporation and consequently
902 the CaO and Al₂O₃ contents. While the majority of CSs from the 3 chemical groups fall within a
903 limited range (CaO+Al₂O₃ < 9 wt%, Sc+Y+Zr+Hf < 33 μg/g) and fairly close to the observed
904 correlation curve with a slope of ~0.27 (Fig. 8C), a number of CSs fall significantly outside this
905 range with strong deviations from the slope (e.g., WF1202B-0001, 0002, 0016, and 0011). The
906 majority of CSs belonging to the normal group are positioned at the lower end of the correlation
907 curve, reflecting minor evaporative losses. In contrast, the CAT-like and high Ca-Al CSs lie at the
908 middle and higher end of the correlation line, suggesting ~50% mass losses and >75% mass losses,
909 respectively. Particle WF1202B-0001 is an extreme case positioned at the far end of the correlation
910 line, again indicating strong evaporative loss (~90%). While this particle may have been affected
911 by some terrestrial alteration, the elements used in Fig. 8C are relatively immobile and should only
912 undergo limited effects from such process. As the slope of the correlation curve is defined by the
913 volatility of the combination of elements considered, CSs that deviate from this trend may reflect
914 highly variable precursor mineralogy and geochemistry (e.g., Imae et al., 2013).

915

916 *4.3.2. Depletion in siderophile and chalcophile elements*

917 Both siderophile (including W, Co, Ni) and chalcophile (including V, Cr, Mn) trace elements
918 show systematic negative anomalies relative to their neighboring lithophile elements when ordered
919 according to increasing volatility (Fig. 10). In the CSs studied in this work, the depletion in
920 siderophile elements is most pronounced for CAT-like CSs, while the high Ca-Al spherules exhibit
921 siderophile element depletions of similar magnitude as those observed for normal CSs. Among
922 normal CSs, the depletions are comparable for CC- and V-type spherules, while the effects are less
923 pronounced for BO-type spherules (Table 2; Fig. 10). The depletions relative to chondritic values
924 observed for chalcophile elements are comparable for CAT-like and high Ca-Al CSs, but less
925 pronounced in normal CSs.

926 Relative to experimentally defined evaporation trends, CAT-like spherules, presumably
927 affected by intermediate degrees of evaporative loss, display FeO concentrations significantly
928 lower than those measured for the high Ca-Al and normal groups (Fig. 10, 11D-F; Cordier et al.,
929 2011b). This confirms that Fe concentrations in CSs are not only governed by the evaporation
930 process. This is consistent with the Fe isotope fractionation observed in CSs, indicating that Fe is
931 mainly lost by physical separation of metal-rich phases, with minor free evaporation, except

932 perhaps in the case of CAT-like and high Ca-Al spherules (Alexander et al., 2002; Engrand et al.,
933 2005; Taylor et al., 2005).

934 The data reported here confirm the observations of Cordier et al. (2011b) who propose that
935 mechanical separation of siderophile- and chalcophile-rich phases occurs during atmospheric
936 entry, rather than partitioning of chalcophile elements into metal phases or loss by evaporation
937 alone (Brownlee et al., 1997; Genge and Grady, 1998). While removal of Fe–Ni metal or sulfide
938 beads from silicate melts has long been considered to cause depletions in siderophile and possibly
939 chalcophile elements (e.g., Brownlee et al., 1997; Genge and Grady, 1998), the separation of
940 chalcophile-rich solids, such as chromites, is a more recent idea (Cordier et al., 2011b). The latter
941 authors suggest that the migration of chromite grains toward the particle periphery may result from
942 differential acceleration between contained chromite grains and silicate melt, or as proposed for
943 metal beads in spinning CSs from centrifugal forces or floating of chromite grains on rising
944 vesicles, as surface tension allows for their fixation on the vesicle surface. However, the density
945 range for chromite between 4.5 and 5 g/cm³ perhaps renders the latter unlikely.

946 As chromite is a potential refractory phase in basaltic melts (e.g., Longhi and Pan, 1998; Roeder
947 and Reynolds, 1991), incomplete melting during atmospheric heating could lead to a depletion of
948 chalcophile elements in silicate melts. When chromite grains are small, their melting may take
949 place relatively fast, while the contrast in density relative to silicate melt may be less effective and
950 inhibit settling (Genge et al., 2016). However, if chalcophile and siderophile element depletions
951 result from (refractory) metal, sulfide or spinel group mineral losses, then the enrichment in
952 siderophile and to lesser extent chalcophile elements observed in high Ca-Al CSs would require
953 that these particles underwent less efficient separation of such high-density phases during
954 atmospheric passage, relative to the other chemical CS groups. As high Ca-Al spherules are
955 interpreted to have experienced the highest evaporative losses and peak temperatures, their
956 enrichment in siderophile and chalcophile elements relative to spherules that formed at lower
957 temperatures may simply result from the oversampling of more refractory phases within the MM,
958 i.e. a slight excess of spinel group minerals or refractory metal nuggets (e.g., as in the refractory
959 Ir and Pt-enriched high Ca-Al WF1202B-0011) rather than high-density phase ejection.

960

961 *4.3.3. Effects from redox conditions*

962 Following the work of Cordier et al. (2011b) on V-type spherules and extending these
963 observations to BO-type and CC-type CSs, the CS compositions determined here can be compared
964 to those of residues obtained after heating of experimental charges with solar composition in terms
965 of refractory major element and REE compositions (Fig. 11; Wang et al., 2001; Cordier et al.,
966 2011b). The progressive enrichment observed for refractory REEs from the normal group (avg.
967 $REE_N = 1.8 \times CI$) over the CAT-like group (avg. $REE_N = 4.1 \times CI$) to the high Ca–Al group (avg.
968 $REE_N = 4.5 \times CI$; Table 2) is consistent with increasing levels of evaporation. Evaporation mostly
969 does not fractionate the REEs, yet Ce does not always occur in chondritic proportions in CSs (Fig.
970 9, 11). While some of the observed Ce anomalies may be linked to terrestrial alteration (e.g.,
971 WF1202B-0013 and 0017), this is unlikely to be the case for all particles studied here, as most are
972 relatively fresh, devoid of fracturing and surficial alteration. In addition, the CSs showing Ce
973 depletions are not equally distributed among the different chemical groups studied, with 83% (by
974 number) of the CAT-like, 67% of the high Ca–Al, and only 15% of the normal chondritic CSs
975 exhibiting REE patterns characterized by a negative Ce anomaly (with $Ce^* < 0.88$; Fig. 9, 11).
976 While experimental residues systematically show large negative anomalies in Ce for mass losses
977 larger than 50% (Floss et al., 1996; Wang et al., 2001), Ce anomalies observed in CSs are generally
978 smaller in magnitude (1 to 2 versus 3 orders of magnitude in experiments; Fig. 11). As these Ce
979 anomalies are thought to result from the volatile behavior of Ce^{4+} under highly oxidizing conditions
980 prevalent during non-equilibrium kinetic evaporation in Earth’s atmosphere (Hashimoto, 1990;
981 Floss et al., 1996; Wang et al., 2001), Ce depletions in CSs hint at moderately oxidizing conditions
982 during atmospheric passage or incomplete vacuum during the experiments. As the Ce anomalies
983 are mainly observed in CAT-like and high Ca–Al spherules that are interpreted to have experienced
984 mass losses of 50% or higher, Ce anomalies in CSs may relate to high degrees of evaporation
985 experienced during atmospheric entry, which could allow for local increases in the partial pressure
986 of oxygen (Cordier et al., 2011b).

987

988 **4.4. Comparison to other Antarctic micrometeorite collections and implications for the** 989 **interplanetary dust complex**

990 While major and trace element concentrations indicate a largely chondritic parentage for the
991 CSs studied in this work, oxygen isotope ratios can refine the relative contributions of each
992 chondrite class. Cordier and Folco (2014) compiled previously reported three-oxygen isotope data

993 for 136 CSs. Of these 136 spherules, ranging from 50 μm to 2280 μm in diameter and studied
994 using both IRMS and ion microprobe, $\sim 60\%$ relate to carbonaceous chondrite asteroids (or
995 comets), $\sim 17\%$ to ordinary chondrites, $\sim 8\%$ to a ^{16}O -poor reservoir, and $\sim 4\%$ to HED asteroids,
996 while $\sim 11\%$ remain ambiguous. Importantly, the ratio of carbonaceous chondrite relative to
997 ordinary chondrite material decreases as the CS diameter increases, from ~ 10 for small particles
998 ($< 500 \mu\text{m}$) to ~ 0.3 for particles larger than $500 \mu\text{m}$. For CSs in the range of $500\text{-}1000 \mu\text{m}$ (32 in
999 the compiled dataset), $\sim 38\%$ can be linked to ordinary chondrites, while $\sim 38\%$ relates to
1000 carbonaceous chondrites, $\sim 6\%$ remains ambiguous and $\sim 19\%$ is related to HED asteroids (Table
1001 4). Note that the latter were the focus of the work by Cordier et al. (2011a) and the particles
1002 analyzed were selected based on their chemical composition, leading to a population bias. In the
1003 $250\text{-}500 \mu\text{m}$ size fraction, the number of CSs in the literature linked to ordinary chondrites
1004 decreases to $\sim 9\%$, while those related to carbonaceous chondrites increase to $\sim 80\%$, with ^{16}O -poor
1005 and ambiguous CSs both contributing $\sim 6\%$ of the population. Cosmic spherules below $500 \mu\text{m}$ are
1006 composed of $\sim 70\%$ carbonaceous chondrite-derived material (Cordier and Folco, 2014), consistent
1007 with the Mg-Si-Al compositions of various MM collections (Taylor et al., 2012; Genge, 2008).
1008 This distribution indicates that a significant proportion of large ($> 200 \mu\text{m}$) MMs are related to
1009 ordinary chondrites or to CO, CV, CK carbonaceous chondrites, whereas smaller MMs (from 20
1010 to $100 \mu\text{m}$) are mainly linked to CM2 or CR2 chondrites (Kurat et al., 1994; Brownlee et al., 1997;
1011 Engrand and Maurette, 1998; Engrand et al., 2005). This relationship may reflect the lower
1012 mechanical resistance of phyllosilicate-bearing chondrites, leading to enhanced fragmentation into
1013 smaller particles during dust production in space as a result of the collisions between their parent
1014 asteroids (Flynn et al., 2009). Examples of large anhydrous chondritic MMs include a $> 1000 \mu\text{m}$
1015 CV-like and a $> 700 \mu\text{m}$ CK-like MM (van Ginneken et al., 2012; Cordier et al., 2018). However,
1016 exceptions exist, as illustrated by unambiguously hydrated fine-grained chondritic CM/CR MMs
1017 recovered from the $> 400 \mu\text{m}$ size fraction (Suttle et al., 2019).

1018 For Widerøefjellet, a fairly similar particle parentage is observed for the $500\text{-}1000 \mu\text{m}$ size
1019 fraction, with $\sim 50\%$ of the spherules relating to carbonaceous chondrites, $\sim 29\%$ to ordinary
1020 chondrites, and $\sim 21\%$ to ^{16}O -poor material. Although the set of analyzed CSs remains limited, no
1021 clear population shift is observed for the $250\text{-}500 \mu\text{m}$ size fraction ($\sim 29\%$ OC, $\sim 57\%$ CC, $\sim 7\%$
1022 ^{16}O -poor, 7% ambiguous; Table 4). However, it should be noted that most of the CSs characterized

1023 in this size fraction fall between ~400 and 500 μm , so the expected transition in terms of relative
1024 abundance between the two CS size populations at around 500 μm (Cordier and Folco, 2014) might
1025 in fact lie between 250 and 400 μm . This agrees with impact destruction experiments on hydrous
1026 (e.g., CM chondrite) and anhydrous (e.g., ordinary chondrite) targets that show that small dust
1027 particles less than 300 μm are favored in hydrous (carbonaceous) targets (Flynn et al., 2009).

1028 In the compilation of Cordier and Folco (2014), no correlation was observed between CS texture
1029 and their assigned precursor material, except that most spherules related to HED asteroids
1030 primarily belong to the V-type subtype. Van Ginneken et al. (2017) recently studied a number of
1031 CSs recovered from the Atacama Desert and compared these to TAM CSs to determine possible
1032 relationships between the different textural CS types and their respective parent bodies. These
1033 authors concluded that coarse-grained dust particles, with affinities toward the ordinary chondrite
1034 parent bodies, are more prone to produce Po textures. At higher peak temperatures, these dust
1035 particles will preferably develop a CC-type texture, rather than a BO texture, due to the lack of
1036 nuclei available to develop new crystal faces. In contrast, BO spherules are predominantly thought
1037 to originate from the matrices of fine-grained carbonaceous chondrite particles (van Ginneken et
1038 al., 2017). This is mainly attributed to the mineralogical variety present in the matrices of
1039 carbonaceous chondrites, favoring supercooling, as well as the presence of accessory mineral
1040 phases, which may act as nuclei for the development of BO textures. No correlations have been
1041 found for V-type spherules as the highest peak temperatures ensure complete melting of the MM
1042 precursor, regardless of composition. Based on the triple-oxygen isotopic data of the
1043 Widerøefjellet collection (Table 2), the predominance of BO-type CSs toward a carbonaceous
1044 chondrite precursor (71% of BO-type), and the lack of correlation between V-type spherules and
1045 a specific precursor is confirmed. Yet, Po- and CC-type spherules do not follow the trends
1046 mentioned above. More specifically, one Po-type CS appears to be related to the *Group 4* CSs,
1047 while another is linked to carbonaceous chondrites (Tables 2 and 4). CC-type spherules at
1048 Widerøefjellet have a predominant affinity with carbonaceous chondrites (67%), as opposed to
1049 ordinary chondrites (17%). *Group 4* CSs are represented by all four major textural types. Hence,
1050 accurate predictions of the parent body composition of CSs solely based on textural properties
1051 remains challenging.

1052 The oxygen isotope composition of the SRM CS collection confirms that the composition of
1053 the micrometeoroid complex is different from that of macroscopic meteoroids. Materials with

1054 compositions similar to CI, CR, CM, CV, and CO chondrites dominate the former, whereas
1055 ordinary chondrites (~86%) and evolved meteorites (e.g., HED, making up ~4%) dominate the
1056 latter (Meteoritical Bulletin Database: <http://www.lpi.usra.edu/meteor/metbull.php>, accessed 17
1057 October 2019). Cosmic spherule statistics thus indicate that asteroids commonly observed in the
1058 inner asteroid belt (e.g., S-type ordinary chondrite and V-type HED parent asteroids) feed 20-30%
1059 or more of the micrometeoroid complex (Table 4). The other 55-60% is related to primitive solar
1060 system objects with carbonaceous chondritic compositions (Cordier and Folco, 2014). These
1061 materials could be associated to silicate dust released by short-period comets (e.g., Nesvorný et
1062 al., 2010) or with primitive asteroids belonging to the C-, D- or P-type spectral classes in the middle
1063 and outer asteroid belt (from 2.8 AU to Jupiter's orbit). In the case of the latter, recently disrupted
1064 asteroid families represent the primary source of MMs. Based on dynamic modeling and
1065 observations using the Infrared Astronomical Telescope (IRAS), three major dust bands produced
1066 by the C-type Veritas, older C-type Themis, and S(IV)-type Koronis asteroid families supply the
1067 majority of asteroidal dust delivered to the Earth (Kortenkamp, 1998; Nesvorný et al., 2002;
1068 Genge, 2008). Continued oxygen isotope ratio work on CSs, and MMs in general, extending the
1069 numbers of characterized particles as well as the currently sampled size fractions, will lead to a
1070 more refined understanding of the contributions of the various parent bodies in the solar system to
1071 the different fractions of the extraterrestrial flux to Earth and more accurately point out possible
1072 fluctuations with time.

1073 5. CONCLUSIONS

1074 To demonstrate the representativeness of the Widerøefjellet CS collection, the physicochemical
1075 properties of the CSs in this deposit, including cumulative size distribution, frequency by type and
1076 chemical composition, presence of vesicles and high-density phases, major and trace element
1077 chemical compositions, and oxygen isotope ratios, have been compared to those of other Antarctic
1078 MM deposits, including the TAM and SPWW collections. Although the Widerøefjellet deposit
1079 contains unmelted and scoriaceous MMs (< 5% of all MMs) as well as both silicate- and metal-
1080 rich CSs (~95% and ~5% of all CSs, respectively), this work focused on characterizing the silicate-
1081 rich CSs larger than 200 μm . All major textural (V-, BO-, CC-, and Po-type) and chemical (normal,
1082 CAT-like, high Ca-Al) CS groups are present. Most particles appear relatively unaltered, while the
1083 proportions for each CS type are comparable to those of the least biased Antarctic collections.
1084 While the molar Fe/(Mg + Si) ratios of the studied CSs are similar to that of the SPWW, a higher
1085 proportion of V-type CSs relative to other deposits was found. A relatively unbiased cumulative
1086 size distribution plot supports the claim of an essentially representative MM deposit. The -4.4
1087 exponent slope of the size distribution is similar to that of the TAM collection, suggesting direct
1088 infall to be the dominant process controlling the MM accumulation. The widely varying degree of
1089 alteration for Widerøefjellet and TAM particles, from fresh to heavily altered, confirms the long
1090 accumulation ranges from respectively ~ 3 and ~ 4 Myr ago to present.

1091 A subset of Widerøefjellet CSs larger than 325 μm was characterized for major and trace
1092 element concentrations and oxygen isotope ratios. The collected data confirm the major trends
1093 observed in literature, linking the Widerøefjellet CSs to chondritic precursors and their
1094 mineralogical constituents, which underwent chemical changes during atmospheric passage.
1095 Various factors control the CS composition, including the primary characteristics of the parent
1096 body precursors, expulsion of high-density phases (including metal bead, sulfides, and spinel
1097 crystals) as well as evaporation linked to differential redox and thermal conditions following
1098 atmospheric entry, and subsequent terrestrial alteration. The parent bodies of MMs are thought to
1099 differ from those sampled by normal-sized meteorites due to different production and transport
1100 mechanisms. At least 50% by number of CSs from all size fractions relate to primitive solar system
1101 objects with carbonaceous chondrite compositions, either to the C-, D-, or P-type spectral class
1102 asteroids in the outer asteroid belt or, alternatively, to comets. The contribution of ordinary
1103 chondrite particles shows larger variations, and strongly depends on the size fraction of the

1104 particles studied. A relatively constant proportion of CSs (~10%) is related to a chondritic reservoir
1105 depleted in ^{16}O . Overall, the physicochemical properties of the Widerøefjellet particles denote a
1106 distinctive and representative collection of CSs from East Antarctica, including a statistically
1107 significant number of particles with diameters larger than 800 μm . The Widerøefjellet collection
1108 complements currently existing collections and offers an important addition to study the
1109 composition of the MM flux over the last few million years.

1110 **ACKNOWLEDGEMENTS**

1111 This work was made possible by the 2009 Baillet Latour Antarctica Fellowship to SG.
1112 Additional support was provided by the Interuniversity Attraction Poles Program (IUAP)
1113 Planet Topers and BRAIN-be BAMB! projects initiated by the Belgian Science Policy
1114 Office and the FWO/FNRS Excellence of Science project ET-HoME (ID 30442502). SG
1115 and PhC also acknowledge continuous funding by the VUB Strategic Research Council.
1116 VD thanks the FRS-FNRS and ERC StG “ISoSyC” for support. FV thanks BOF-UGent for
1117 financial support under the form of a GOA project. SVM is a postdoctoral fellow of the
1118 FWO and acknowledges the financial and logistic support from the Research Foundation -
1119 Flanders (FWO, research project 12S5718N). All authors would like to acknowledge the
1120 Centre for X-ray Tomography at Ghent University, Belgium, for the performed
1121 experiments. VC acknowledges the Ghent University Special Research Fund (BOF-
1122 UGent) for financial support to BOF.EXP.2017.0007. Oxygen isotope studies at the Open
1123 University are funded by a consolidated grant from the Science and Technology Facilities
1124 Council, UK (STFC grant ST/P000657/1). The reported oxygen isotope data in this work
1125 was measured in the framework of Europlanet 2020 Research Infrastructure Transnational
1126 Access project 15-EPN-033. Europlanet 2020 RI has received funding from the European
1127 Union's Horizon 2020 research and innovation program under grant agreement No 654208.
1128 This work benefited significantly from support in the field by Alain Hubert and the
1129 International Polar Foundation. We extend our gratitude to O. Steenhaut, L. Pittarello, C.
1130 Ventura-Bordenca, T. De Kock, C. Suavet, P. Rochette, and L. Folco for their help and
1131 advice during various phases of this work. We thank Martin Suttle and 2 anonymous
1132 reviewers as well as associate editor Rhian Jones for their detailed comments and
1133 suggestions that helped to improve this manuscript significantly.

1134 **TABLE CAPTIONS**

1135 Table 1. Average major (oxide wt.%) and trace (ppm) element composition with standard
1136 deviations (1 SD; *italic*) of textural and chemical groups of cosmic spherules determined
1137 by electron microprobe analysis (EMPA) and laser ablation-inductively coupled plasma-
1138 mass spectrometry (LA-ICP-MS), compared to the literature values compiled by Folco and
1139 Cordier (2015) for particles from other micrometeorite collections.

1140

1141 Table 2. Three-oxygen isotope data for a selection of cosmic spherules from the
1142 Widerøefjellet collection, in addition to the textural group, apparent diameter and mass,
1143 degree of alteration as determined using SEM-EDS, and the presence of vesicles and high-
1144 density phases based on μ CT images. A rudimentary classification summarizing to which
1145 oxygen isotopic group, as identified by Suavet et al. (2010), each particle belongs, is also
1146 included (see text for additional explanation).

1147

1148 Table 3. Distribution by textural type for Widerøefjellet (WF), Frontier Mountain (FRO),
1149 Miller Butte (MIL), Larkman nunatak (LAR), Walcott Névé (WAL), South Pole Water
1150 Well (SPWW), and Indian Ocean (IO) cosmic spherules. The FRO and MIL data represent
1151 mostly magnetically separated fractions, while for the WAL data, a separation was made
1152 with heavy liquids and the light fraction was further sorted magnetically. The IO particles
1153 were separated magnetically, while the non-magnetic fractions did not yield any cosmic
1154 spherules after heavy liquid separation. Magnetic separation techniques were employed for
1155 some of the LAR samples to concentrate MMs. For the SPWW and WF collections, no
1156 bias was introduced. Data for all collections but Widerøefjellet compiled in Suavet et al.
1157 (2009), Shyam Prasad et al. (2013), and Genge et al. (2018).

1158

1159 Table 4. Parentage statistics for 28 silicate cosmic spherules determined in this work,
1160 compared to previously compiled literature data (Cordier and Folco, 2014).

1161

1162 **FIGURE CAPTIONS**

1163 Figure 1. Location of the Sør Rondane Mountains within Antarctica, the sites of the
1164 Princess Elisabeth (Belgium) and former Asuka (Japan) Antarctic research stations
1165 (circles), and the position of the Widerøefjellet CS accumulation site (star) relative to the
1166 Sør Rondane Mountains. Map adapted after Suganuma et al. (2014).

1167

1168 Figure 2. Widerøefjellet CS accumulation site in the Sør Rondane Mountains. (A) Map
1169 detail of the Widerøefjellet site within the Sør Rondane Mountains region, where the CSs
1170 described in this work have been recovered. The orange line highlights the track used to
1171 reach this site, the black dashed lines represent contour lines that connect points of equal
1172 elevation (height) in meter above sea level (masl). (B) View on the Widerøefjellet summit
1173 ridge (72°09'S, 23°17'E, 2755 masl), with the box highlighting the approximate location
1174 of the MM accumulation site. Orientation and dominant wind direction are also indicated.
1175 (C-D) After removal of the largest rock fragments and boulders, the surface delineated by
1176 the orange dashed line in (D) yielded the described collection of CSs.

1177

1178 Figure 3. Back-scattered electron images of silicate cosmic spherules characterized in this
1179 work. (A) V-type CS WF1202B-0001, displaying limited alteration. (B) Section through
1180 the same spherule. (C) V-type cosmic spherule WF1202B-0057, exhibiting a more altered,
1181 crackled surface relative to (A). (D) BO-type CS WF1202B-0013. (E) Section of the same
1182 spherule indicating local dissolution of the interstitial glass. (F) Textural detail of the same
1183 spherule showing Mg-rich olivine bars (dark grey) and magnetite crystallites (white) in Fe-
1184 rich glass (grey). (G) CC-type CS WF1202B-0030 with characteristic turtle-back
1185 (polyhedral-like) morphology. (H) A section through the same particle. (I) Textural detail
1186 of the same sectioned spherule showing olivine (grey) and magnetite crystallites (white).
1187 (J) Po-type CS WF1202B-0025, consisting mainly of olivine microphenocrysts (dark grey)
1188 in glass (grey) and magnetite (white). (K) A section through the same spherule. Note the
1189 presence of two larger, relict mineral phases, which have partially been resorbed due to
1190 atmospheric heating (indicated by arrows). (L) Textural detail of the same sectioned
1191 spherule showing microphenocryst with variable Fe-Mg contents. (M) Cosmic spherule
1192 WF1202B-0071, exhibiting a mixed BO/CC-type texture. (N) μ PO-type CS WF1202B-

1193 0073. (O) Po-type “*Group 4*” CS WF1202B-0070. (P) Irregular CS WF1202B-0079.
1194 Particles WF1202B-0001, 0013, 0025 and 0030 were sectioned and characterized using
1195 EMPA and LA-ICP-MS, while CSs WF1202B-0057, 0070, 0071, 0073 and 0079 were
1196 analyzed as a whole for oxygen isotope ratios using LF-IRMS.

1197

1198 Figure 4. (A) Cumulative size distribution for CSs from the Widerøefjellet (>200 μm size
1199 fraction, filled diamonds) and Transantarctic Mountains (>400 μm size fraction, filled
1200 circles) collections. The slopes are calculated for all samples with diameters larger than
1201 240 μm and 440 μm , respectively, following the method described in Suavet et al. (2009).
1202 (B) Comparison of size distributions for CSs characterized for oxygen isotope ratios to
1203 those characterized for major and trace element concentrations.

1204

1205 Figure 5. Micro computer-assisted X-ray tomographic renderings for four CSs,
1206 highlighting the presence of metal beads (red), vesicle inclusions, or both. BO-type CSs
1207 WF1202B-0002 (A), WF1202B-0042 (C) and WF1202B-0052 (D), and V-type CS
1208 WF1202B-0021 (B). Additional cross-sections are provided in Supplementary Fig. S2.

1209

1210 Figure 6. Molar Fe/(Si+Mg) histograms for Widerøefjellet Mountain (WF; this work),
1211 Frontier Mountain (FRO, magnetic extract; Suavet et al., 2009), Miller Butte (MIL; Suavet
1212 et al., 2009), Walcott Névé (WAL, heavy fraction [methylene iodide, $\rho = 3300 \text{ kg/m}^3$] and
1213 magnetic extract of the light fraction; Suavet et al., 2009) and South Pole Water Well
1214 (SPWW; Taylor et al., 2000) micrometeorites. All data except for Widerøefjellet extracted
1215 from Suavet et al. (2009).

1216

1217 Figure 7. Ternary atomic Mg-Si-Fe (A) and K+Na-Ca-Al (B) diagrams presenting EMPA
1218 data for a selection of CSs (V-type, BO-type, CC-type, and Po-type) recovered from the
1219 Widerøefjellet sedimentary accumulation. The elemental ranges for Antarctic volcanic
1220 rocks and tephra are based on those compiled in Rochette et al. (2008) and Suavet et al.
1221 (2009), while individual compositions of V-type CSs by Cordier et al. (2011b) are also
1222 shown. The ranges for CSs are based on other Antarctic, Greenland, and deep-sea

1223 collections (Taylor et al., 2000). Also indicated are a range of compositions of Australasian
1224 micrometeorites from the Transantarctic Mountains (Folco et al., 2009).

1225

1226 Figure 8. Classification diagrams for silicate CSs (see details in Folco and Cordier, 2015
1227 for A, B, and D). (A) Relationships between Fe/Mn and Fe/Mg atomic ratios. Field for
1228 chondrites and trends for achondrites are based on Goodrich and Delaney (2000). (B) CaO
1229 + Al₂O₃ content in wt.% versus Fe/Si atomic ratio. The definition for the three groups of
1230 chondritic V-type CSs are based on estimates by Taylor et al. (2000) and Cordier et al.
1231 (2011b). (C) Refractory lithophile major element content as the sum of CaO and Al₂O₃ in
1232 wt.% versus refractory lithophile trace element content, taken here as the sum of Sc, Y, Zr,
1233 and Hf in ppm. (D) Mg/Al versus Si/Al atomic ratios. An evaporation trajectory is drawn
1234 from the Ivuna-type (CI) carbonaceous chondrite precursor (fields from Jarosewich, 1990).
1235 Regardless of the starting composition, evaporation trajectories for carbonaceous and
1236 ordinary chondritic compositions converge after ~30% of the material has evaporated
1237 (Alexander et al., 2002). The arrows labeled “enstatite” and “forsterite” show the
1238 mineralogical control of precursor material on the bulk CS composition (CC =
1239 carbonaceous chondrite field; OC = ordinary chondrite field). V-type (Lit.) from Cordier
1240 et al. (2011b).

1241

1242 Figure 9. The categories of REE patterns observed among CSs of Widerøefjellet.
1243 Normalization to CI chondrite composition (McDonough and Sun, 1995). While five of
1244 the patterns correspond to those identified by Cordier et al. (2011b), the LREE-enriched
1245 patterns in (F) differ slightly from the previously identified “U-shaped” pattern.

1246

1247 Figure 10. Comparison of major and trace element compositions for the normal V-type,
1248 BO-type, and CC-type, CAT-like, and high Ca-Al CS groups recognized among the
1249 Widerøefjellet particles and in literature (Folco and Cordier, 2015; Table 1).
1250 Concentrations are normalized to CI chondrites (McDonough and Sun, 1995). Elements
1251 are ordered according to increasing volatility (i.e. 50% decreasing condensation T_C at 10⁻⁴
1252 bar; Lodders, 2003) from left to right.

1253

1254 Figure 11. (A-C) Binary plots of (partially) siderophile elements V, Cr, and Ni versus
1255 FeO*, as determined by LA-ICP-MS in this work. Fields for ordinary chondrites and
1256 carbonaceous chondrites (2 SD of the mean) based on Cr, Ni, and FeO* data from
1257 Jarosewich (1990) and V data from Friedrich et al. (2002). (D-F) Comparison of average
1258 major and trace refractory element concentrations in residues of heating experiments with
1259 varying total weight loss in % (Wang et al., 2001) with the CAT-like and high Ca-Al CS
1260 patterns determined in this work. The compositions of the CSs are normalized to CI
1261 chondrite (McDonough and Sun, 1995), while those of the residues are normalized to the
1262 starting solar composition (Wang et al., 2001).

1263

1264 Figure 12. $\delta^{18}\text{O}$ (horizontal) versus $\Delta^{17}\text{O}$ (vertical) in ‰ versus V-SMOW for the
1265 individual CSs from Widerøefjellet measured in this work compared to literature IRMS
1266 data for (A) Antarctic CSs (Suavet et al. 2010, 2011a; Cordier et al. 2011b, 2012) and (B)
1267 CSs from the Atacama Desert in Chile (open symbols; van Ginneken et al., 2017). The data
1268 from this work are shown by orange squares in (A) and filled dark grey symbols in (B).
1269 The solid line labeled TFL represents the terrestrial fractionation line ($\approx \delta^{17}\text{O} = 0.52 \times$
1270 $\delta^{18}\text{O}$), while the average isotopic composition of oxygen around the transition from the
1271 stratosphere to the mesosphere ($\delta^{18}\text{O} \approx 23.5\text{‰}$ and $\delta^{17}\text{O} \approx 11.8\text{‰}$; Thiemens et al., 1995)
1272 is represented by a star. Plot (A) is adapted after Suavet et al. (2010) and Cordier and Folco
1273 (2014), with colored domains representing potential parent bodies (Clayton et al., 1991;
1274 Schulze et al., 1994; Clayton and Mayeda, 1999; Newton et al., 2000) and shaded areas
1275 indicating the range of possible values for a micrometeorite derived from a particular parent
1276 body. Mass fractionation lines for asteroid 4 Vesta (EFL, $\Delta^{17}\text{O} = -0.242 \pm 0.016\text{‰}$; Scott
1277 et al., 2009) and Mars (MFL, $\Delta^{17}\text{O} = 0.301 \pm 0.013\text{‰}$; Franchi et al., 1999) are also shown.
1278 The outlines of the 4 groups originally identified by Suavet et al. (2010) are represented
1279 using dotted lines, while the dashed arrows reflect the direction of possible shifts due to
1280 the formation of alteration products in equilibrium with Antarctic precipitation. Individual
1281 CSs are highlighted using their number designation only, as these all share the common
1282 prefix “WF1202B-”. Plot (B) includes textural information on the individual particles and
1283 illustrates the three possible effects by which the bulk O isotopic composition of a CS can
1284 be changed starting from chondritic parent body values. Analytical uncertainties for IRMS

1285 measurements are $\pm 0.42\text{‰}$ for $\delta^{18}\text{O}$ and $\pm 0.04\text{‰}$ for $\Delta^{17}\text{O}$ (2σ). As ion microprobe data are
1286 generally associated with larger uncertainties ($\pm 1\text{‰}$ for $\delta^{18}\text{O}$ and ± 0.7 for $\Delta^{17}\text{O}$) and show
1287 much larger variability because of the characterization of individual mineral phases, such
1288 literature data are not included here.

1289 **REFERENCES**

- 1290 Alexander C. M. O., Taylor S., Delaney J. S., Ma P. and Herzog G. F. (2002) Mass-
1291 dependent fractionation of Mg, Si, and Fe isotopes in five stony cosmic spherules.
1292 *Geochim. Cosmochim. Acta* **66**, 173–183.
1293
- 1294 Alexander C. M. O., Greenwood R. C., Bowden R., Gibson J. M., Howard K. T. and
1295 Franchi I. A. (2018) A multi-technique search for the most primitive CO chondrites.
1296 *Geochim. Cosmochim. Acta* **221**, 406–420.
1297
- 1298 Beaudoin G. and Therrien P. (2009) The updated web stable isotope fractionation
1299 calculator. In *Handbook of Stable Isotope Analytical Techniques* (ed. P. A. DeGroot).
1300 Elsevier, Amsterdam, Netherlands. pp. 1120–1122.
1301
- 1302 Blanchard M. B., Brownlee D. E., Bunch T. E., Hodge P. W. and Kyte F. T. (1980)
1303 Meteoroid ablation spherules from deep-sea sediments. *Earth Planet. Sci. Lett.* **46**, 178–190.
1304
- 1305 Brownlee D. E., Pilachowski L. B. and Hodge P. W. (1979) Meteorite mining on the ocean
1306 floor. *Lunar Planet. Sci. Conf. X*. Lunar Planet. Inst., Houston. #157–158 (abstr.).
1307
- 1308 Brownlee D. E., Bates B. A. and Wheelock M. M. (1984) Extraterrestrial platinum group
1309 nuggets in deep-sea sediments. *Nature* **309**, 693–695.
1310
- 1311 Brownlee D. E., Bates B. and Schramm L. (1997) The elemental composition of stony
1312 cosmic spherules. *Meteorit. Planet. Sci.* **32**, 157–175.
1313
- 1314 Choi B.-G., McKeegan K. D., Krot A. N. and Wasson J. T. (1998) Extreme oxygen-isotope
1315 compositions in magnetite from unequilibrated ordinary chondrites. *Nature* **392**, 577–579.
1316
- 1317 Clayton R. N. (1993) Oxygen isotopes in meteorites. *Annu. Rev. Earth Planet. Sci.* **21**,
1318 115–149.
1319

1320 Clayton R. N. and Mayeda T. K. (1999) Oxygen isotope studies of carbonaceous
1321 chondrites. *Geochim. Cosmochim. Acta* **63**, 2089–2104.
1322

1323 Clayton R. N., Mayeda T. K., Olsen E. J. and Goswami J. N. (1991) Oxygen isotope studies
1324 of ordinary chondrites. *Geochim. Cosmochim. Acta* **55**, 2317–2337.
1325

1326 Cordier C. and Folco L. (2014) Oxygen isotopes in cosmic spherules and the composition
1327 of the near Earth interplanetary dust complex. *Geochim. Cosmochim. Acta* **146**, 18–26.
1328

1329 Cordier C., Folco L. and Taylor S. (2011a) Vestoid cosmic spherules from the South Pole
1330 Water Well and Transantarctic Mountains (Antarctica): A major and trace element study.
1331 *Geochim. Cosmochim. Acta* **75**, 1199–1215.
1332

1333 Cordier C., Folco L., Suavet C., Sonzogni C. and Rochette P. (2011b) Major, trace element
1334 and oxygen isotope study of glass cosmic spherules of chondritic composition: The record
1335 of their source material and atmospheric entry heating. *Geochim. Cosmochim. Acta* **75**,
1336 5203–5218.
1337

1338 Cordier C., van Ginneken M. and Folco L. (2011c) Nickel abundance in stony cosmic
1339 spherules: Constraining precursor material and formation mechanisms. *Meteorit. Planet.*
1340 *Sci.* **46**, 1110–1132.
1341

1342 Cordier C., Suavet C., Folco L., Rochette P. and Sonzogni C. (2012) HED-like cosmic
1343 spherules from the Transantarctic Mountains, Antarctica: Major and trace element
1344 abundances and oxygen isotopic compositions. *Geochim. Cosmochim. Acta* **77**, 515–529.
1345

1346 Cordier C., Baecker B., Ott U, Folco L. and Trieloff M. (2018) A new type of oxidized and
1347 pre-irradiated micrometeorite. *Geochim. Cosmochim. Acta* **233**, 135–158.
1348

1349 Dartois E., Engrand C., Brunetto R., Duprat J., Pino T., Quirico E., Remusat L., Bardin N.,
1350 Briani G., Mostefaoui S., Morinaud G., Crane B., Szwec N., Delauche L., Jamme F., Sandt

1351 Ch. and Dumas P. (2013) Ultracarbonaceous Antarctic micrometeorites, probing the Solar
1352 System beyond the nitrogen snow-line. *Icarus* **224**, 243–252.
1353

1354 Dobrică E., Engrand C., Duprat J. and Gounelle M. (2010) A statistical overview of
1355 Concordia Antarctic micrometeorites. In *73rd Ann. Meet. of Meteorit. Soc. New York, N.Y.,*
1356 *USA. #5213* (abstr.).
1357

1358 Dobrică E., Engrand C., Leroux H., Rouzaud J.-N. and Duprat J. (2012) Transmission
1359 electron microscopy of CONCORDIA UltraCarbonaceous Antarctic MicroMeteorites
1360 (UCAMMs): Mineralogical properties. *Geochim. Cosmochim. Acta* **76**, 68-82.
1361

1362 Duprat J., Maurette M., Engrand C., Matrajt G., Immel G., Gounelle M. and Kurat G.
1363 (2001) An estimation of the contemporary micrometeorite flux obtained from surface snow
1364 samples collected in central Antarctica. *Meteorit. Planet. Sci.* **36**, A52 (abstr.).
1365

1366 Duprat J., Engrand C., Maurette M., Kurat G., Gounelle M. and Hammer C. (2007)
1367 Micrometeorites from central Antarctic snow: The CONCORDIA collection. *Adv. Space*
1368 *Res.* **39**, 605–611.
1369

1370 Duprat J., Dobrica E., Engrand C., Aleon J., Marrocchi Y., Mostefaoui S., Meibom A.,
1371 Leroux H., Rouzaud J.-N., Gounelle M. and Robert F. (2010) Extreme deuterium excesses
1372 in Ultracarbonaceous Micrometeorites from central Antarctic snow. *Science* **328**, 742-745.
1373

1374 Engrand C. and Maurette M. (1998) Carbonaceous micrometeorites from Antarctica.
1375 *Meteorit. Planet. Sci.* **33**, 565–580.
1376

1377 Engrand C., McKeegan K. D. and Leshin L. (1999) Oxygen isotopic compositions of
1378 individual minerals in Antarctic micrometeorites: Further links to carbonaceous chondrites.
1379 *Geochim. Cosmochim. Acta* **63**, 2623–2636.
1380

1381 Engrand C., McKeegan K. D., Leshin L. A., Herzog G. F., Schnabel C., Nyquist L. E. and
1382 Brownlee D. E. (2005) Isotopic compositions of oxygen, iron, chromium, and nickel in
1383 cosmic spherules: toward a better comprehension of atmospheric entry heating effects.
1384 *Geochim. Cosmochim. Acta* **69**, 5365–5385.

1385

1386 Floss C., Goresy A. E., Zinner E., Kransel G., Rammensee W. and Palme H. (1996)
1387 Elemental and isotopic fractionations produced through evaporation of the Allende CV
1388 chondrite: implications for the origin of HAL-type hibonite inclusions. *Geochim.*
1389 *Cosmochim. Acta* **60**, 1975–1997.

1390

1391 Flynn G. J., Durda D. D., Sandel L. E., Kreft J. W. and Strait M. M. (2009) Dust production
1392 from the hypervelocity impact disruption of the Murchison hydrous CM2 meteorite:
1393 Implications for the disruption of hydrous asteroids and the production of interplanetary
1394 dust. *Planet. Space Sci.* **57**, 119–126.

1395

1396 Folco L. and Cordier C. (2015) Micrometeorites. In *EMU Notes in Mineralogy 15:*
1397 *Planetary Mineralogy* (eds. M. R. Lee and H. Leroux). European Mineralogical Union,
1398 Twickenham, United Kingdom. pp. 253–297.

1399

1400 Folco L., Rochette P., Perchiazzi N., D’Orazio M., Laurenzi M. and Tiepolo M. (2008)
1401 Microtektites from Victoria Land Transantarctic Mountains. *Geology* **36**, 291–294.

1402

1403 Folco L., D’Orazio M., Tiepolo M., Tonarini S., Ottolino L., Perchiazzi N. and Rochette
1404 P. (2009) Transantarctic Mountain microtektites: geochemical affinity with Australasian
1405 microtektites. *Geochim. Cosmochim. Acta* **73**, 3694–3722.

1406

1407 Franchi I. A., Wright I. P., Sexton A. S. and Pillinger C. T. (1999) The oxygen-isotopic
1408 composition of Earth and Mars. *Meteorit. Planet. Sci.* **34**, 657–661.

1409

1410 Franchi I. A., Baker L., Bridges J. C., Wright I. P. and Pillinger C. T. (2001) Oxygen
1411 isotopes and the early solar system. *Philos. Trans. R. Soc. A* **359**, 2019–2035.

1412

1413 Fredriksson K. and Martin L. R. (1963) The origin of black spherules found in Pacific
1414 islands, deep sea sediments, and Antarctic ice. *Geochim. Cosmochim. Acta* **27**, 245–248.

1415

1416 Friedrich J. M., Wang M.-S. and Lipschutz M. E. (2002) Comparison of the trace element
1417 composition of Tagish Lake with other primitive carbonaceous chondrites. *Meteorit.*
1418 *Planet. Sci.* **37**, 677–686.

1419

1420 Ganapathy R., Brownlee D. E. and Hodge P. W. (1978) Silicate spherules from deep sea
1421 sediments: Confirmation of extraterrestrial origin. *Science* **201**, 1119–1121.

1422

1423 Genge M. J. (2008) Koronis asteroid dust within Antarctic ice. *Geology* **36**, 687–690.

1424

1425 Genge M. J. and Grady M. M. (1998) Melted micrometeorites from Antarctic ice with
1426 evidence for the separation of immiscible Fe–Ni–S liquids during entry heating. *Meteorit.*
1427 *Planet. Sci.* **33**, 425–434.

1428

1429 Genge M. J. and Grady M. M. (1999) The fusion crusts of stony meteorites: implications
1430 for the atmospheric reprocessing of extraterrestrial materials. *Meteorit. Planet. Sci.* **34**,
1431 341–356.

1432

1433 Genge M. J., Grady M. M. and Hutchinson R. (1997) The textures and compositions of
1434 fine-grained Antarctic micrometeorites – Implications for comparisons with meteorites.
1435 *Geochim. Cosmochim. Acta* **61**, 5149–5162.

1436

1437 Genge M. J., Engrand C., Gounelle M. and Taylor S. (2008) The classification of
1438 micrometeorites. *Meteorit. Planet. Sci.* **43**, 497–515.

1439

1440 Genge M. J., Suttle M. and van Ginneken M. (2016) Olivine settling in cosmic spherules
1441 during atmospheric deceleration: An indicator of the orbital eccentricity of interplanetary
1442 dust. *Geophys. Res. Lett.* **43**, 10646–10653.

1443

1444 Genge M. J., Larsen J., Suttle M. D., and van Ginneken M. (2017) An urban collection of
1445 modern-day large micrometeorites: Evidence for variations in the extraterrestrial dust flux
1446 through the Quaternary. *Geology* **45**, 119–122.

1447

1448 Genge M. J., van Ginneken M., Suttle M. D. and Harvey R. P. (2018) Accumulation
1449 mechanisms of micrometeorites in an ancient supraglacial moraine at Larkman Nunatak,
1450 Antarctica. *Meteorit. Planet. Sci.* **53**, 2051–2066.

1451

1452 Gorodetskaya I. V., Van Lipzig N. P. M., Van den Broeke M. R., Mangold A., Boot W.
1453 and Reijmer C. H. (2013) Meteorological regimes and accumulation patterns at Utsteinen,
1454 Dronning Maud Land, East Antarctica: Analysis of two contrasting years. *J. Geophys.*
1455 *Res.-Atmos.* **118**, 1–16.

1456

1457 Goodrich C. A. and Delaney J. S. (2000) Fe/Mg-Fe/Mn relations of meteorites and primary
1458 heterogeneity of primitive achondrite parent bodies. *Geochim. Cosmochim. Acta* **64**, 149–
1459 160.

1460

1461 Gounelle M., Engrand C., Maurette M., Kurat G., McKeegan K. D. and Brandstätter F.
1462 (2005) Small Antarctic micrometeorites: A mineralogical and in situ oxygen isotopic study.
1463 *Meteorit. Planet. Sci.* **40**, 917–932.

1464

1465 Gounelle M., Chaussidon M., Morbidelli A., Barrat J.-A., Engrand C., Zolensky M. E. and
1466 McKeegan K. D. (2009) A unique basaltic micrometeorite expands the inventory of solar
1467 system planetary crusts. *Proc. Natl. Acad. Sci. USA* **106**, 6904–6909.

1468

1469 Greenwood R. C., Schmitz B., Bridges J. C., Hutchison R. and Franchi I. A. (2007)
1470 Disruption of the L chondrite parent body: new oxygen isotope evidence from Ordovician
1471 relict chromite grains. *Earth Planet. Sci. Lett.* **262**, 204–213.

1472

1473 Greenwood R. C., Burbine T. H., Miller M. F. and Franchi I. A. (2017) Melting and
1474 differentiation of early-formed asteroids: The perspective from high precision oxygen
1475 isotope studies. *Chem. Erde-Geochem.* **77**, 1-43.

1476

1477 Hagen E. H., Koeberl C. and Faure G. (1989) Extra-terrestrial spherules in glacial
1478 sediment, Beardmore-Glacier area, Transantarctic Mountains. *Contrib. Antarct. Res. I,*
1479 *Antarct. Res. Ser.* **50**, 19-24.

1480

1481 Harvey R. P. and Maurette M. (1991) The origin and significant of cosmic dust from
1482 Walcott Névé, Antarctica. *Proc. Lunar Planet. Sci. Conf.* **21**, 569–578.

1483

1484 Hashimoto A. (1990) Evaporation kinetics of forsterite and implications for the early solar
1485 nebula. *Nature* **347**, 53–55.

1486

1487 Imae N., Taylor S. and Iwata N. (2013) Micrometeorite precursors: Clues from the
1488 mineralogy and petrology of their relict minerals. *Geochim. Cosmochim. Acta* **100**, 113–
1489 157.

1490

1491 Imae N., Debaille V., Akada Y., Debouge W., Goderis S., Hublet G., Mikouchi T., Van
1492 Roosbroek N., Yamaguchi A., Zekollari H., Claeys Ph. and Kojima H. (2015) Report of
1493 the JARE-54 and BELARE 2012-2013 joint expedition to collect meteorites on the Nansen
1494 Ice Field, Antarctica. *Antarct. Rec.* **59**, 38–72.

1495

1496 Jarosewich E. (1990) Chemical analysis of meteorites: A compilation of stony and iron
1497 meteorite analyses. *Meteoritics* **25**, 323–337.

1498

1499 Kamei A., Horie K., Owada M., Yuhara M., Nakano N., Osanai Y., Adachi T., Hara Y.,
1500 Terao M., Teuchi S., Shimura T., Tsukada K., Hokada T., Iwata C., Shiraishi K., Ishizuka
1501 H. and Takahashi Y. (2013) Late Proterozoic juvenile arc metatonalite and adakitic
1502 intrusions in the Sør Rondane Mountains, eastern Dronning Maud Land, Antarctica.
1503 *Precambrian Res.* **234**, 47–62.

1504
1505 Koeberl C. and Hagen E.H. (1989) Extraterrestrial spherules in glacial sediment from the
1506 Transantarctic Mountains, Antarctica: Structure, mineralogy, and chemical composition.
1507 *Geochim. Cosmochim. Acta* **53**, 937–944.
1508
1509 Kojima S. and Shiraishi K. (1986) Note on the geology of the western part of the Sør
1510 Rondane Mountains, East Antarctica. *Mem. Natl. Inst. Polar Res.* **43**, 116–131.
1511
1512 Kortenkamp S. J. (1998) Accretion of interplanetary dust particles by the Earth. *Icarus* **135**,
1513 469–495.
1514
1515 Kurat G., Koeberl, C., Presper, T., Brandstätter F. and Maurette M. (1994) Petrology and
1516 geochemistry of Antarctic micrometeorites. *Geochim. Cosmochim. Acta* **58**, 3879–3904.
1517
1518 Lodders K. (2003) Solar system abundances and condensation temperatures of the
1519 elements. *Astrophys. J.* **591**, 1220–1247.
1520
1521 Longhi J. and Pan V. (1988) A reconnaissance study of phase boundaries in low-alkali
1522 basaltic liquids. *Journal of Petrology* **29**, 115–147.
1523
1524 Love S. G. and Brownlee D. E. (1993) A direct measurement of the terrestrial mass
1525 accretion rate of cosmic dust. *Science* **262**, 550–553.
1526
1527 Martin C., Debaille V., Lanari P., Goderie S., Vandendael I., Vanhaecke F., Vidal O. and
1528 Claeys Ph. (2013) REE and Hf distribution among mineral phases in the CV–CK clan: A
1529 way to explain present-day Hf isotopic variations in chondrites. *Geochim. Cosmochim.*
1530 *Acta* **120**, 496–513.
1531
1532 Masschaele B. C., Cnudde V., Dierick M., Jacobs P., Van Hoorebeke L. and Vlassenbroeck
1533 J. (2007) UGCT: New X-ray radiography and tomography facility. *Nucl. Instrum. Meth. A*
1534 **580**, 266–269.

1535
1536 Masschaele B. C., Dierick M., Loo D. V., Boone M. N., Brabant L., Pauwels E., Cnudde
1537 V., and Hoorebeke L. V. (2013) HECTOR: A 240kV micro-CT setup optimized for
1538 research. *J. Phys. Conf. Ser.* **463**(1), 012012, doi:10.1088/1742-6596/463/1/012012.
1539
1540 Maurette M., Immel G., Hammer C., Harvey R., Kurat G. and Taylor S. (1994) Collection
1541 and curation of IDPs from the Greenland and Antarctic ice sheets. In *Analysis of*
1542 *Interplanetary Dust Conference Proceedings* (eds. M. E. Zolensky, T. L. Wilson, F. J. M.
1543 Rietmeijer and G. J. Flynn). Am. Inst. Phys., Houston. pp. 277–289.
1544
1545 McDonough W. F. and Sun S. S. (1995) The composition of the Earth. *Chem. Geol.* **120**,
1546 223–253.
1547
1548 Miller M. F., Franchi I. A., Sexton A. S. and Pillinger C. T. (1999) High precision $\delta^{17}\text{O}$
1549 isotope measurements of oxygen from silicates and other oxides: method and applications.
1550 *Rapid Commun. Mass Sp.* **13**, 1211–1217.
1551
1552 Moriwaki K., Hirakawa K. and Matsuoka N. (1991) Weatering stafe of till and glacial
1553 history of the central Sør Rondane Mountains, East Antarctica. *Proc. NIPR. Sym. Antarct.*
1554 *Geosci.* **5**, 99–111.
1555
1556 Nakamura T., Imae N., Nakai I., Noguchi T., Yano H., Terada K. and Ohmori R. (1999)
1557 Antarctic micrometeorites collected at the Dome Fuji Station. *Antarct. Meteorite Res.* **12**,
1558 183–198.
1559
1560 Nakamura T., Noguchi T., Tsuchiyama A., Ushikubo T., Kita N. K., Valley J. Y., Zolensky
1561 M. E., Kakazu Y., Sakamoto K., Mashio E., Uesugi K. and Nakano T. (2008) Chondrule-
1562 like objects in short-period comet 81P/Wild 2. *Science* **321**, 1664–1667.
1563
1564 Nesvorný D., Bottke W. F., Dones L. and Levison H. F. (2002) The recent breakup of an
1565 asteroid in the main-belt region. *Nature* **417**, 720–771.

1566
1567 Nesvorný D., Jenniskens P., Levison H. F., Bottke W. F., Vokrouhlicky D. and Gounelle
1568 M. (2010) Cometary origin of the zodiacal cloud and carbonaceous micrometeorites.
1569 Implications for hot debris disks. *Astrophys. J.* **713**, 816–836.
1570
1571 Newton J., Franchi I. A. and Pillinger C. T. (2000) The oxygen-isotopic record in enstatite
1572 meteorites. *Meteorit. Planet. Sci.* **35**, 689–698.
1573
1574 Nishiizumi K., Kohl C. P. Arnold J. R., Klein J., Fink D. and Middleton R. (1991) Cosmic
1575 ray produced ^{10}Be and ^{26}Al in Antarctic rocks: exposure and erosion history. *Earth*
1576 *Planet. Sci. Lett.* **104**, 440–454.
1577
1578 Noguchi T., Nakamura T. and Nozaki W. (2002) Mineralogy of phyllosilicate-rich
1579 micrometeorites and comparison with Tagish Lake and Sayama meteorites. *Earth Planet.*
1580 *Sci. Lett.* **202**, 229–246.
1581
1582 Pattyn F., Matsuoka K. and Berte J. (2010) Glacio-meteorological conditions in the vicinity
1583 of the Belgian Princess Elisabeth Station, Antarctica. *Antarct. Sci.* **22**, 79–85.
1584
1585 Raisbeck G. M., Yiou F., Bourles D. and Maurette M. (1986) ^{10}Be and ^{26}Al in Greenland
1586 cosmic spherules: Evidence for irradiation in space as small objects and a probable
1587 cometary origin. *Meteoritics* **21**, 487–488.
1588
1589 Rochette P., Folco L., Suavet C., van Ginneken M., Gattacceca J., Perchiazzi N., Braucher
1590 R. and Harvey R. P. (2008) Micrometeorites from the Transantarctic Mountains. *Proc.*
1591 *Natl. Acad. Sci. USA* **105**, 18206–18211.
1592
1593 Roeder P. L. and Reynolds I. (1991) Crystallization of chromite and chromium solubility
1594 in basaltic melts. *Journal of Petrology* **32**, 909–934.
1595

1596 Rubin A. E. (2018) Mechanisms accounting for variations in the proportions of
1597 carbonaceous and ordinary chondrites in different mass ranges. *Meteorit. Planet. Sci.* **53**,
1598 2181–2192.

1599

1600 Rubin A. E. and Grossman J. N. (2010) Meteorite and meteoroid: New comprehensive
1601 definitions. *Meteorit. Planet. Sci.* **45**, 114–122.

1602

1603 Rudraswami N. G., Parashar K. and Shyam Prasad M. (2011) Micrometer- and nanometer-
1604 sized platinum group nuggets in micrometeorites from deep-sea sediments of the Indian
1605 Ocean. *Meteorit. Planet. Sci.* **46**, 470–491.

1606

1607 Rudraswami N. G., Shyam Prasad M., Babu E. V. S. S. K., Vijaya Kumar T., Feng W. and
1608 Plane J. M. C. (2012) Fractionation and fragmentation of glass cosmic spherules
1609 during atmospheric entry. *Geochim. Cosmochim. Acta* **99**, 110–127.

1610

1611 Rudraswami N. G., Shyam Prasad M., Nagashima K. and Jones R. H. (2015a) Oxygen
1612 isotopic composition of relict olivine grains in cosmic spherules: Links to chondrules from
1613 carbonaceous chondrites. *Geochim. Cosmochim. Acta* **164**, 53–70.

1614

1615 Rudraswami N. G., Shyam Prasad M., Dey S., Plane J. M. C., Feng W. and Taylor S.
1616 (2015b) Evaluating changes in the elemental composition of micrometeorites during entry
1617 into the Earth's atmosphere. *Astrophys. J.* **814**, 78, doi:10.1088/0004-637X/814/1/78.

1618

1619 Rudraswami N. G., Shyam Prasad M., Babu E. V. S. S. K. and Vijaya Kumar T. (2016)
1620 Major and trace element geochemistry of S-type cosmic spherules. *Meteorit. Planet. Sci.*
1621 **51**, 718–742.

1622

1623 Schulze H., Bischoff A., Palme H., Spettel B., Dreibus G. and Otto J. (1994) Mineralogy
1624 and chemistry of Rumuruti: The first meteorite fall of the new R chondrite group. *Meteorit.*
1625 *Planet. Sci.* **29**, 275–286.

1626

1627 Scott E. R., Greenwood R. C., Franchi I. A. and Sanders I. S. (2009) Oxygen isotopic
1628 constraints on the origin and parent bodies of eucrites, diogenites, and howardites.
1629 *Geochim. Cosmochim. Acta* **73**, 5835–5853.
1630

1631 Shiraishi K., Osanai Y., Ishizuka H. and Asami M. (1997) Geological Map of the Sør
1632 Rondane Mountains, Antarctica. Antarctic Geological Map Series, Sheet 35, Scale
1633 1:250,000. National Institute of Polar Research, Tokyo.
1634

1635 Shiraishi K., Dunkley D. J., Hokada T., Fanning C. M., Kagami H. and Hamamoto T.
1636 (2008) Geochronological constraints on the Late Proterozoic to Cambrian crustal evolution
1637 of eastern Dronning Maud Land, East Antarctica: a synthesis of SHRIMP U-Pb age and
1638 Nd model age data. In *Geodynamic Evolution of East Antarctica: A Key to the East-West
1639 Gondwana Connection* (eds. M. Satish-Kumar, Y. Motoyoshi, Y. Osanai, Y. Hiroi and K.
1640 Shiraishi). Geological Society, London, Special Publications, vol. 308. pp. 21–67.
1641

1642 Shyam Prasad M., Rudraswami N. G. and Panda D. K. (2013) Micrometeorite flux on Earth
1643 during the last ~50,000 years. *J. Geophys. Res.-Planet.* **118**, 2381–2399.
1644

1645 Starkey N. A., Franchi I. A. and Lee, M. R. (2014) Isotopic diversity in interplanetary dust
1646 particles and preservation of extreme ¹⁶O-depletion. *Geochim. Cosmochim. Acta*
1647 **142**, 115–131.
1648

1649 Steele A. (1992) Olivine in Antarctic micrometeorites: Comparison with other
1650 extraterrestrial olivine. *Geochim. Cosmochim. Acta* **56**, 2923–2929.
1651

1652 Suavet C., Rochette P., Kars M., Gattacceca J., Folco L. and Harvey R. P. (2009) Statistical
1653 properties of the Transantarctic Mountains (TAM) micrometeorite collection. *Polar Sci.* **3**,
1654 100–109.
1655

1656 Suavet C., Alexandre A., Franchi I. A., Gattacceca J., Sonzogni C., Greenwood R. C., Folco
1657 L. and Rochette P. (2010) Identification of the parent bodies of micrometeorites with high-
1658 precision oxygen isotope ratios. *Earth Planet. Sci. Lett.* **293**, 313–320.

1659

1660 Suavet C., Cordier C., Rochette P., Folco L., Gattacceca J., Sonzogni C. and Damphoffer
1661 D. (2011a) Ordinary chondrite related giant (>800 µm) cosmic spherules from the
1662 Transantarctic Mountains, Antarctica. *Geochim. Cosmochim. Acta* **75**, 6200–6210.

1663

1664 Suavet C., Gattacceca J., Rochette P. and Folco L. (2011b) Constraining the terrestrial age
1665 of micrometeorites using their record of the Earth's magnetic field polarity. *Geology* **39**,
1666 123–126.

1667

1668 Suganuma Y., Miura H., Zondervan A. and Okuno J. (2014) East Antarctic deglaciation
1669 and the link to global cooling during the Quaternary: evidence from glacial geomorphology
1670 and ¹⁰Be surface exposure dating of the Sør Rondane Mountains, Dronning Maud Land.
1671 *Quaternary Sci. Rev.* **97**, 102–120.

1672

1673 Suttle M. D., Folco L., Genge M. J., Russell S. S., Najorka J. and van Ginneken M. (2019)
1674 Intense aqueous alteration on C-type asteroids: Perspectives from giant fine-grained
1675 micrometeorites. *Geochim. Cosmochim. Acta* **245**, 352–373.

1676

1677 Taylor S. and Brownlee D. E. (1991) Cosmic spherules in the geological record.
1678 *Meteoritics* **26**, 203–211.

1679

1680 Taylor S. and Lever J. H. (2001) Seeking unbiased collections of modern and ancient
1681 micrometeorites. In *Accretion of extraterrestrial matter throughout Earth's history* (eds.
1682 B. Peucker-Ehrenbrink and B. Schmitz). Kluwer Academic/Plenum Publishers, New York.
1683 pp. 205–219.

1684

1685 Taylor S., Lever J. H. and Harvey R. P. (1998) Accretion rate of cosmic spherules measured
1686 at the South Pole. *Nature* **392**, 899–903.

1687
1688 Taylor S., Lever J. H. and Harvey R. P. (2000) Numbers, types and compositional
1689 distribution of an unbiased collection of cosmic spherules. *Meteorit. Planet. Sci.* **35**, 651–
1690 666.
1691
1692 Taylor S., Alexander C. M. O., Delaney J. S., Ma P., Herzog G. F. and Engrand C. (2005)
1693 Isotopic fractionation of iron, potassium, and oxygen in stony cosmic spherules:
1694 Implications for heating histories and sources. *Geochim. Cosmochim. Acta* **69**, 2647–2662.
1695
1696 Taylor S., Herzog G. F. and Delaney J. S. (2007a) Crumbs from the crust of Vesta:
1697 Achondritic cosmic spherules from the South Pole water well. *Meteorit. Planet. Sci.* **42**,
1698 223–233.
1699
1700 Taylor S., Matrajt G., Lever J. H., Joswiak D. J. and Brownlee D. E. (2007b) Size
1701 distribution of Antarctic micrometeorites. In *Workshop on Dust in Planetary Systems* (eds.
1702 H. Krueger and A. Graps). ESA, NY, pp. 145-148.
1703
1704 Taylor S., Matrajt G. and Guan Y. (2012) Fine-grained precursors dominate the
1705 micrometeorite flux. *Meteorit. Planet. Sci.* **47**, 550–564.
1706
1707 Thiemens M., Jackson T., Zipf E., Erdman P. W. and Van Egmond C. (1995) Carbon
1708 dioxide and oxygen isotope anomalies in the mesosphere and stratosphere. *Science* **270**,
1709 969–972.
1710
1711 van Ginneken M., Folco L., Perchiazzi N., Rochette P. and Bland P. A. (2010) Meteoritic
1712 ablation debris from the Transantarctic Mountains: Evidence for a Tunguska-like impact
1713 over Antarctica ca. 480 ka ago. *Earth Planet. Sci. Lett.* **293**, 104–113.
1714
1715 van Ginneken M., Folco L., Cordier C. and Rochette P. (2012) Chondritic micrometeorites
1716 from the Transantarctic Mountains. *Meteorit. Planet. Sci.* **47**, 228–247.
1717

1718 van Ginneken M., Genge M. J., Folco L. and Harvey R. P. (2016) The weathering of
1719 micrometeorites from the Transantarctic Mountains. *Geochim. Cosmochim. Acta* **179**, 1–
1720 31.

1721

1722 van Ginneken M., Gattacceca J., Rochette P., Sonzogni C., Alexandre A., Vidal V. and
1723 Genge M. J. (2017) The parent body controls on cosmic spherule texture: Evidence from
1724 the oxygen isotopic compositions of large micrometeorites. *Geochim. Cosmochim. Acta*
1725 **212**, 196-210.

1726

1727 Van Roosbroek N., Debaille V., Pittarello L., Goderis S., Humayun M., Hecht L., Jourdan
1728 F., Spicuzza M. J., Vanhaecke F. and Claeys Ph. (2015) The formation of IIE iron
1729 meteorites investigated by the chondrule-bearing Mont Dieu meteorite. *Meteorit. Planet.*
1730 *Sci.* **50**, 1173–1196.

1731

1732 Vlassenbroeck J., Dierick M., Masschaele B. C., Cnudde V., Van Hoorebeke L. and Jacobs
1733 P. (2007) Software tools for quantification of X-ray microtomography at the UGCT. *Nucl.*
1734 *Instrum. Meth. A* **580**, 442–445.

1735

1736 Wang J., Davis A. M., Clayton R. N., Mayeda T. K. and Hashimoto A. (2001) Chemical
1737 and isotopic fractionation during the evaporation of the FeO–MgO–SiO₂–CaO–Al₂O₃–
1738 TiO₂–REE melt system. *Geochim. Cosmochim. Acta* **65**, 479–494.

1739

1740 Welten K. C., Folco L., Nishiizumi K., Caffee M. W., Grimberg A., Meier M. M. M. and
1741 Kober F. (2008) Meteoritic and bedrock constraints on the glacial history of Frontier
1742 Mountain in northern Victoria Land, Antarctica. *Earth Planet. Sci. Lett.* **270**, 308–315.

1743

1744 Yada T., Nakamura T., Takaoka N., Noguchi T., Terada K., Yano H., Nakazawa T. and
1745 Kojiima H. (2004) The global accretion rate of extraterrestrial materials in the last glacial
1746 period estimated from the abundance of micrometeorites in Antarctic glacier ice. *Earth*
1747 *Planets Space* **56**, 67–79.

1748

1749 Yada T., Nakamura T., Noguchi T., Matsumoto N., Kusakabe M., Hiyagon H., Ushikubo
1750 T., Sugiura N., Kojima H. and Takaoka N. (2005) Oxygen isotopic and chemical
1751 compositions of cosmic spherules collected from the Antarctic ice sheet: Implications for
1752 their precursor material. *Geochim. Cosmochim. Acta* **69**, 5789–5804.
1753
1754 Zekollari H., Goderis S., Debaille V., van Ginneken M., Gattacceca J., ASTER Team, Jull
1755 A. J., Lenaerts J., Yamaguchi A., Huybrechts Ph. and Claeys Ph. (2019) Unravelling the
1756 high-altitude Nansen blue ice field meteorite trap (East Antarctica) and implications for
1757 regional palaeo-conditions. *Geochim. Cosmochim. Acta* **248**, 289–310.
1758

Table 2.

Sample name	Textural group	Diameter (μm)	Mass (μg)	Weathering stage ^a	Vesicles or high-density phases (HDP)	Isotopic group	$\delta^{17}\text{O}$ ‰ VSMOW	$\delta^{18}\text{O}$ ‰ VSMOW	$\Delta^{17}\text{O}$ ‰ VSMOW
WF1202B-0053	V	465	128	Fresh (0a)	Not present	CC - Group 1	13.30	32.86	-3.79
WF1202B-0054	V	459	124	Fresh (0a)	HDP	OC - Group 3	8.19	14.68	0.56
WF1202B-0055	V	689	350	Fresh (0a)	HDP	CC - Group 1	7.15	17.91	-2.16
WF1202B-0056	BO	536	191	Fresh (0a)	Not present	OC - Group 3	8.18	14.89	0.44
WF1202B-0057	V	685	362	Moderate alteration (2a)	Vesicles	CC - Group 2	8.16	18.51	-1.46
WF1202B-0058	BO	505	166		Fresh (0a)	Not present	CC - Group 1	6.34	19.99
WF1202B-0059	V	625	274	Fresh (0a)	Not present	¹⁶ O-poor - Group 4	23.96	43.54	1.32
WF1202B-0060	V	601	276	Fresh (0a)	Not present	OC - Group 3	9.04	15.83	0.81
WF1202B-0061	CC	606	253	Fresh (0a)	HDP	CC - Group 1	3.94	11.31	-1.95
WF1202B-0062	CC	522	192	Fresh (0a)	Vesicles	¹⁶ O-poor - Group 4	22.90	40.34	1.92
WF1202B-0063	V	622	413	Fresh (0a)	Vesicles	OC - Group 3	10.09	18.69	0.37
WF1202B-0064	BO	592	310	Fresh (0a)	Not present	CC - Group 1	2.76	12.76	-3.87
WF1202B-0065	BO	516	187	Fresh (0a)	Vesicles	¹⁶ O-poor - Group 4	22.59	40.03	1.77
WF1202B-0067	V	715	450	Fresh (0a)	Vesicles	OC - Group 3	9.40	17.25	0.43
WF1202B-0068	CC	492	150	Fresh (0a)	Not present	CC - Group 1	16.62	36.35	-2.28
WF1202B-0069	CC	524	143	Fresh (0a)	Not present	CC - Group 1	4.12	11.03	-1.61
WF1202B-0070	Po	439	127	Fresh (0a)	Not present	¹⁶ O-poor - Group 4	23.20	41.62	1.56
WF1202B-0071	BO/CC	482	187	Fresh (0a)	HDP	Ambiguous	19.08	37.18	-0.25
WF1202B-0072	CC	490	143	Fresh (0a)	Vesicles	OC - Group 3	6.42	10.51	0.96
WF1202B-0073	μPo	491	162	Fresh (0a)	Vesicles	CC - Group 1	9.42	22.77	-2.42
WF1202B-0075	V	483	144	Fresh (0a)	Not present	OC - Group 3	9.91	17.68	0.72
WF1202B-0076	BO	497	161	Fresh (0a)	Not present	CC - Group 1	14.55	32.41	-2.31
WF1202B-0077	BO	472	163	Fresh (0a)	Not present	CC - Group 1	13.05	30.65	-2.88
WF1202B-0078	CC	471	133	Fresh (0a)	Vesicles	CC - Group 1	6.18	22.04	-5.28
WF1202B-0079	Irregular	479	134	Fresh (0a)	Not present	OC - Group 3	6.43	10.95	0.73
WF1202B-0080	BO/CC	542	161	Fresh (0a)	Vesicles	CC - Group 1	11.65	28.01	-2.91
WF1202B-0101	BO	418	117	Minor alteration (1a)	Vesicles	CC - Group 1	6.25	16.25	-2.20
WF1202B-0105	V	325	45		Fresh (0a)	Not present	CC - Group 1	4.59	12.07

Notes: Textural group: V = glassy; BO = barred olivine; CC = cryptocrystalline; Po = porphyritic; μPo = microporphyritic.

^aFollowing classification by van Ginneken et al. (2016).

Isotopic group: CC = carbonaceous chondrite; OC = ordinary chondrite.

Table 3.

Sample	Size	S-type	V-subtype	G-type	I-type	Number
WF	>400 μm	95%	33%	1%	4%	109
	>200 μm	95%	27%	2%	3%	228
FRO	>400 μm	<i>na</i>	<i>na</i>	2%	3%	331
	>200 μm	95%	15%	1%	4%	254
MIL	>400 μm	<i>na</i>	<i>na</i>	1%	3%	729
	>200 μm	<i>na</i>	<i>na</i>	<i>na</i>	3%	920
LAR	>60 μm	92%	19%	2%	6%	634
WAL	>100 μm	92%	10%	2%	6%	126
SPWW	>100 μm	98%	15%	1%	1%	1130
IO	>60 μm	91%	8%	3%	6%	453

Notes: *na* - identification of this type was not attempted or reported.

Table 4.

Groups ^a	OC-related	CC-related	¹⁶ O-poor	Ambiguous	HED-related	Total ^b
# of spherules in this work	8	15	4	1	0	28
% all sizes	29	54	14	4	0	
% 250-500 μm	29	57	7	7	0	14
% 500-1000 μm	29	50	21	0	0	14
% V-type	50	40	10	0	0	10
% BO-type	14	71	14	0	0	7
% Po-type	0	50	50	0	0	2
% CC-type	17	67	17	0	0	6
# of spherules in literature	23	81	11	15	6	136
% all sizes	17	60	8	11	4	
% <100 μm	7	66	17	10	0	29
% 100-250 μm	6	68	10	16	0	31
% 250-500 μm	9	80	6	6	0	35
% 500-1000 μm	38	38	0	6	19	32
% > 1000 μm	44	11	11	33	0	9

^aThe proportion of CSs assigned to the ambiguous group provides some indication on the degree of certainty in the assignment of particles to these isotopic groups.

^bTotals are expressed as the number of spherules.

Figure 1

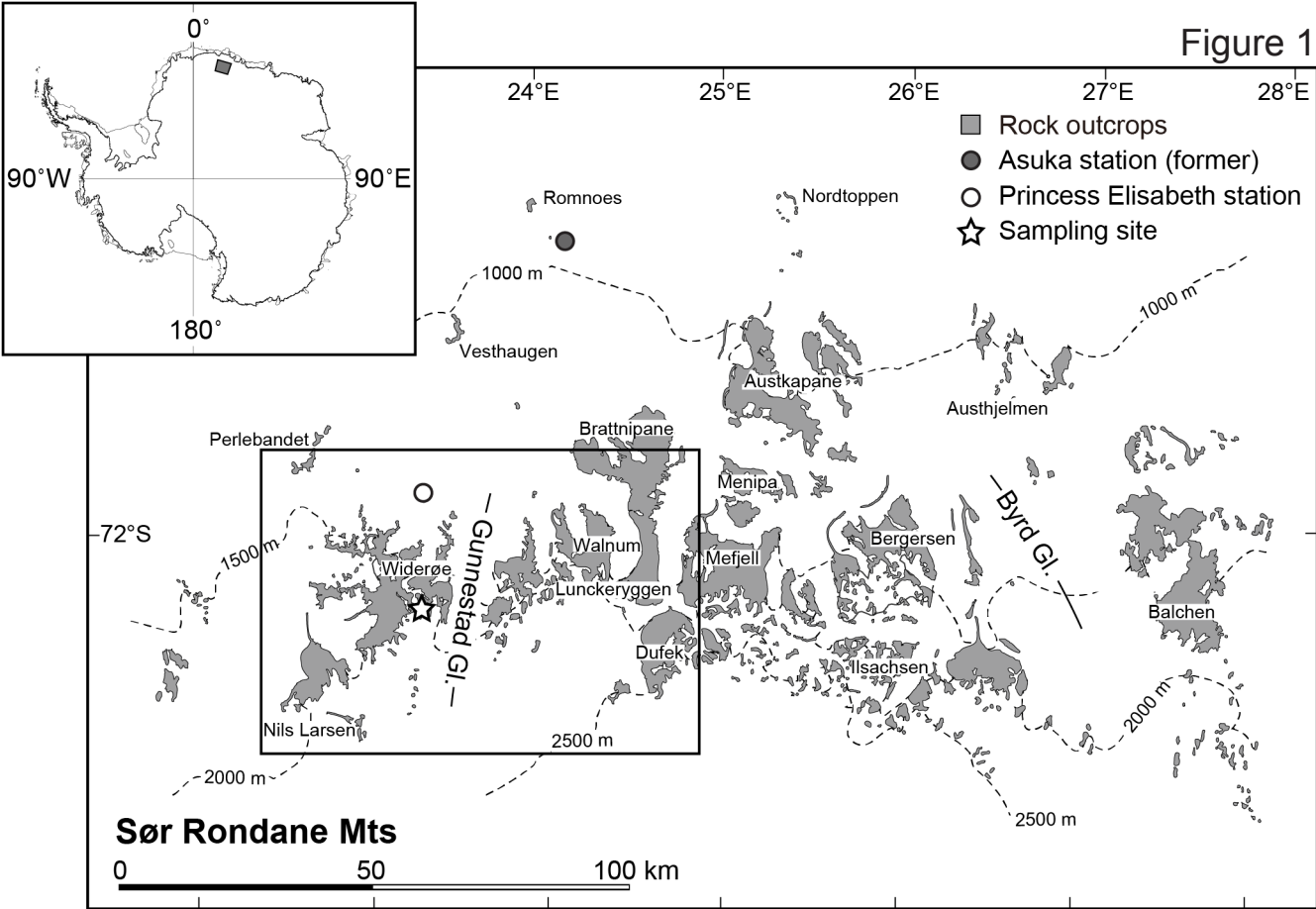


Figure 2

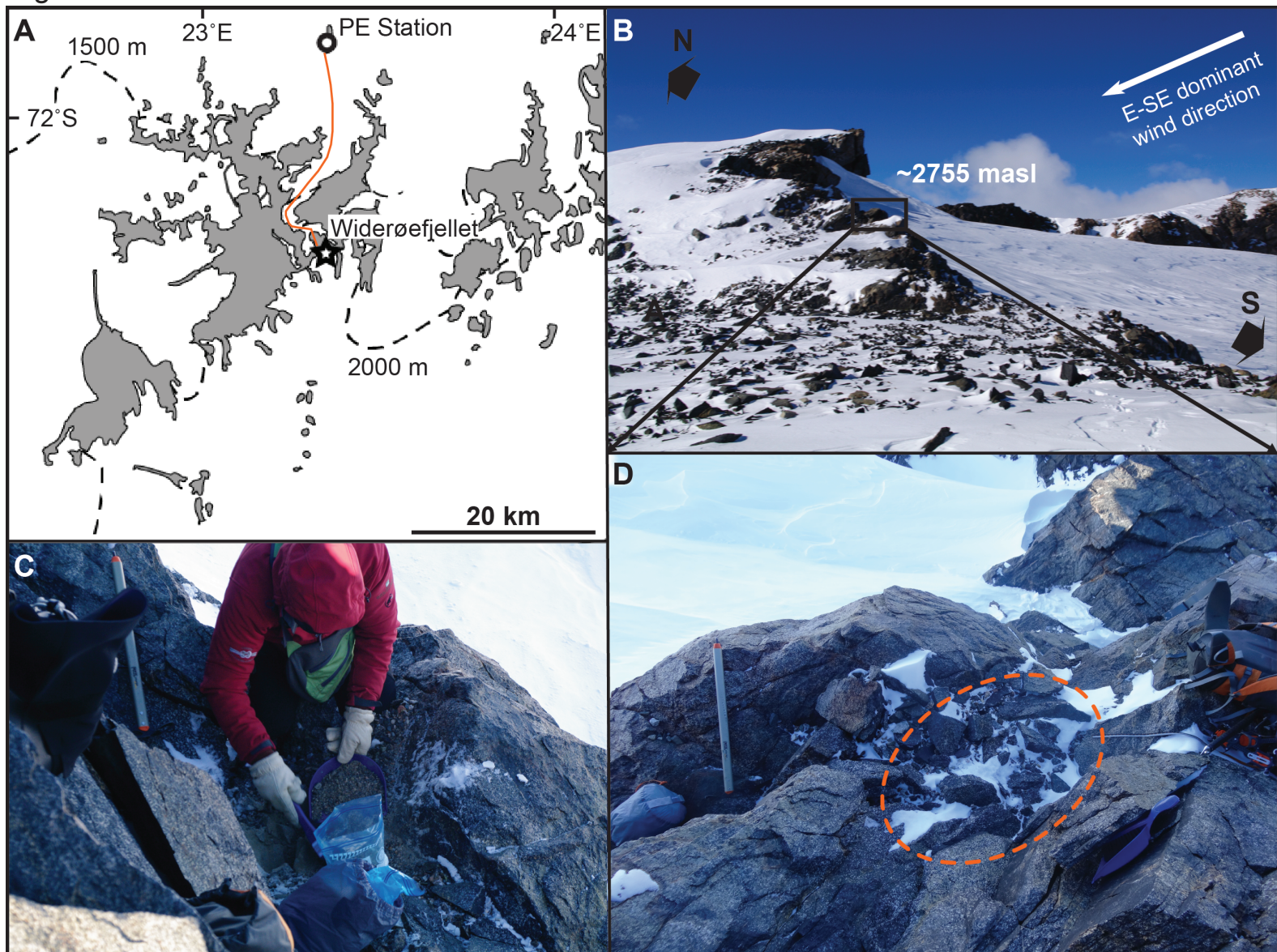


Figure 3

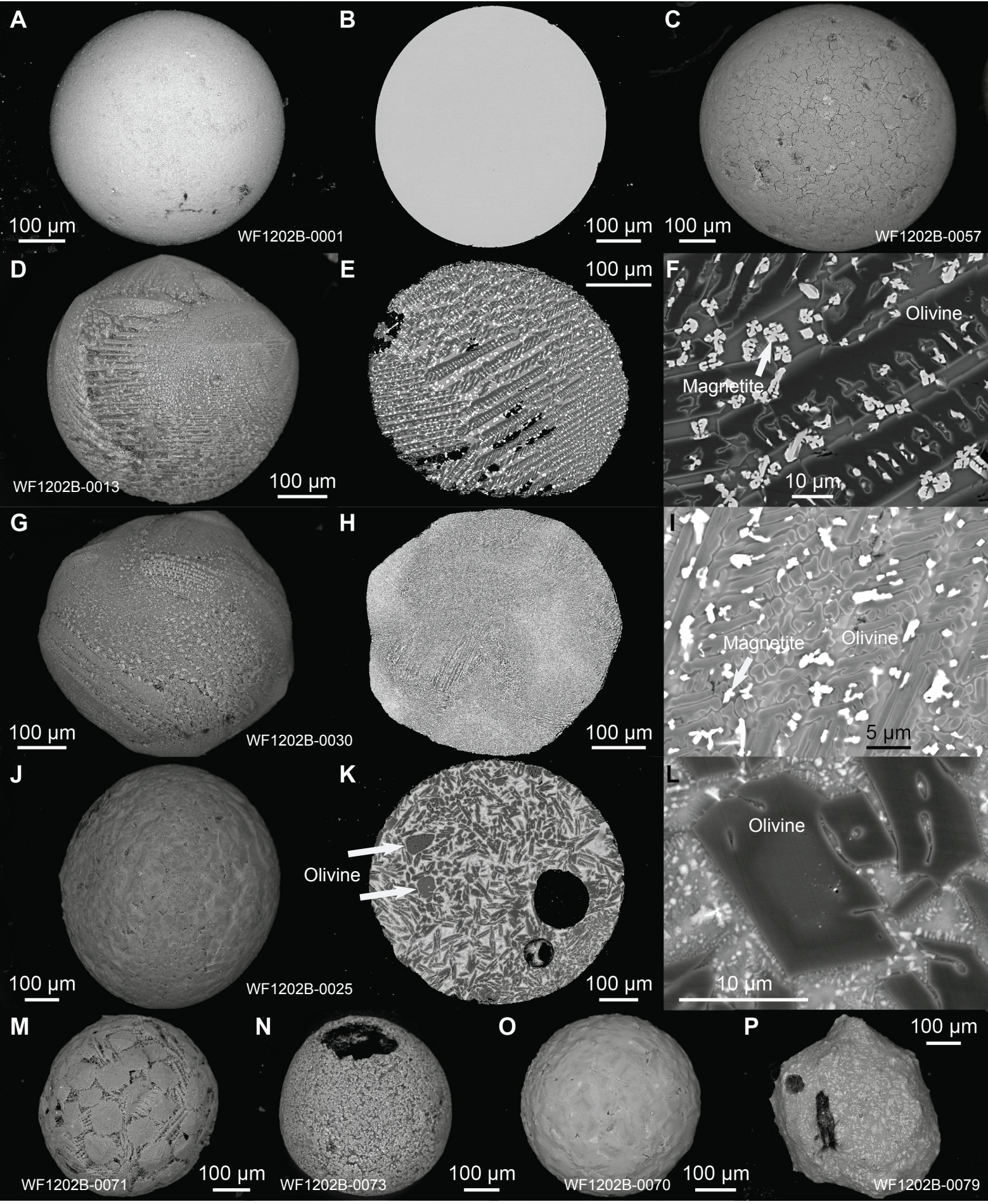


Figure 4

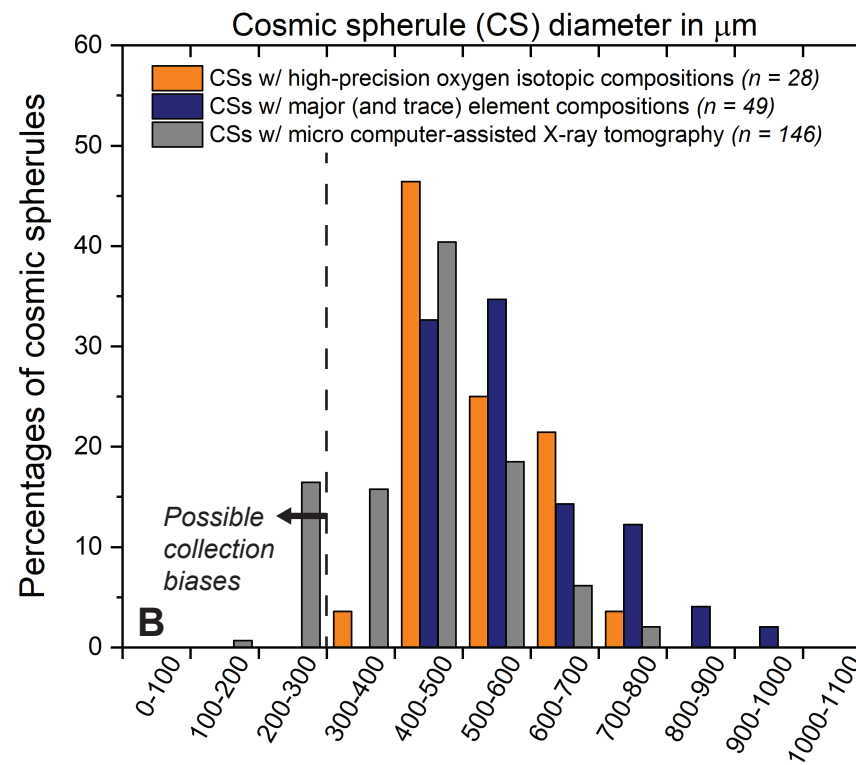
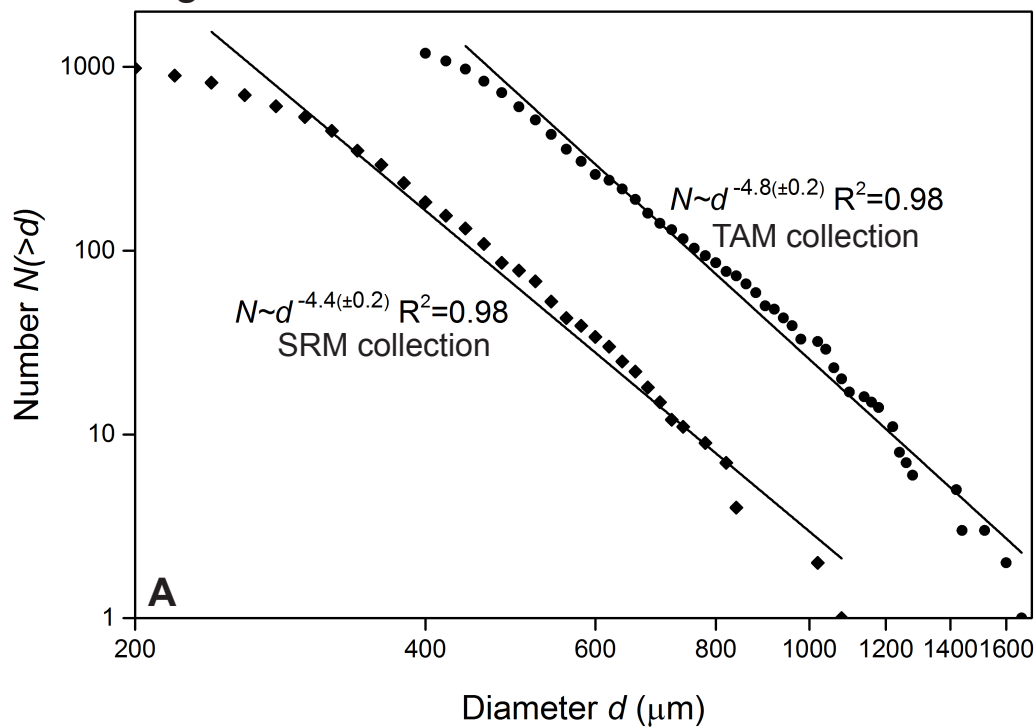
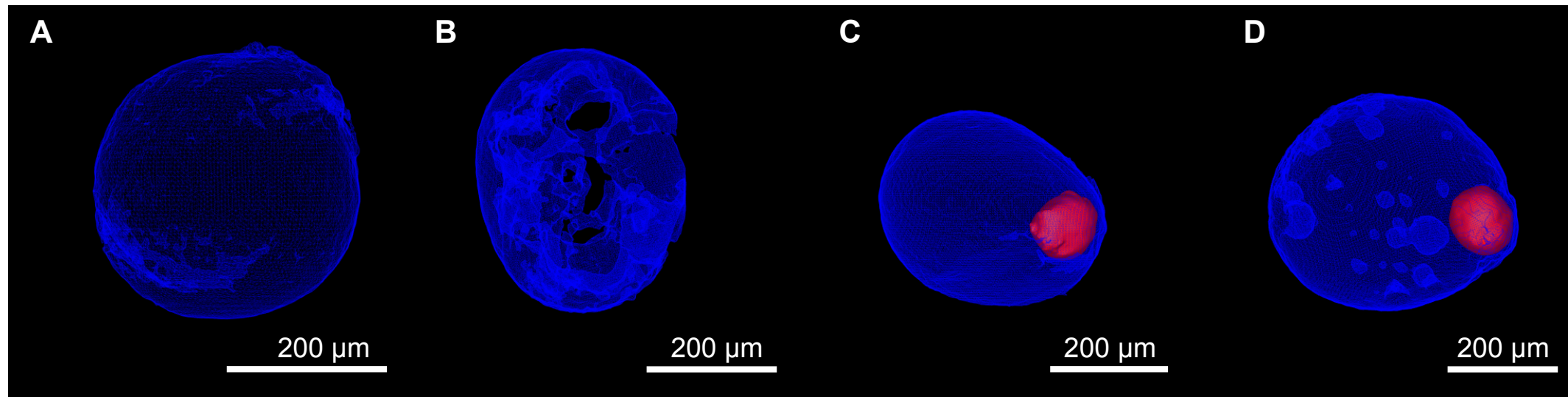


Figure 5



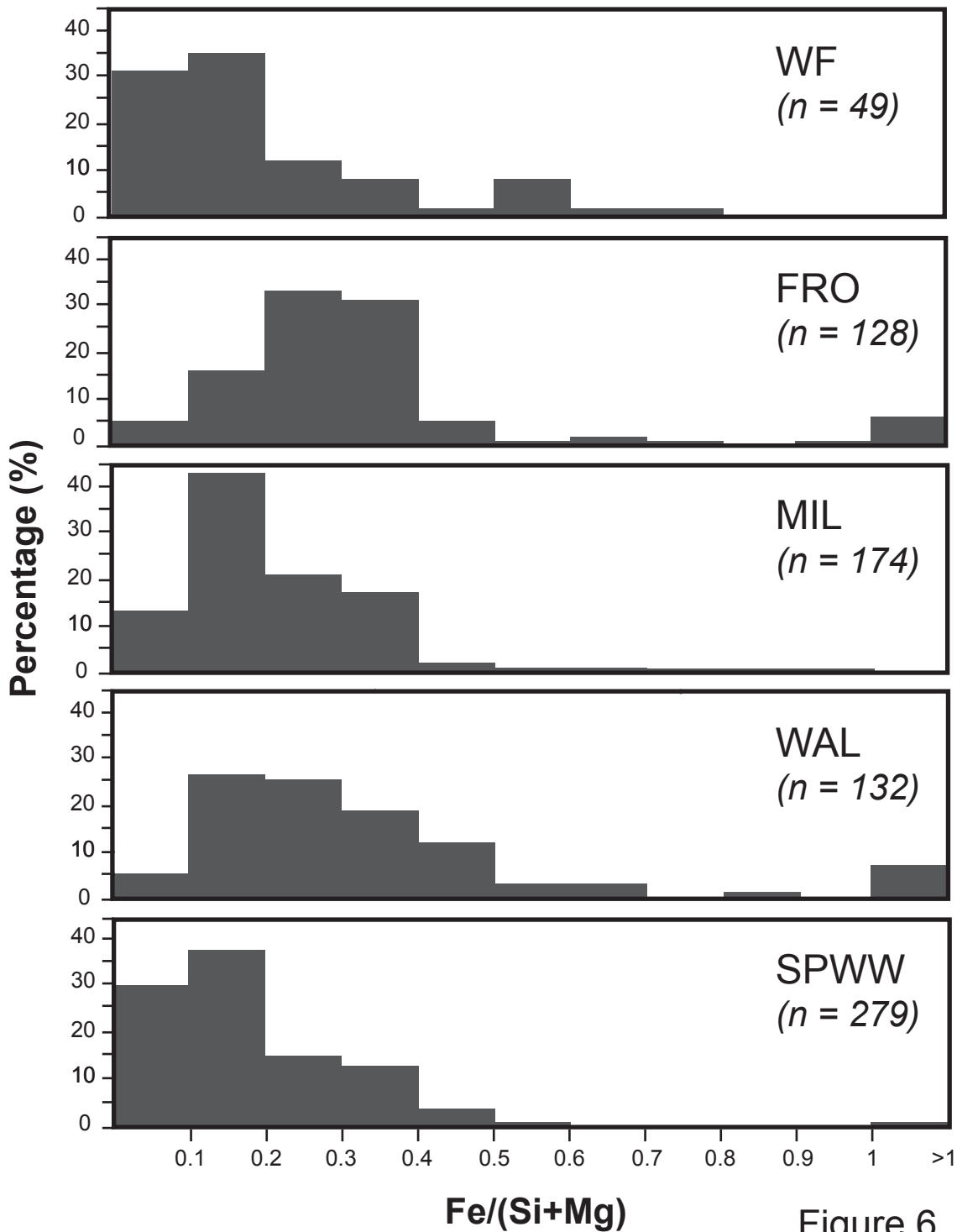


Figure 6

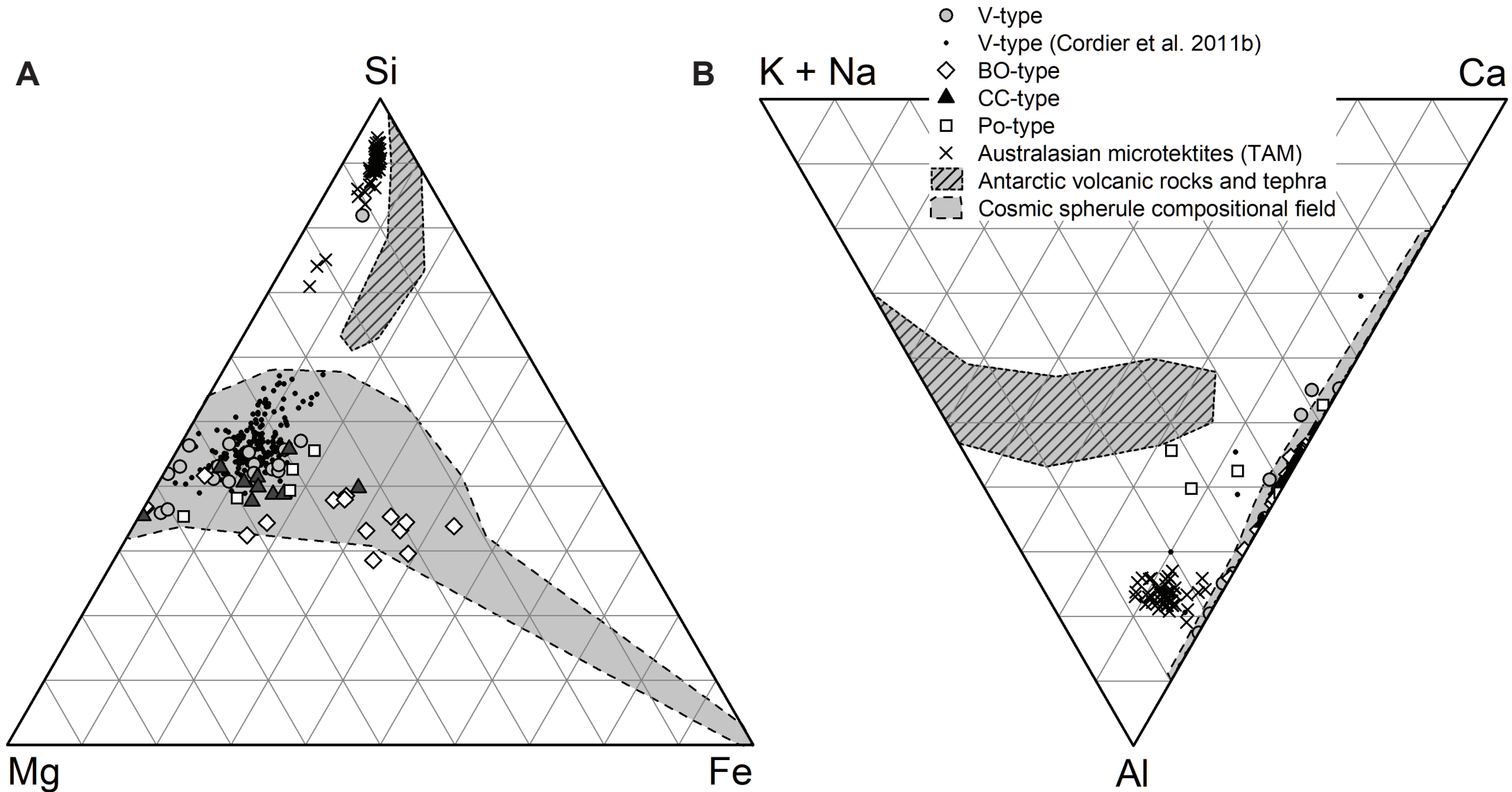
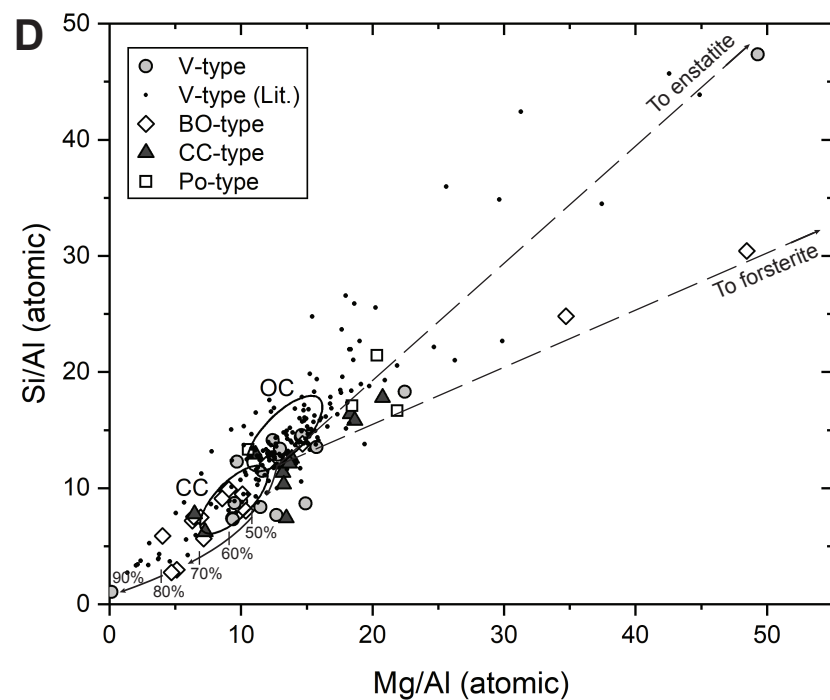
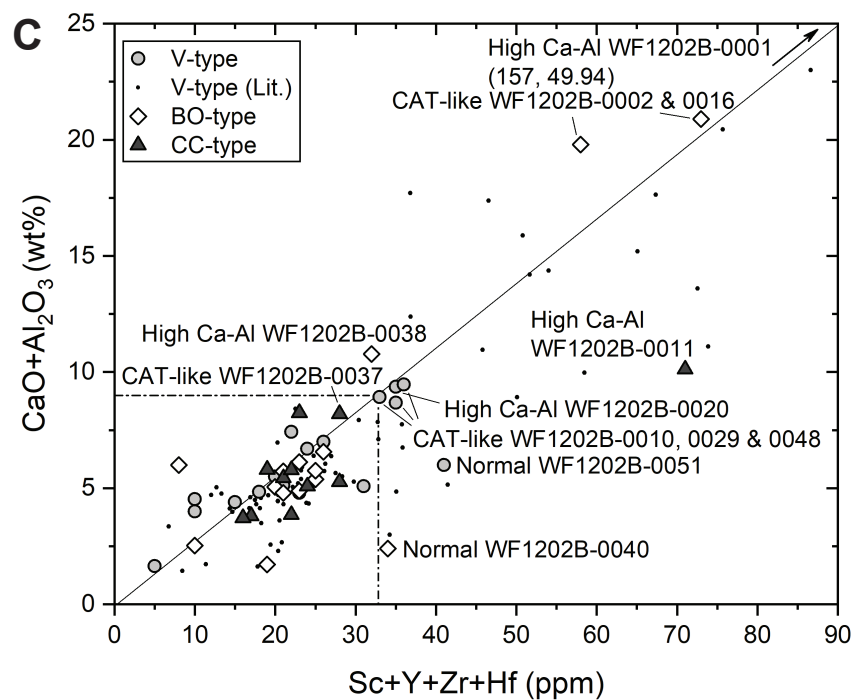
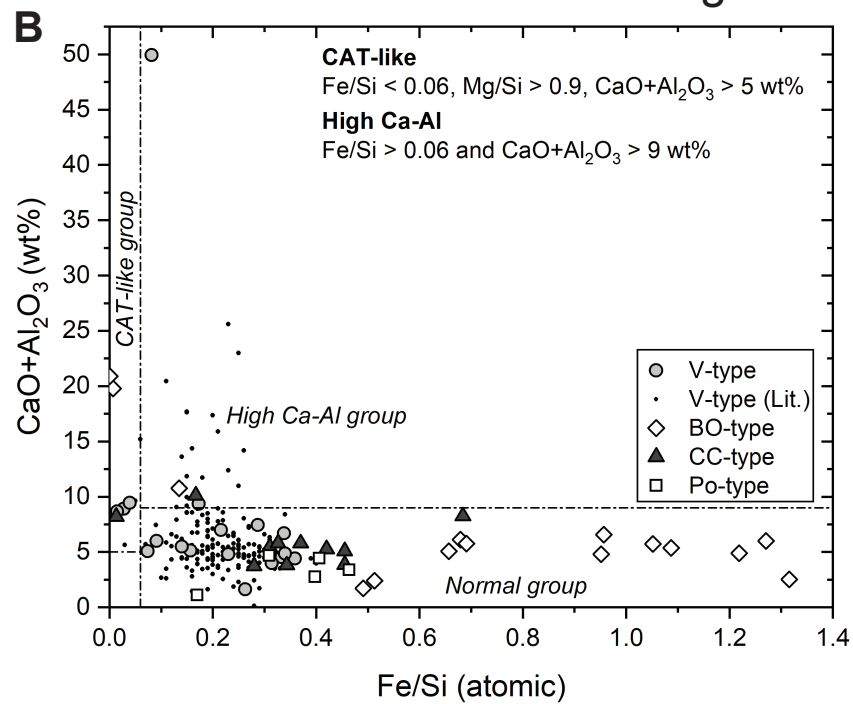
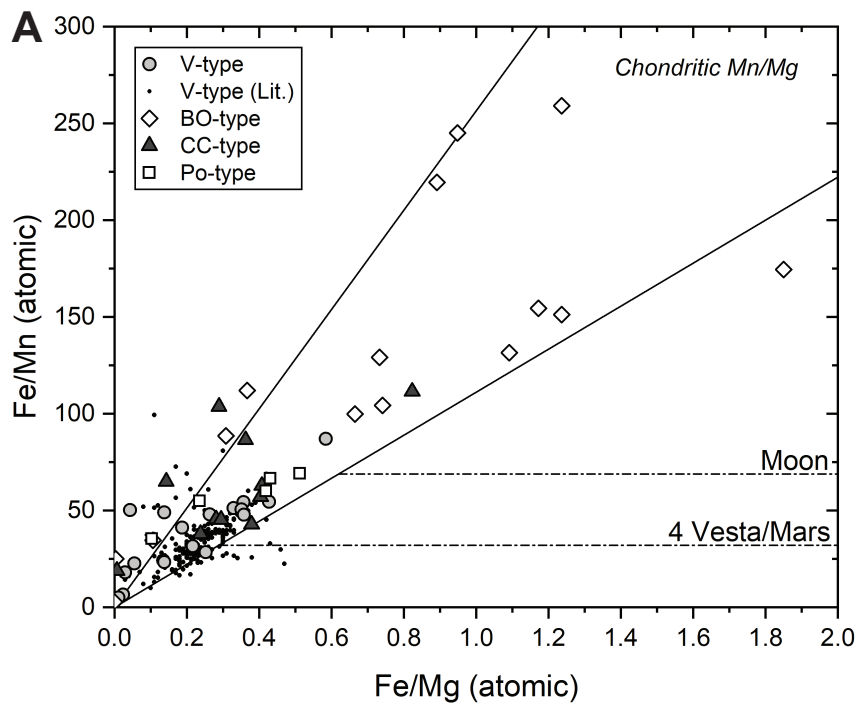


Figure 7

Figure 8



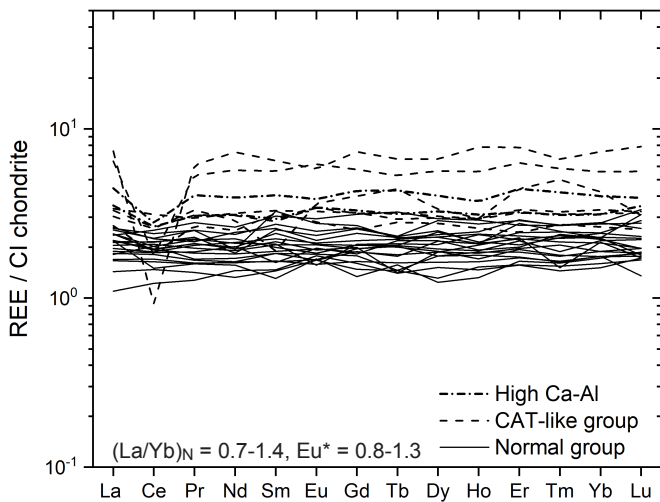
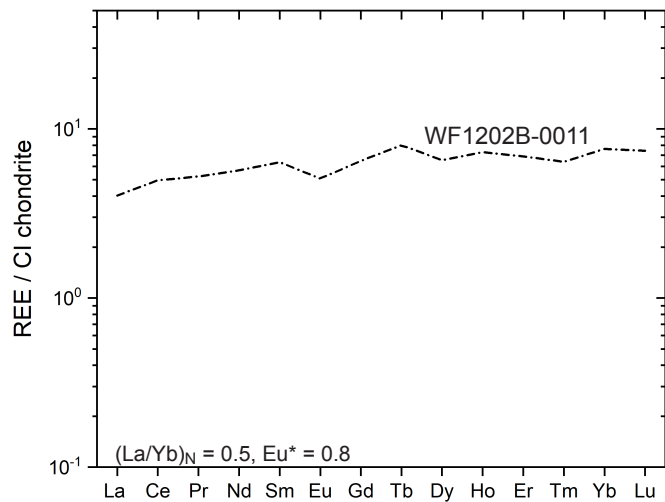
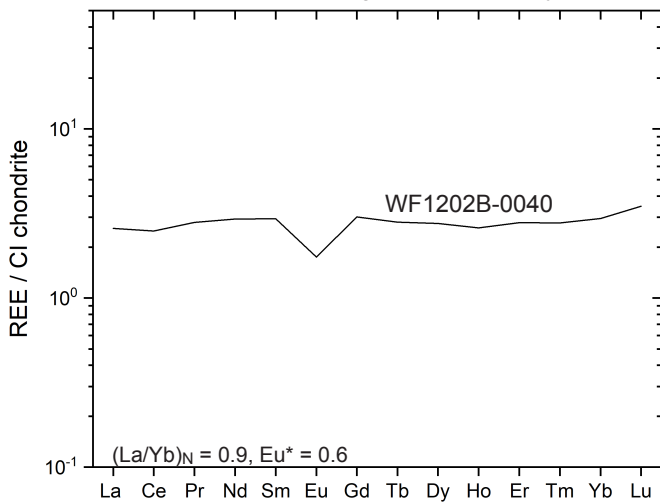
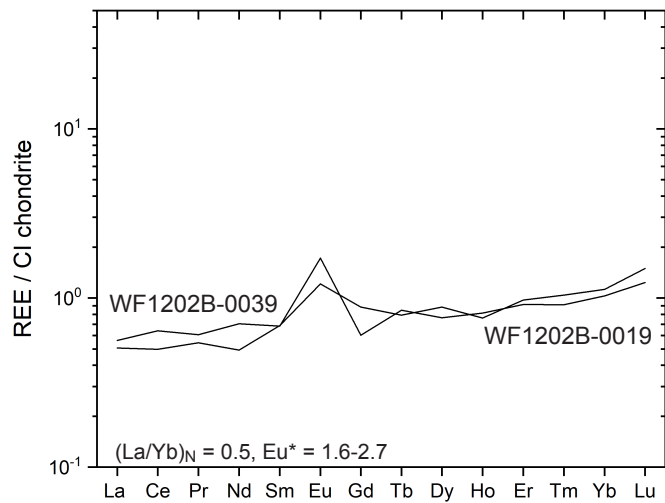
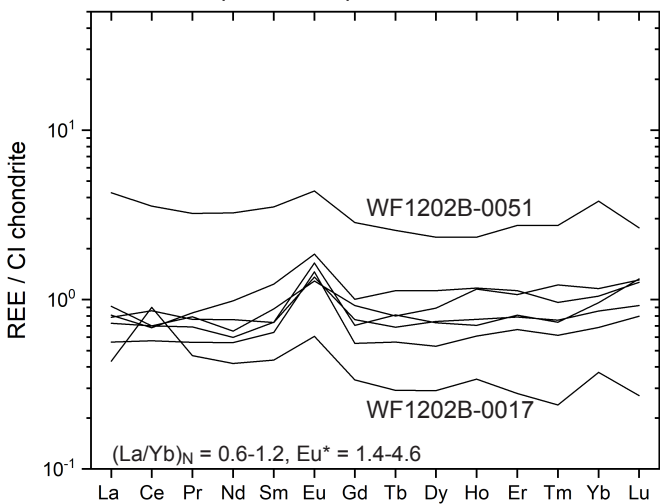
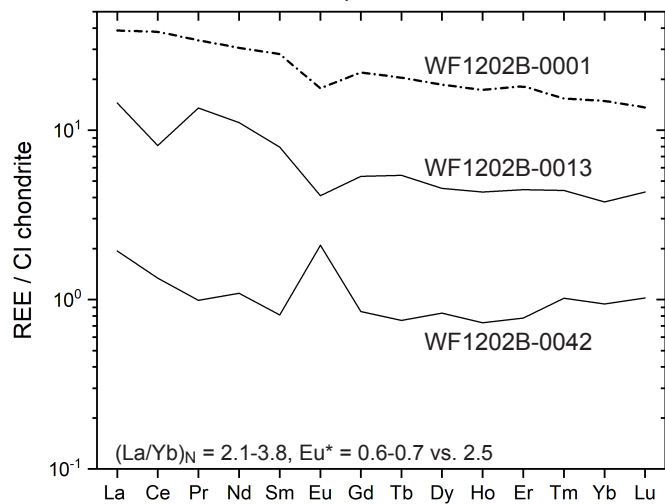
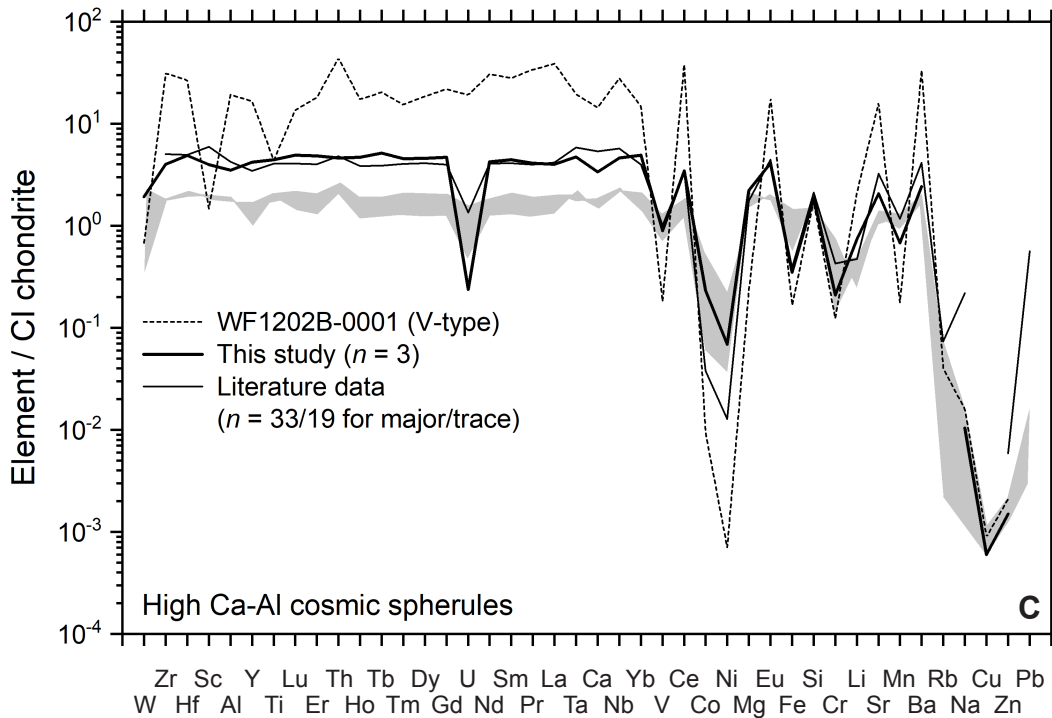
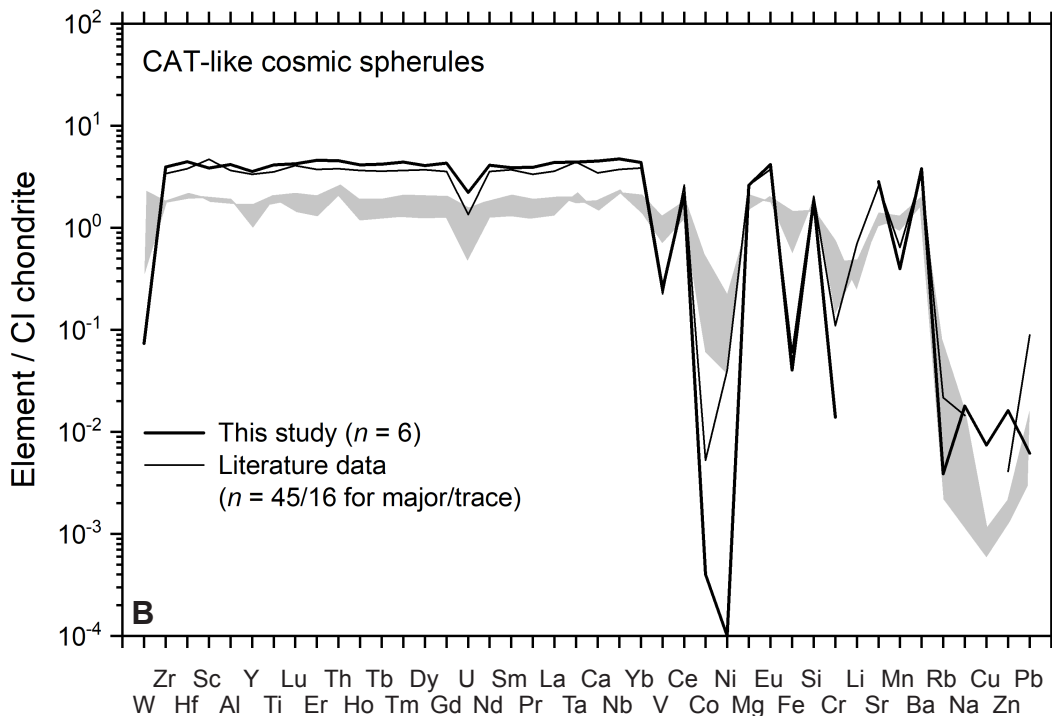
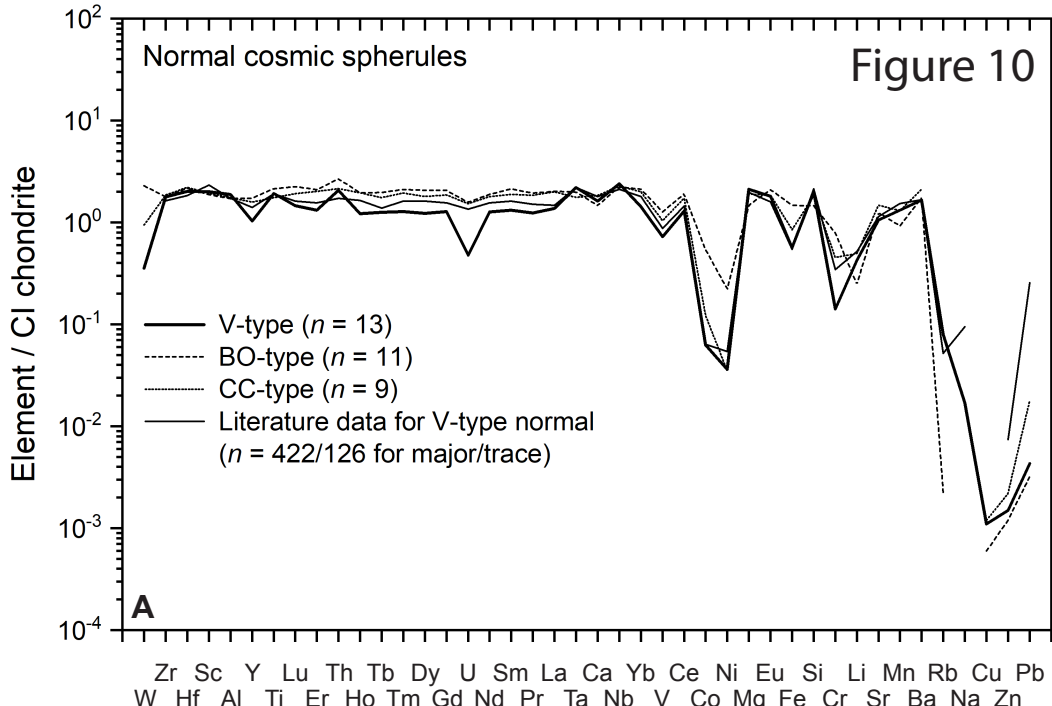
A Flat REE patterns**D** LREE-depleted REE pattern**B** Flat REE pattern w/ negative Eu anomaly**E** LREE-depleted patterns w/ positive Eu anomalies**C** Flat REE patterns w/ positive Eu anomalies**F** LREE-enriched REE patterns

Figure 10



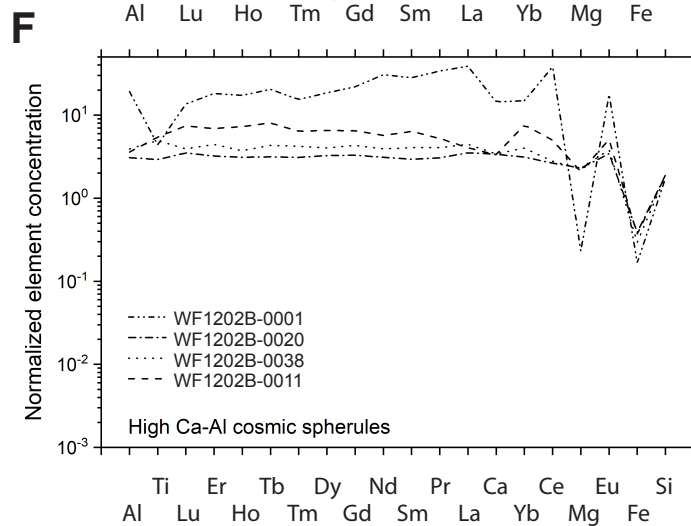
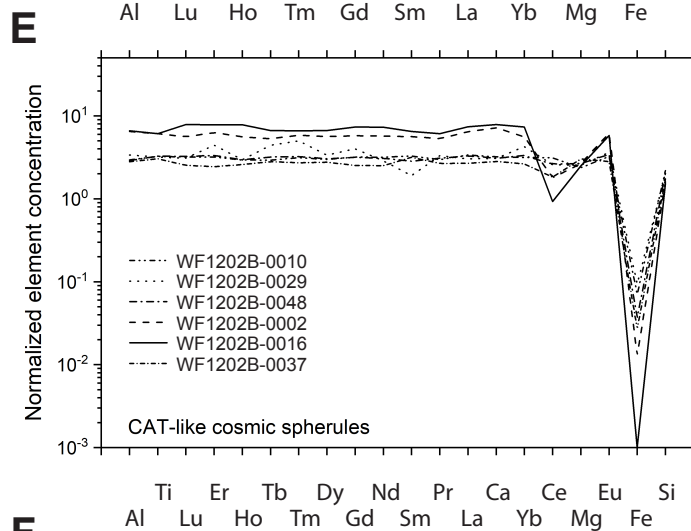
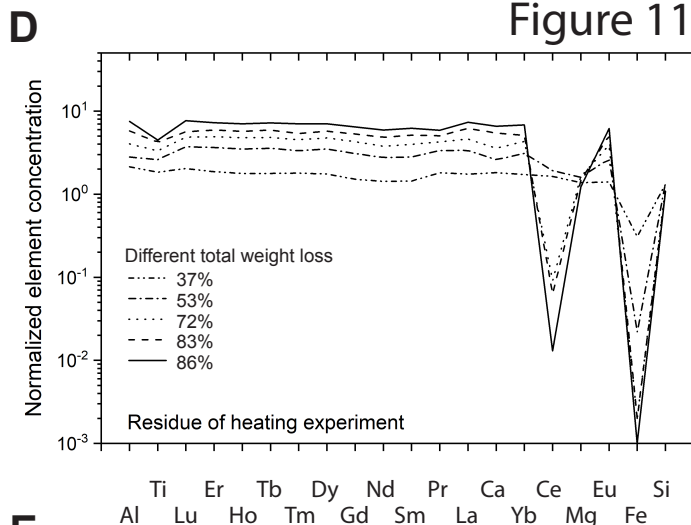
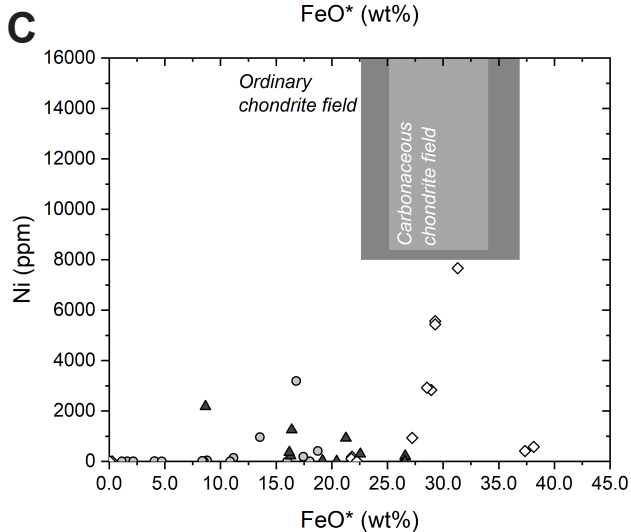
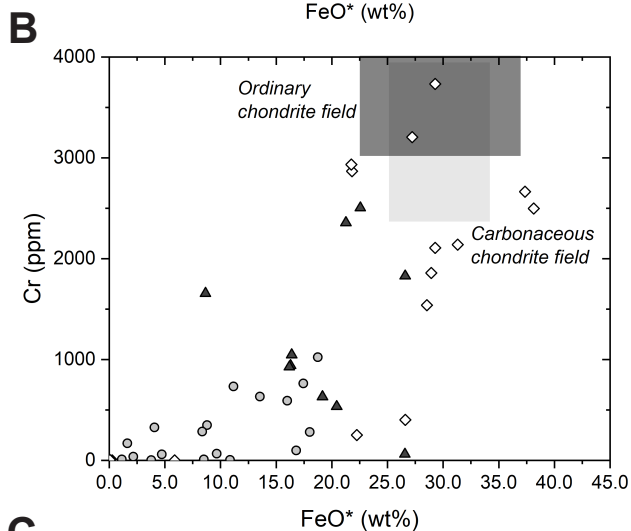
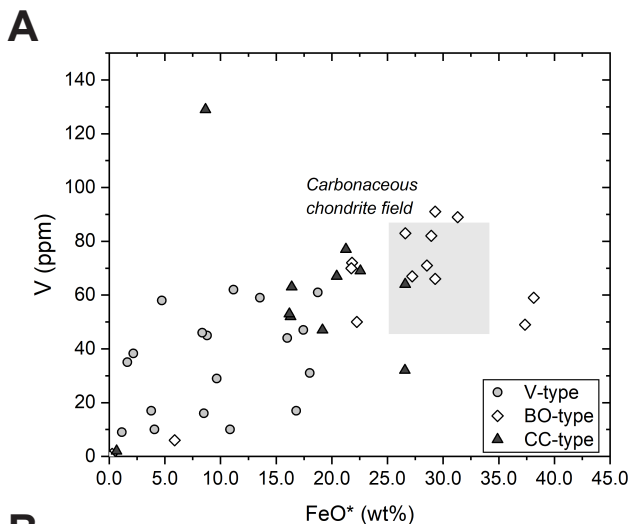


Figure 12

